Shiwen Sun, MSc

APPLICATIONS OF INTEGRATED OPTICAL SENSORS FOR pH AND OXYGEN MONITORING IN MICRO(BIO)REACTOR

DOCTORAL THESIS

to achieve the university degree of

Doktor der technischen Wissenschaften

submitted to

Graz University of Technology

Supervisor

Assoc.Prof. Dipl.-Chem. Dr.rer.nat. Torsten Mayr

Institute of Analytical Chemistry and Food Chemistry

Graz, October 2017

AFFIDAVIT

I declare that I have authored this thesis independently, that I have not used other than the declared sources/resources, and that I have explicitly indicated all material which has been quoted either literally or by content from the sources used. The text document uploaded to TUGRAZonline is identical to the present doctoral thesis.

Date

Signature

Acknowledgement

First and foremost, I would like to express my sincere gratitude to my advisor, Assoc.Prof. Dipl.-Chem. Dr.rer.nat. Torsten Mayr, for his continuous support to my PhD study and research, and for giving me the chance and freedom to explore the scientific world.

I feel extremely grateful to work for the EUROMBR ITN. I got the chance to work together with and to learn from other ESRs and PIs, and to receive extensive training through my PhD.

I also would like to thank Prof. Piotr Garstecki and Prof. Martin Roth for letting me work in theirs groups. Especially Prof. Garstecki, he was very patient and inspiring during the work of our collaborative publication.

Also all the group members of the Institute of Analytical Chemistry and Food Chemistry have given me great support during the last three years.

Last but not least, I wouldn’t finish this long journey without my friends. Thank you for all your support along the way.

Dedication

To my parents for their support and love when I was abroad these years.

谨以此论文献给我的父亲母亲，感谢你们对我不在你们身边的理解与支持。

Abstract of the dissertation

We present here several applications of using optical chemical sensors to monitor the concentration of oxygen and pH in (bio)processes in microfluidics systems and micro(bio) reactors. Microfluidics has been an emerging tool for studies involving (bio)processes. Process monitoring is critical during the (bio)chemical reactions or biological experiments. It is challenging to use conventional analytical tools into microfluidics, due to their small dimension, limited volume of samples, and rapid evolution in process. Among many analytical tools, optical chemical is the best fit for microfluidics, since they are easy to miniaturize, have short response-time, high sensitivity and selectivity.

We show different approaches to integrate optical sensors into microfluidic systems, including sensor layer, single spot in microfluidics structure, and nanoparticles. We demonstrate the oxygen imaging in flow cell, which reveals the spatial and real-time information of enzymatic reaction in the chip. Single-point measurement of oxygen and pH gives a close look of metabolic activities during cell culturing in a microbioreactor with additional aeration. Last, we use the sensor nanoparticles to monitor the concentration of oxygen and pH in microdroplets during biological experiments. It is the most accurate measurement of oxygen level in droplet microfluidics has been shown. We investigate the feasibility of using pH sensor nanoparticles for screening of pathogenic strains in droplet. The readout device used is a miniaturized fluorometer, which is possible to use for different microfluidic setups. We believe this simple and versatile approach of monitoring the concentration of oxygen and change of pH would be a great tool for i) fundamental study to of microfluidic system; ii) accurately monitoring of (bio)processes at small scale; and iii) building a powerful platform/ toolbox of using microfluidics to perform sophisticated biological experiments.

Table of Contents

Acknowledgement v

Dedication vii

Abstract of the dissertation ix

Table of Contents xi

List of figures xv

List of tables xix

List of abbreviations xxi

1 Introduction 1

1.1 Significance/Motivation 1

1.2 Scope and outline of the dissertation 2

1.3 Optical chemical sensors 3

1.3.1 Optical oxygen sensing 4

1.3.2 Optical pH sensing 4

1.3.3 Detection methods 6

1.4 Microfluidic systems 7

1.4.1 Continuous flow microfluidics 8

1.4.2 Droplet-based microfluidics 9

1.5 Integration of sensors in microfluidics 10

1.5.1 Deposition of the sensors 10

1.5.2 Physical and chemical stability of the sensors 12

1.5.3 Compatibility of the sensors with fabrication methods 13

1.5.4 Detecting methods 13

1.5.5 Limit of detection 13

2 Imaging of oxygen in microreactors and microfluidic systems 15

Abstract 15

2.1 Introduction 15

2.2 Oxygen imaging in microreactors and microfluidic systems 19

2.2.1 Oxygen imaging principle 19

2.2.2 Sensor formats 20

2.2.3 Challenges for oxygen imaging in microfluidics 24

2.3 Optical measurement system 27

2.4 Application of oxygen imaging in microreactors and microfluidic systems 28

2.4.1 Monitoring oxygen gradients in microfluidic systems 28

2.4.2 Determination of oxygen concentration in microfluidic systems for cell culture 31

2.4.3 Measuring single-cell oxygen consumption rates in microfluidic devices 32

2.4.4 Oxygen imaging for chemical reaction related applications of microfluidic systems 34

2.5 Conclusion and outlook 36

2.6 Acknowledgment 37

3 Oxygen and pH sensing for bioprocess analysis in micro(bio)reactor 39

3.1 Introduction 39

3.2 Materials and Methods 43

3.2.1 Fabrication of resealable flowcells 43

3.2.2 Surface activation and enzyme immobilization for flowcells 45

3.2.3 Determination of enzymatic activity 46

3.2.4 Fabrication of multiphase microreactor 47

3.2.5 Sensing materials 47

3.2.6 Integration of sensor materials into flowcell and micro(bio)reactor 50

3.2.7 Readout system 51

3.2.8 Calibration of the sensors 52

3.3 Results and discussion 52

3.3.1 Characterization of fabrication of resealable flowcells 52

3.3.2 Transfer of oxygen through the gasket in the flowcells 56

3.3.3 Online oxygen sensing to monitor enzymatic reaction in the flowcells 57

3.3.4 Oxygen imaging in the flowcells 61

3.3.5 Characterization of the multiphase micro(bio)reactor 63

3.3.6 Monitor bioprocess in micro(bio)reactor during cultivation 63

3.4 Conclusions 65

3.5 Acknowledgement 66

4 Lifetime of phosphorescence from nanoparticles yields accurate measurement of concentration of oxygen in microdroplets and allows to monitor the metabolism of bacteria 67

Abstract 67

4.1 Introduction 68

4.2 RESULTS AND DISCUSSION 71
4.2.1 Tubing-based microfluidic cell culturing device 71
4.2.2 Compatibility of oxygen sensor nanoparticles and microfluidic cell culturing system 72
4.2.3 On-line real-time measurements of concentration of oxygen in microdroplets 74
4.2.4 Monitoring bacterial growth and concentration of oxygen in microdroplets 76

4.3 Conclusions 80

4.4 Materials and methods 81
4.4.1 Preparation of oxygen sensor nanoparticles and calibration 81
4.4.2 Microfluidic cell culturing device 82
4.4.3 Bacteria and Media used 83

4.5 Supporting information 83
4.5.1 Optical Oxygen Sensing Principle 83
4.5.2 Calibration of Oxygen Sensor Nanoparticles 84
4.5.3 Autoclavability and Biocompatibility of Oxygen Sensor Nanoparticles 85
4.5.4 Fast Oxygenation of Low Oxygen Microdroplets by Carrier Oil (FC40) in Microfluidic Culturing System 86
4.5.5 Oxygen Transfer From Ambient To Inside of Tubing of Microfluidic Culturing System 90
4.5.6 Determination of Oxygen Concentration in Each Individual Microdroplet 91
4.5.7 Technical Drawing of Teflon FEP Fluidic Connector 92

4.6 Acknowledgement 93

5 Using pH sensor nanoparticles to monitor pH change in droplets during cell culturing 95

5.1 Introduction 95

5.2 Results 98
5.2.1 Measuring principle for pH sensing and its calibration 98
5.2.2 Extended dynamic range of optical pH sensor 101
5.2.3 Validation of measurement of pH in droplets 102
5.2.4 Fabrication of the microfluidic culturing system 104
5.2.5 Selection of the data from measurement 105
5.2.6 Identification of pathogenic strain by the difference of change in pH during cultivation 106
5.2.7 Effect of culturing media on the pH sensor nanoparticles 109

5.3 Discussion 113
5.3.1 Extended dynamic range of optical pH sensor by using different aza-BODIPY building block.... 113
5.3.2 Potential of our tubing based microfluidic system 114
5.3.3 Potential improvement for optical pH sensing in droplets 115
5.3.4 Application of machine learning for sensing and droplet microfluidic system 116

5.4 Conclusions 117

5.5 Materials and Methods 118

5.5.1 Synthesis of the sensor nanoparticles 118
5.5.2 Detection unit 118
5.5.3 Calibration of the dual sensor nanoparticles 119
5.5.4 Tubing-based cell culturing microfluidic system 119
5.5.5 Bacteria and Medium used 120

5.6 Supplementary information 120

5.6.1 Temperature during the incubation in droplets 120

6 Conclusions 123

7 Acknowledgement of previous publications 125

8 References 127

9 Appendix 133

9.1 Curriculum Vitae 133

List of figures

Figure 1.1: A scheme of two kinds of fluids in continuous flow and in segmented flow. Parabolic flow and Taylor-Aris dispersion [17,18] cause the mix of two fluids in continuous flow, but not in segmented flow (droplet microfluidics). This scheme is created based on the image published by Casadevall I Solvas and deMello [19]. 9

Figure 2.1: (a) Microscopic color (original) image and (b) calculated oxygen image of one channel of a microfluidic chip, which is flushed with nitrogen. (c) Macroscopic color (original) image and (d) calculated oxygen image of four channels of the same microfluidic chip; the first and third channels were flushed with nitrogen, while the other channels contained air (Reprinted from [29] with permission from Royal Society of Chemistry). 18

Figure 2.2: Different optical oxygen sensor formats used in microfluidic systems. 21

Figure 2.3: Schematic of the sensor fabrication process depicting stamp fabrication in PDMS (a, b), spin-coating of the sensor layer (c, d), pattern transfer into the sensor layer by RIE (e), and integration with a PDMS microfluidic device by plasma bonding (f) (Reprinted from [56] with permission from Royal Society of Chemistry). 23

Figure 2.4: A typical setup scheme for oxygen imaging systems. 28

Figure 2.5: (a)–(i) Time-lapse images of the patterned oxygen microgradient as it is moved around using ten horizontal microelectrodes (each 20 mm 6 1 mm). Video capture frames are 20 s apart and were taken with a white light microscope (Reprinted from [88] with permission from Royal Society of Chemistry). 29

Figure 2.6: oxygen measurements from a closed-loop PDMS bioreactor for continuous cell culture of C2C12 mouse myoblasts. (a) Device schematic. Channel shape was an isosceles trapezoid with a height of 30µm and an upper (lower) PDMS layer of 180 µm(402 µm). Each of the six loops has a right and left valve separating it from the others. (b) Oxygen distribution images at different points of a single loop (binary scale in µM) (Reprinted from [59] with permission from SPIE). 31

Figure 2.7: (a) Optical microscope image of a trapped, attached cell. (b) Fluorescent image of an attached cell stained with Calcein AM with the sensor ring highlighted with a white circle (Reprinted from [99] with permission from IOP Publishing). 34

Figure 2.8: Fluorescence intensity images of the PDMS optode film seen from the cover plate side (a) and glass base side (b) of the silicon-onglass micromodel. LED excitation light is provided through the cover plate side to the optode film (Reprinted from [70] with permission from Royal Society of Chemistry). 35

Figure 2.9: Fluorescence lifetime image obtained by a scanning phase technique for an optode in a silicon-on-glass micromodel. The dark region in the lower left corner has high oxygen, and hence little fluorescent intensity, a short lifetime, and a low phase angle, while the regions toward the upper right are anoxic. The gradient was formed in a two-input micromodel. The locations of pillars are apparent as black circles in the anoxic region (Reprinted from [101] with permission from SPIE). 36

Figure 3.1: Drawing of the chip holder used for the experiments. (Left) exploded view of the resealable flowcell in the open holder with the tubings and optical fibers connected. (Right) drawing of the closed holder. 41

Figure 3.2: Multiphase microreactor (mMR), including the reaction chamber, fluidic inlets and outlets, nozzle, adjustable-height effluent tube, fiber optic channels with alignment and clamp structures and biconvex cylindrical lenses for correcting the numerical aperture. 42

Figure 3.3: Dispensing of prepolymer of gasket onto glass slides. The gasket height depended on the dispensing settings and the respective polymer, e.g. its viscosity. The prepolymer was dispensed to the surface by applying a pressure to the prepolymer cartridge. By controlled movement in x,y,z-direction the flowcell boundary was made. 43

Figure 3.4: (Left) examples of various modules that could be combined to form a tailor-made flowcell. One module from section I–III and one from section 1–3 were selected and stacked. (I) Represents a homogeneous surface modification, e.g. with catalytic biomolecules or sensing layers. (II) Represents a modification for spot measurements. (III) Represents a heterogeneous surface modification, e.g. with two different enzymes. These modifications could also be applied to the fluidic part, i.e. 1–3. (Right) microfluidic chip with meandering channel and oxygen sensing layer (green) as used for the experiments. Please note, this example chip did not contain the access through holes. 44

Figure 3.5: Setup for on-line spot oxygen consumption measurement. An oxygen sensitive layer was integrated into the resealable flowcell. Optical fibers were led to the spots of interest through the top of the holder and the signals were monitored in real-time. 51

Figure 3.6: Various layouts of structured flowcells that have been successfully fabricated. The structures in (a)–(d) are all of the same height on a single device. In (e)–(f) the structures inside the outline are lower than the height of the outline. 53

Figure 3.7: Height distribution for one set of dispensing parameters. The mean height is 354 µm with a standard deviation of 6 µm. If a normal distribution is fitted, 95.44 %, which is the definition of $2\boldsymbol{\sigma}$, of the produced structures have a height in the range of 343 µm and 365 µm. 54

Figure 3.8: Evaluation of the oxygen transfer through the gasket. (a) Oxygen resaturation versus time in the gas phase, two different layouts, straight (figure 3.4(1) and meandering (figure 3.4(3)), and two different materials, PFE and medical silicone. (b) Time-lapse pictures of the first 6 min, 1 per min, of resaturation in the gas phase for a meandering MED channel. A 8 pixel by 8 pixel region of interest was chosen in the center of the fluorescence lifetime image for the numerical evaluation in (a). (c) Time-lapse pictures of the first 6 min, 1 picture per minute, of resaturation in water for a meandering MED channel. 56

Figure 3.9. On-line monitoring with integrated oxygen sensor. (a) Two point on-line monitoring of oxygen concentration at the inlet and outlet. GOX was bound to a PEI modified surface and a glucose mixture was flushed at different flow rates through the resealable flowcell, whilst the oxygen consumption was monitored simultaneously. The vertical lines indicate changes of the flow rates in the range of 50 to 5 µl min−1. (b) Volumetric activity of GOX, bound to different modified surfaces, calculated from the oxygen consumption. 58

Figure 3.10. Enzyme volumetric activity monitored during a 24 h period. The flowcell surface was activated with PEI for stable binding during the test with a flow rate of 20 µl min^{-1}. 60

Figure 3.11. Oxygen consumption monitoring of GOX immobilized on a PEI functionalized surface. Images were taken for various flow rates after equilibrium was reached, checked with two point monitoring. Flow rates: (a) 5 µl min^{-1}, (b) 10 µl min^{-1}, (c) 20 µl min^{-1}, (d) 30 µl min^{-1}, (e) 40 µl min^{-1}, and (f) 50 µl min^{-1}. 62

Figure 3.12: Setup of micro(bio)reactor with integrated sensors. 63

Figure 3.13: Change of glucose concentration, optical density, pH, and dissolved oxygen in micro(bio)reactor during the cultivation of *S. cerevisiae*. 64

Figure 4.1: (a) Scheme of microfluidic cell culturing system including two parts: generation of droplets and incubation of colonies; (b) zoom-in of detection unit in the incubation part including measurements for Optical Density (OD) and concentration of oxygen in droplets; (c) picture of tubings connected by customized fluidic connectors and with Piccolo2 placed next to it and fixed by a homemade holder (only bottom part is shown). 72

Figure 4.2: (a) Illustration of corresponding phase shift angle and signal intensity recorded when measuring at different positions of droplets or oil. High signal intensity indicates measuring in cylindrical body of the droplet. Low signal intensity indicates measuring at caps of the droplet. When measuring at oil, there is negligible signal intensity. (b) Example of online sensing data of a train of droplets. Phase shift angle is recorded into log only when signal intensity is above 40 mV. The average value of phase shift angle of this train of droplets is 53.27 ± 0.18 degree. 76

Figure 4.3: Monitoring of OD (Top) and concentration of oxygen (Bottom) during 24 hours incubation of control set of droplets and experiment set - droplets seeded with *E. coli* ATCC35218. 77

Figure 4.4: Monitoring of OD (top) and concentration of oxygen (bottom) during 96 hours incubation of control set of droplets and droplets seeded with *M. smegmatis* PCM661; inset: OD measurement of each of 10 droplets seeded with *M. smegmatis* during 96 hours incubation. 79

Figure 4.5: A full calibration for PSPVP oxygen sensor nanoparticles at 20 °C and 37 °C to determine values for$KSV1$, $KSV2$ and f. Oxygen sensor nanoparticles are dispersed in DI water in a closed glass vial. Gases with different concentrations of oxygen are flushing through oxygen sensor nanoparticles dispersion to obtain different air saturation level in the dispersion. Calibration gases are produced by mixing nitrogen and compressed air using a computer controlled gas mixing device (Vögtlin Instruments, Switzerland). Phase shift angle (dphi) are recorded by Piccolo2 to calculate lifetime of oxygen sensor nanoparticles at different concentrations of oxygen. 84

Figure 4.6: Full calibration of oxygen sensor nanoparticles before and after autoclave (5 cycles of autoclaving of 15 minutes at 121°C). Very similar oxygen sensitivity is shown by comparing calibration curves. Oxygen sensor nanoparticles remain nearly same properties after autoclave. 85

Figure 4.7: (a) Survival rate of Gram-negative and Gram-positive bacteria: *Escherichia coli* ATCC 35218 and *Staphylococcus epidermidis* DSMZ 20044 after 18 hours incubation at 37°C in the suspension of oxygen sensor nanoparticles in LB (Luria/Miller) medium (Roth, Germany) at a series of multiple dilutions; (b) Growth curves of *E. coli* ATCC 35218 in LB media and in LB media with oxygen sensitive nanoparticles (at concentration 1 mg/ml) for 24 hours incubation at 37°C. 86

Figure 4.8: Kinetic of oxygen transfer from air saturated carrier oil (FC40) to oxygen low aqueous droplet while moving in the bacteria incubation part of microfluidic culturing system. 87

Figure 4.9: Schematics of experimental procedure for generating low oxygen droplet: a) droplets generation module was left over night in sodium sulfite solution (1 wt%) to remove oxygen from material structures, b) in next step water solution with NPs which was initial deoxidize by argon was sucked *via* syringe pump to aspiration tube and left until rest of oxygen was removed by surrounding sodium sulfite, steps (c-d) were performed automatically controlled by custom LabView program. c) water solution was driven by oil to detection point, d) when oxygen level was lower than 50mM then valves switched occur and droplet was formed (e). Figures (f-h) shows cycling of droplet with possibly higher frequency of passing under detection point (~1.5 Hz). 89

Figure 4.10: Oxygen concentration in Teflon FEP tubing (ID = 0.8 mm, OD = 1.6 mm) after filling with water with low concentration of oxygen. 90

Figure 4.11: (a) Oxygen concentrations in each of the droplets seeded with *E. coli* ATCC35218 between 12 to 24 hours of incubation. (b) Ten consecutive measurements of oxygen concentration in each of the ten droplets seeded with *E. coli* ATCC35218 during one hour (hour 16.7 – 17.6) of incubation. 91

Figure 4.12: Technical drawing of Teflon FEP connector (unit mm). 92

Figure 5.1: Illustration of modified dual lifetime referencing method. F represents the signal from short-lived indicator; P represents the signal from long-lived indicator; TS represents the total signal. 100

Figure 5.2: 3D calibration surface for pH and concentration of oxygen dual sensor nanoparticles. 101

Figure 5.3: Boltzmann function fit for calibration of measurement of pH. 102

Figure 5.4: Comparison of measurement of pH in bulk and in droplets. 103

Figure 5.5: Scheme of the microfluidic culturing systems. 104

Figure 5.6: Workflow for data selection from each droplet. 106

Figure 5.7: Illustration of experiment of incubation of droplets with different composition i) seeded with *S. aureus*, ii) seeded with *S. epidermidis*, iii) seeded with no cells in single batch of cultivation. 107

Figure 5.8: Measurement of the concentration of oxygen, pH and optical density in droplet culturing *S. aureus*, *S. epidermidis* and control group. 108

Figure 5.9: Signal of pH measurement on the calibration droplets over 18 hours. 110

Figure 5.10: Signals from modified dual lifetime referencing method of samples with single ingredient of chapman medium. 111

Figure 5.11: emission spectra (exc: 617 nm) of sample AR5 (no Tween 80) and AR6 (with Tween 80).......... 112

Figure 5.12: Calibration curves of pH sensor nanoparticles in adapted chapman medium with high concentration of NaCl and low concentration of NaCl. 113

Figure 5.13: Monitoring of temperature during incubation of cells in droplets. 121

List of tables

Table 2.1: Commonly used optical oxygen indicators shown in microfluidic system application used either as indicator dissolved in the sample or embedded into a host polymer. 22

Table 3.1: Composition of different sensor cocktails and cocktails for primary layer used for microdispensing. 49

Table 3.2: Settings for different cocktails for microdispensing. 49

Table 4.1: Comparison of signal (phase shift) recorded from oxygen sensor nanoparticles and calculated lifetime (τ) from the same solutions at oxygen free and air saturated conditions of settings i) in a bulk solution, ii) in continuous flow in a tubing, and iii) in microdroplets flowing in a tubing. 74

Table 5.1: Parameters for Boltzmann fitting for calibration of pH sensor nanoparticles with different indicator dye entrapped. 102

Table 5.2: compositions of samples for experiment to check the effect of chapman medium on pH sensor nanoparticles. Each sample only contains a single ingredient from adapted chapman medium. 110

Table 5.3: Composition of adapted chapman medium by A. Ruszczak. 120

List of abbreviations

µTAS	micro Total Analysis Systems
PtTPTBPF	Platinum(II) *meso*-tetra(4-fluorophenyl)tetrabenzoporphyrin
NIR	near-infrared
LED	light-emitting diode
HPTS	Hydroxy-1,3,6-trisulfonic acid
aza-BODIPY	BF_2-chelated tetraarylazadipyrromethane
PET	photoinduced electron transfer
LOC	Lab on a chip
PS	Polystyrene
PDMS	poly(dimethylsiloxane)
PtOEPK	Platinum(II) octaethylporphyrin ketone
RTDP	ruthenium tris(2,2'-dipyridyl) dichloride hexahydrate
RIE	reactive ion etching
FLIM	fluorescence lifetime imaging
LbL	layer-by-layer
DO	dissolved oxygen
RLD	rapid lifetime determination
mMR	microreactor
PFE	perfluorinated elastomer

PPB	potassium phosphate buffer
PEI	poly(ethyleneimine)
GOX	glucose oxidase
CNC	computerized numerical control
kLa	volumetric mass transfer coefficient
OD	optical density
OTR	oxygen transfer rate
FEP	Fluorinated Ethylene Propylene
ID	inner diameter
OD	outer diameter
PSPVP	poly(styrene-block-vinylpyrrolidone)
AI	Artificial Intelligent

1 Introduction

1.1 Significance/Motivation

Since the development of micro Total Analysis Systems (µTAS) in the early 90s [1,2], the reactions or processes at micro scale have attracted a lot of attention. They offer some unique features, which are not common in macro scale. For example, low Reynolds number (i.e. laminar flow), and fast mass and heat transfer, which increase the efficiency for many processes. The small footprint is also a great advantage that microfluidics offers over large-scale approach. It is not the first time researchers try to bring their work in small dimension. If we have a look at our bench, this effort has been made from bringing fermenters to flasks to micro well plates. Scale down is as important as scale up. The scale down not only increases the efficiency, but also prevails some information that has not been shown before. One great interesting area for research on microfluidic platform is the study on single-cell level. By separating cells, researchers are able to show the heterogeneity among the same type of cells. This piece of information was overlooked or was not available before. But now microfluidics offers the possibility to dig into the big data for more profound discovery.

One challenge for microfluidics is the lack of monitoring tool. Monitoring of the process is critical for many applications. For example, many parameters including the dissolved oxygen level and pH are important during biological experiments. The concentration of oxygen and pH are the most widely monitored parameters in (bio)processes. The oxygen is the most essential element for most living organisms. pH is relevant to so many processes or detection of the analytes which cause the change of the concentration of hydrogen ion. One bench-top fermenter is usually fully equipped with sensors. The implementation of sensors for reactions at small scale is also essential. Without sensors, each microfluidic device is like a black box for operator, there is no information available during the process in the reactor. This challenge of implementing sensors comes from the small size of microfluidics. Most of the sensors for conventional experimental setup are not suitable for microfluidic systems. For example, the commonly used glass electrode pH meter is too bulky for microfluidic systems. Another difficulty is the high requirement of the performance of the sensors. The reaction or process is developing in a short time-scale in the microfluidic systems. The sensors need to be fast enough to show the change of the concentration of the analytes. And the amount of samples is usually very limited. It requires the sensors have high sensitivity and selectivity.

Optical chemical sensors are a good candidate for sensing in microfluidics. They are usually easy to miniaturize, have short response time, high sensitivity, and non-invasive measurement. So here we explore the integration of optical sensors in microfluidics and its applications for monitoring (bio)processes.

1.2 Scope and outline of the dissertation

In this thesis, we discuss the application of integrated optical chemical sensors in microfluidic system for biological experiments. Different types of sensors have been integrated in microfluidic system for sensing. Here, we will only focus on the optical sensors. It is worthy to mention that we will not discuss the usage of fluorescent probes microfluidic systems. For the microfluidic systems, we will show an example of tailor-made flow cell chip, an example of a sub-milliliter bioreactor, and in droplet microfluidics. The droplet microfluidic system is a droplet-on-demand system with droplets in the volume of microliter. There are many more types of microfluidics systems. Each of them may be made in different materials, be fabricated in different methods, and have different formats. We hope the examples we presented in this work can provide readers an overview of various applications of integrated sensors in different microfluidic systems. Different microfluidic systems serves for different purposes. Some are for fundamental studies of physics (i.e. transportation, hydrodynamics), some are for chemical synthesis, some are for intensification of bioprocess, and so on. Here we mainly focus on the applications of biological experiments, particularly, cultivation of cells, including bacteria and yeasts.

In this chapter, we provide the basic theoretical background including optical chemical sensors and microfluidics systems. In chapter 2, we give a review for the recently updates on oxygen imaging in micro(bio)reactor and microfluidics systems. We show two examples of oxygen sensing for bioprocess analysis in micro(bio)reactor in Chapter 3. One example is enzymatic reaction in flow cell chips. The other example is cultivation of yeast in micro(bio)reactor. In Chapter 4 and Chapter 5, we use oxygen and pH sensor nanoparticles for monitoring the concentration of oxygen and pH, respectively, in a droplet-on-demand system for bacterial incubation. Last but not least, we conclude the applications of sensor-integrated microfluidics for biological experiment, and an outlook of potential challenges and opportunities.

1.3 Optical chemical sensors

The definition of chemical sensors is “miniaturized devices that can deliver real time and on-line information on the presence of specific compounds or ions in even complex samples.” [3] A sensor system usually consists of three main parts: the sample (analyte), transduction platform, and signal-processing step. The optical chemical sensors are the sensors employ optical transduction methods to yield information on analytes. Many reviews have addressed the advantages of optical technique over other techniques for transduction [4–8]. And optical chemical sensors have been applied to different fields including chemistry, biology, medicine, marine science, biotechnology etc. Optical chemical sensors are based on indicators those change their optical properties (usually absorption or luminescence) according to different concentration of analyte. The optical transducer then converts the optical signal into electronic information.

1.3.1 Optical oxygen sensing

The most widely adapted principle for optical oxygen sensing is the dynamic quenching of luminescence intensity and lifetime of the indicator by molecular oxygen. In the present of oxygen molecular, the excited molecules of luminophore are quenched from triplet state to ground state. And this energy is transferred to excite oxygen molecules from triplet state (ground state) to singlet state (excited state). The decrease of luminescence intensity and lifetime is proportional to the concentration of oxygen, and it is described by two-site Stern-Volmer equation [9]:

$$\frac{F_0}{F} = \frac{\tau_0}{\tau} = (\frac{f}{1 + K_{SV1} \times [O_2]} + \frac{1 - f}{1 + K_{SV2} \times [O_2]})^{-1}$$

where F_0 (τ_0) and F (τ) are the luminescence intensities (lifetime) in the absence and presence of the quencher, oxygen; K_{SV1}andK_{SV2} are the Stern-Volmer constants, which describes the quenching efficiency for two micro-environment; f is the distribution coefficient between the two media, and $[O_2]$ is the oxygen concentration in the sample.

The oxygen indicator we used in this thesis is Platinum(II) *meso*-tetra(4-fluorophenyl)tetrabenzoporphyrin (PtTPTBPF). The indicator PtTPTBPF is excited by red light and emits in near-infrared (NIR) wavelengths (above 700 nm). This range of frequencies is particularly compatible with measurements on biological systems because it minimizes background fluorescence and has little interference with cells.

1.3.2 Optical pH sensing

Optical pH sensing usually means using some material changing its optical properties to different concentrations of hydrogen ions to indicate different values of pH. A common group of optical pH sensors is colorimetric-based. These optical pH sensors show different pH-dependent absorption (reflectance) change. Colorimetric-based pH sensor is not able to provide quantitative information of pH. And it is easily affected by scattering light (e.g. luminescence from biological matters). The major type of optical pH sensors is dependent on the detection of the change of fluorescence intensity or lifetime of the indicator dye. There are several popular pH indicator dyes on the markets, but they all have their drawbacks. Carboxy-fluorescein has moderate photostability and is prone to self-quencing. Hydroxy-1,3,6-trisulfonic acid (HPTS) is highly ionic strength dependent. SNARF is not photostable. Naphthalimides has low molar absorption coefficient. And all of these dyes have wavelengths of absorption/emission in the UV/Vis range (400 – 600 nm). This range is overlapping with the autofluorescence from biological matters. But for measurement in biological samples, red light excitable and Near-infrared (NIR) emission are desired. Because they have less interference with biological samples, less damage to the cells, and deeper penetration in biological samples than lights in the range of UV/Vis [10].

Former member of our group Jokic et al. [11] developed a series of new BF_2-chelated tetraarylazadipyrromethane (aza-BODIPY) dyes for pH sensing. This series of dyes has great optical properties regarding molar absorption coefficient, quantum yields, photostability. Also they show low cross-sensitivity to ionic strength and absorb red light and emit in NIR. The principle of aza-BODIPY dyes are based on photoinduced electron transfer (PET) mechanism [12,13]. The PET-based fluorophores usually have a receptor-spacer-fluorophore architecture and switching on-and-off property of fluorescence. Briefly, when there is no quencher present, an electron transfers from PET group to the fluorophore and occupies the ground state. As a result, the radiative relaxation via fluorescence is inhibited. When there is quencher present, the free electron pair of the PET group is electronically lower than the ground state of fluorophore. Therefore, the radiative relaxation via fluorescence is possible. For pH sensing, the high intensity of fluorescence is observed when there is low concentration of hydrogen ions. The relation between pH and phase shift measured can be described by Blotzmann sigmoid function, as shown below:

$$\cot(\varphi) = A_2 + \frac{A_1 - A_2}{1 + e^{\frac{(x - x_0)}{d_x}}}$$

where A_1 and A_2 are top and bottom value, respectively; x_0 is the apparent pKa value (the point of inflection); x is the pH value measured; and d_x is the slope at the point of inflection.

Another key component for optical pH sensor is the polymeric matrix for dye immobilization. Similar to the optical oxygen sensor, the indicator dye should not leach from the polymeric matrix to maintain constant concentration in the matrix. The material of matrix need to be hydrophilic to provide i) good dispersibility in aqueous phase, ii) good permeability to hydrogen ions. Most of the pH indicators are immobilized in hydrogel [14]. Another consideration need to be addressed here is the adhesion between substrate and sensor matrix. In this thesis, we used silicon hydrogel and core-shell-structured microbeads for the immobilization of pH indicator dye.

1.3.3 Detection methods

Most of the detection methods for optical sensors are either luminescent intensity-based or lifetime-based measurement. Luminescent intensity-measurement is a straightforward approach. It measures the change of luminescent intensity and correlates it to the concentration of analytes. This method requires persistent optical properties during the whole period of the measurement. For example, the instrument should provide constant intensity of excitation light source; the ambient light should stay the same, the dye concentration should not change; the turbidity of the sample should not change etc. These conditions sometimes are hard to maintain during experiments, especially working with biological matters. Ratiometric measurement can reduce the influence from these changing optical conditions. But it has high requirement of the design of the sensing chemistry to be suitable for ratiometric sensing.

Lifetime-based measurement, on the contrary, is based on the intrinsic properties of the luminescent dye. So it provides more accurate measurement.

Two dominant methods for lifetime-based measurement are time-domain and frequency-domain measurements. For time-domain lifetime-based measurement, it excites the sample with a pulse of light, and measures the time-dependent intensity after the excitation. The decay time is then calculated from the time-dependent intensity. For frequency-domain lifetime-based measurement, it excites the sample with intensity-modulated light (e.g. sine-wave modulation). Then the emission responds at the same modulation frequency. But the lifetime of the fluorophore causes the delay of emission from excitation. This delay in time is recorded as phase shift information and used to correlate to the concentration of analytes.

$$\tau = \frac{\tan \varphi}{2\pi f}$$

Where τ is the decay time (lifetime), φ is the phase shift, and f is the modulation frequency.

1.4 Microfluidic systems

Miniaturization has always been a demand for high knowledge-based industry. For the semiconductor industry, due to the miniaturization of integrated circuits, the size of a single transistor has decreased from 10 μm [15] to 22 nm [16] during the last four decades. This technology is so attractive that many other fields can also benefit from it, e.g. analytical chemistry. Why miniaturization is important and beneficial for analytical chemistry? Because microfluidics work with very small amount (10^{-6} to 10^{-18} liter) of fluids. This feature gives the capabilities: i) to analyze samples in limited volume; ii) to save the cost of expensive reagents; iii) to increase the throughput of analysis, iv) to leave small footprint for the analytical devices; v) to reduce the safety risk of working with toxic or explosive samples; vi) to increase yield by parallelization. From analytical and economic point of view, microfluidic technology is so convincing for researchers to adapt it into analysis in chemistry, biochemistry, biology and physics.

Microfluidics is a highly inter-disciplinary field. It requires the knowledge from chemistry, physics, biology, engineering and computer science. For the design of the microfluidics devices, it requires one to have good understanding of small scales and transport phenomena. For different applications of microfluidic devices, it requires the operator has the corresponding knowledge in the field. And the expertise in computer science helps to improve the design of the device with simulation tool, the automation level of microfluidic systems and data analysis.

1.4.1 Continuous flow microfluidics

Continuous flow microfluidics means there is only one kind of phase flow continuously in the microfluidic device. The significant difference between macro scale and micro scale for fluid is the viscous forces become dominant, instead of inertial forces. The ratio of inertial force and viscous force is defined by the Reynolds number (*Re*). The Reynolds number is a dimensionless parameter to define the transition from laminar to turbulent regimes. It is defined as:

$$Re = \frac{ud}{v}$$

where u is the velocity of the flow, v is the kinematic viscosity, and d is the channel dimension.

The flow is usually considered laminar flow in microfluidic channel. In this situation, the only way to mix two fluids in the channel is diffusion, instead of convection. The diffusion is a rather slow process in macro scale, but it is a fast process when the distance for diffusion is small (e.g. 100 µm). This phenomenon allows performing and controlling chemical reaction, especially for synthetic chemistry, in microfluidics.

The one major drawback of single-phase microfluidics is the Taylor-Aris dispersion. It is an effect in fluid mechanic that the shear force increases the effective diffusivity [17,18]. For example, there are two species (red and blue in Figure 1.1) in the continuous flow. The middle of the channel has enhanced mixing of two species due to strong shear force. And this effect causes the uneven distribution of the species in the tubing. Taylor dispersion can be suppressed by using droplet-based microfluidics.

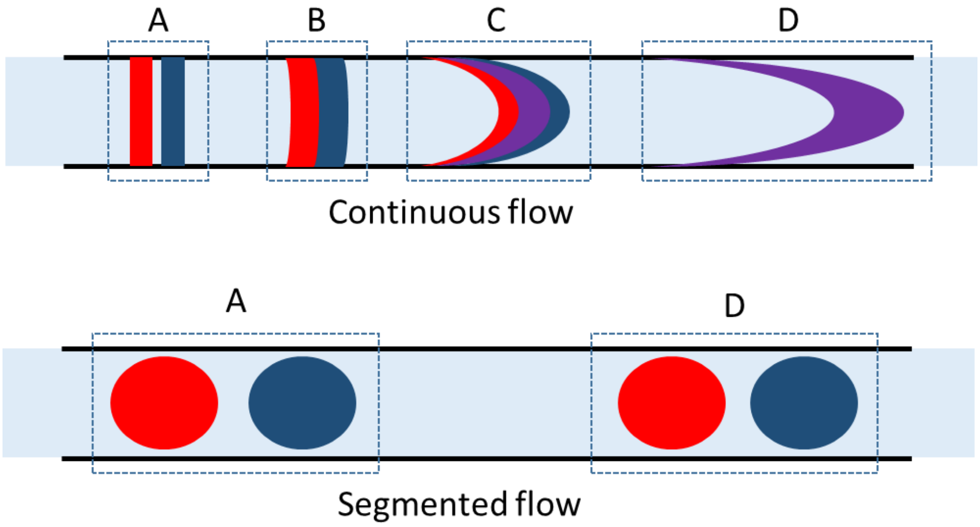

Figure 1.1: A scheme of two kinds of fluids in continuous flow and in segmented flow. Parabolic flow and Taylor-Aris dispersion [17,18] cause the mix of two fluids in continuous flow, but not in segmented flow (droplet microfluidics). This scheme is created based on the image published by Casadevall I Solvas and deMello [19].

1.4.2 Droplet-based microfluidics

Droplet-based microfluidics contains two immiscible phases. Usually the continuous phase is a hydrophobic fluid, such as fluorinated oil; and the disperse phase is an aqueous phase. The generation of the droplet is usually a spontaneous process from the shear force and interfacial tension at liquid-liquid interface. The two most common channel geometries for droplet generation are T-junction and flow focusing [20,21]. Droplet-based microfluidic is an alternative approach to continuous flow microfluidics. Each droplet in the flow is considered as a separated confinement. All the molecules of the samples stay in the aqueous phase (droplet), so Taylor dispersion doesn't happen in this case.

Droplet microfluidics have been extensively applied in chemistry and biology[22–27]. The isolated compartment gives the possibility to study single or small population of cells or molecules. This feature of droplet microfluidics provides more profound information on single cell or single molecules level, which is difficult to address by conventional approaches (e.g. experiments in flask, or micro well plates). Additionally, droplet microfluidics allows one to perform experiments in large quantity. If we consider each droplet as a (bio)reactor, we can perform thousands or millions times of experiments. This amount of experiments generates great amount of data, which is extremely valuable in the ear of information.

1.5 Integration of sensors in microfluidics

The integration of optical chemical sensor into microfluidics is critical and challenging. Gruber et al. summarize the way to integrate sensor into micro(bio)reactor and its application [28]. It gives a good tutorial overview on how to combine the sensor technology and microfluidics systems. The challenges for the sensor integration can be divided into the following perspectives: i) deposition of sensor material in micro scale structure; ii) physical and chemical stability of sensor material during operation of microfluidic systems; iii) compatibility of sensors with fabrication methods; iv) detecting methods; v) limit of detection.

1.5.1 Deposition of the sensors

For different formats of optical sensors, there are different ways to integrate them with microfluidic system. For planar sensor, it is possible to deposit sensor material on the substrate and then put the substrate into the microfluidic device. For example, one can knife-coat sensor material on the PET foil. Then cut the foil and glue it into the microfluidic channel [29]. The advantage of this method is easy preparation. The substrate with deposited sensor can be prepared in advance. The substrate can be cut into different shape to fit different microfluidic structure. And since the sensor is not directly attached to the microfluidic device, the adhesion is only between substrate and microfluidic device. In this case, glue or double-side tape can be used, which is very simple. The sensor is not contact with glue, so it is not a concern about the effect of glue on sensors. But this method is not working with fine structure of microfluidics. For example, for tiny channel or cavity in microfluidics, the sensing material can be directly dispensed into the microfluidic system by air-spray or micro-dispensing. This approach requires a good design in chemistry. A suitable solvent need to be soluble for sensor material and do not destroy the chip structure. After dispensing, the solvent evaporates, the sensor material stays on the chip. This tactic also requires a lot of experience with the setting of the parameters with the dispensing machine to have a desired formation of the sensor on the chip.

For droplet microfluidics, the only way to integrate sensors is to disperse sensor in the aqueous phase. The luminescent probe molecules can be dispensed directly in the aqueous phase[30–32]. But dye material is usually hydrophobic. It has poor solubility in aqueous phase and can leak into the surrounded organic phase. And the biological samples, which usually have a complex composition, could have interference on the sensor since they are directly in contact. Cao et al.[33] and Funfak et al.[34] have the dye entrapped in hydrophilic polymers and then disperse the polymer in aqueous phase for sensing in segmented flow. This method overcomes the problems of low solubility and leakage of the probe, but the stability of the sensor material in the polymer has to be improved. Another elegant approach is to embed the indicator dye in the nanobeads. Ehgartner et al.[35] and Horka et al.[36] show the use of core-shell structured nanoparticles to encapsulate indicator dye. The hydrophilic shell of the nanoparticles gives good dispersibility in aqueous phase; the lipophilic core of the nanoparticles is ideal for encapsulation of hydrophobic dye material. This tactic not only solves the problem of solubility and leakage of the dye, but also shields the indicator dye in nanoparticles from complex samples.

The nanoparticles have also been used in the continuous flow microfluidic system. Ungerböck et al.[37] reported using magnetic sensor nanoparticles to form a spot for sensing. A unique approach reported by Lasave et al.[38] is directly applying the sensor dispersion in the microfluidic device and incubate the chip for several hours. The reported conjugated polymer-based sensor has great adhesion on glass surface. The biggest advantage of this approach is capability to integrate the sensor into microfluidic system after fabrication of the device.

1.5.2 Physical and chemical stability of the sensors

The sensors need to remain stable both physically and chemically in the microfluidic systems. For example, in flow cell chips, the fluid passes through the channel at a relative high linear velocity over the sensor. The generated shear force can wash sensor material away, which is not wanted. To avoid this, the sensor needs to have sufficient adhesion on the chip at operating condition. Surface modification plays a role here to change certain property of the surface of the chip for a better adhesion for the sensor. The simplest way would be physical modification, for example roughing the surface. Chemical modification is also used, for example sanilizaiton of glass surface.

The chemical stability means the sensor should maintain its sensing ability during the operation of microfluidic systems. The sensors are usually in direct contact with samples. For biological samples, the cells or the proteins excreted by the cells can interact with sensors. It is a good shield for sensor materials if they are encapsulated in the nanobeads, and covalent bonding is desired.

1.5.3 Compatibility of the sensors with fabrication methods

The fabrication of microfluidic devices can involve some harsh conditions. Most of the sensors for microfluidic devices are integrated before the fabrication. In another word, the sensors have to survive the fabrication process. Different materials of the chips require different methods for fabrication. It is case by case solution to decide in which step of fabrication to integrate the sensors.

Another process during the preparation of microfluidic system is sterilization. It is a key step for working with biological materials to avoid contamination. Autoclave is a common technique to sterilize different materials. A sensor can survive the sterilization process is definitely desired.

1.5.4 Detecting methods

Optical sensors are detected by the optical measurement. The material of the microfluidic devices, the solutions used can affect the optical measurement. Most of the microfluidic devices are made of transparent material, for example thermoplastic material or glass. For tubing-based microfluidics, sometimes the tubing is not completely transparent. For some 3D printed microfluidics, the used resin may have luminescence. For droplet microfluidics, there is more than one fluid in the system, typically oil and water, or water and air. These fluids have different reflex index and affect the optical signal acquired. It is necessary to check if there is any interference from the chip to optical measurement.

Another concern for detection unit is the placement of the readout device. Most microfluidic systems are small, and connected with many tubes. Sometime it is difficult to find a proper place for the readout device. So it would limit the “window” for detection. In this case, a miniaturized readout device is desired to be compatible with microfluidics.

1.5.5 Limit of detection

One of the advantages of microfluidics is fast mixing and heat transfer. These advantages lead to rapid chemical or biological process. This fast reaction requires the sensors have a short response time. Otherwise, the sensors cannot provide reliable real time and on-line information of analytes. Beside the fast response time of sensors, the fast measurement is also important. The frequency of measurement can be critical for droplet microfluidics. One feature of droplet microfluidics is high throughput. Every second, the droplets generated can be 10 thousand or more. This high frequency of generation requires the detecting unit also has the same frequency for measurement.

2 Imaging of oxygen in microreactors and microfluidic systems

Chapter 2 has been published in full under the citation:

Sun, S., Ungerböck, B., & Mayr, T. (2015). Imaging of oxygen in microreactors and microfluidic systems. *Methods and Applications in Fluorescence*, 3(3), 034002.

doi: 10.1088/2050-6120/3/3/034002

Abstract

This review gives an overview on the state-of-the-art of oxygen imaging in microfluidics. Oxygen imaging using optical oxygen sensors based on luminescence is a versatile and powerful tool for obtaining profoundly space-resolved information of oxygen in microreactors and microfluidic systems. We briefly introduce the principle of oxygen imaging and present techniques of oxygen imaging applied in microreactors and microfluidic devices, including selection criteria and demands of sensing material and basic set-up for a 2D oxygen sensing system. A detailed review of oxygen imaging in microreactors and microfluidic systems is given on different applications in oxygen gradient monitoring, cell culturing, single-cell analysis and chemical reactions. Finally, we discuss challenges and trends of oxygen imaging in microfluidic systems.

2.1 Introduction

The development of the miniature GC air analyzer on a silicon wafer at Stanford University [39], and the planar silicon ink-jet printer at IBM [40], opened the door for microfluidic research. It had turned into a 'hot' research topic in the early 1990s, when Manz et al proposed the concept of a 'miniaturized total chemical analysis system' [1], which is more recently known as 'micro Total Analysis Systems' (µTAS) or 'Lab on a chip' (LOC). In general, microfluidic systems involve the manipulation of liquids and gases in micro-sized channels (typical cross-sectional dimension in the order of 10–500 µm). During the past decades, with the dedication of many researchers, these 'Lab on a chip' devices have been well studied [41,42] and applied to a rich field of applications, including drug discovery and combinatorial chemistry [43,44], chemical synthesis [45,46], tissue engineering [47], clinical diagnostics [48] and cell analysis [49,50].

Compared with conventional applied technology, microfluidic systems have some outstanding advantages: reduced consumption of reagents and analytes; increased efficiency in production, separation, analytical time; decreased cost in manufacture; portability; and the potential to establish reactions or process windows which cannot be conducted in macro-scale systems. Along with these benefits of microfluidic systems, miniaturized scales also bring up the challenge of detecting various analytes and physical parameters. A suitable sensor needs to have a sufficient sensitivity to a small amount of analytes available during measurement. Compared with conventional bench-scale systems, a decreased number of analyte molecules are detectable to sensors. Furthermore, different sensing components should be able to be scaled down to smaller dimension to fit in LOC devices.

Optical oxygen sensors are established in macro-scale applications found in biotechnology, chemical industry and environmental analysis, such as cell cultures, fermenters, batch reactors, waste water treatment, food packaging, pressure sensitive paints and marine research among others [51]. Optical chemical sensors are an attractive format for integration into microfluidic devices due to their features: highly sensitive, inexpensive, easy to miniaturize and non-invasive during investigation. They are also suitable for 2D mapping of oxygen concentration. Macroscopic imaging of oxygen has been reviewed by Schäferling [52]. The most common optical oxygen sensors comprise of a polymeric layer with an embedded indicator. The sensitivity depends on the luminescent properties of the indicator (lifetime) and the permeability of the polymer matrix. It can be tuned by varying these two components. This format makes optical oxygen sensors extremely attractive for integration into microfluidic devices because it can easily be miniaturized and can apply the dye doped polymer layer. Compared with electrochemical methods, optical oxygen sensors do not need a reference electrode and do not consume analytes. This can be crucial in micro-scale because of the low number of analytes available, which can bias an accurate detection. In addition, the ease of integration is beneficial when mass-production of the microfluidic devices for a broad group of consumers is kept in mind. The less complex the production of a microfluidic chip is, the cheaper it will be and the easier it can be accepted by consumers. For instance, during the application of cell culturing, microfluidic chips are usually treated as disposable because of sterilization issues. A lower cost of these chips is favored. The recent development on integration of optical oxygen sensors into microfluidic systems has been summarized [53,54]. Different aspects of optical sensors in micro-scale systems have been discussed, e.g. design, fabrication and calibration of microfluidic chips with integrated oxygen sensor [55,56], investigation of oxygen transfer characteristics in microfluidic systems [57,58], and oxygen level monitoring during cell culturing [59,60].

The combination of oxygen imaging and microfluidic systems is attractive for various reasons. Oxygen imaging is a versatile tool to monitor and control oxygen distribution with spatial resolution enabling more profound understandings of how microfluidic systems work (e.g. fluidic dynamic, concentration profile) differently from bench-scale reactors. In addition, applying oxygen sensor to microfluidic systems enables the investigation of complex correlations, e.g. the interaction of cells. Moreover, oxygen imaging can not only be used for microscopic imaging, but also 'macroscopic' imaging, which is capable to monitor oxygen gradients throughout the whole chip (see figure 2.1) [29].

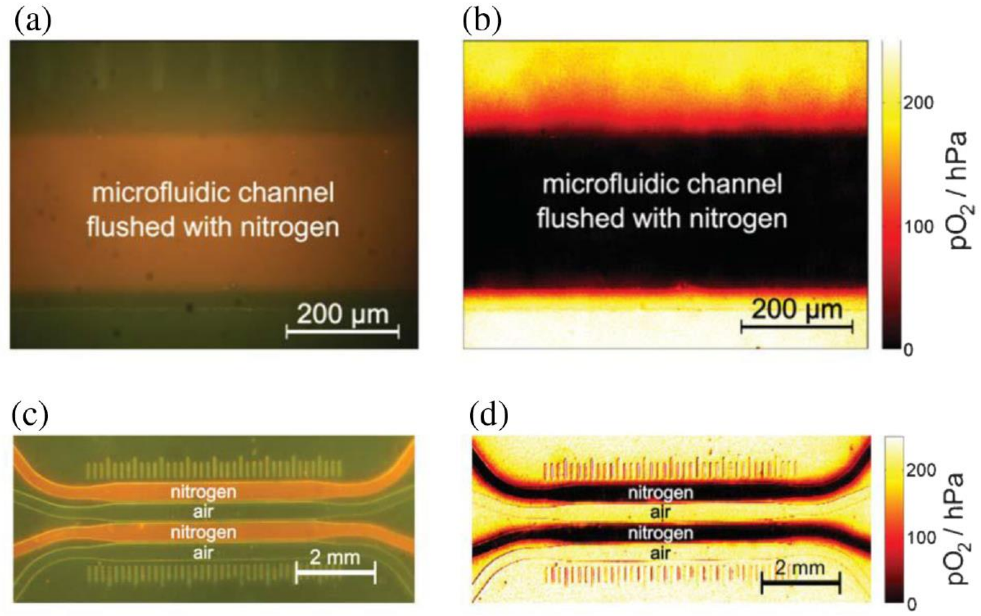
(a)
microfluidic channel flushed with nitrogen
200 µm
(b)
microfluidic channel flushed with nitrogen
200 µm
200
100
0
pO2 / hPa
(c)
nitrogen
air
nitrogen
air
2 mm
(d)
nitrogen
air
nitrogen
air
2 mm
200
100
0
pO2 / hPa

Figure 2.1: (a) Microscopic color (original) image and (b) calculated oxygen image of one channel of a microfluidic chip, which is flushed with nitrogen. (c) Macroscopic color (original) image and (d) calculated oxygen image of four channels of the same microfluidic chip; the first and third channels were flushed with nitrogen, while the other channels contained air (Reprinted from [29] with permission from Royal Society of Chemistry).

In this manuscript we focus on the application of optical oxygen sensors in microfluidic systems and microreactors (with a working volume less than 500 µL) with a view on 2D oxygen detection. We firstly give an overview of the selection of materials and formats that are used in microenvironment for oxygen imaging. Some fundamental knowledge of optical oxygen sensing is briefly presented. Then we focus on oxygen imaging in microfluidic systems, including oxygen sensing methods and measurement systems. After that reported applications of optical oxygen sensors in microfluidic devices for spatially resolved study are reviewed. Finally, a discussion of future trends and developmental challenges is given.

2.2 Oxygen imaging in microreactors and microfluidic systems

2.2.1 Oxygen imaging principle

The principle of oxygen sensing and imaging is collisional quenching of luminescence intensity and the lifetime of an indicator dye by molecular oxygen. The quenching behavior can be described by the Stern–Volmer equation [61]:

$$\frac{I_0}{I} = \frac{\tau_0}{\tau} = 1 + K_{sv} pO_2$$

where I_0 and I are the luminescence intensities in absence and presence of the quencher, τ_0 and τ are the luminescence lifetimes in absence and presence of the quencher, K_{sv} is the Stern–Vollmer quenching constant, which characterizes the quenching efficiency and therefore the sensitivity of the sensor and pO_2 is the partial pressure of oxygen.

Different sensing methods have been used for oxygen imaging. Intensity-based luminescent measurements have been widely used since it is straightforward and compatible with standard fluorescence microscopy setups. However, luminescence intensity measurements are sensitive to instrumental variations (e.g. excitation intensity, ambient light and detection efficiency) and are easily affected by varied dye distributions, photo-bleaching and scattering. Therefore, referenced detection schemes are preferred to overcome these drawbacks including lifetime measurements and ratiometric methods. Two different approaches are used for lifetime-imaging: time-domain and frequency-domain, but both of them require specialized and expensive equipment [62]. Ratiometric methods employ an oxygen-sensitive indicator and a reference dye with different spectral emissions and use standard imaging equipment. The ratio of emission of oxygen indicator and reference dye at two different wavelengths is used to calculate the oxygen concentration. This method reduces the effect of setup environment variations, like excitation light, inhomogeneities of dye distribution and sensor layer thickness. However, signal variations due to photobleaching or leaching of one luminophore, ambient light or wavelength-dependent scattering still have an influence on accurate analyte determination.

2.2.2 Sensor formats

The possibility of using various formats makes optical sensors a very versatile platform to integrate into microfluidics (figure 2.2). Most widely used formats include water-soluble indicators or molecular probes dissolved in fluid, integrated sensor layers and sensor particles. Each of these formats has its advantages and drawbacks due to its properties and working environment in microfluidic systems. Dissolved indicators are easy to apply to microfluidic systems, e.g. by mixing a stock solution with the sample stream. However, they require a high dye concentration, which makes them prone to interference with the sample, suffer from a low sensitivity and selectivity, potential toxicity, tendency to aggregation, liability to non-specific binding and restriction to water-soluble indicators only. Sensor layers, which have indicators encapsulated in a matrix, overcome these drawbacks and result in better sensitivity, higher signal-to-noise ratio, shielding from interference with sample and easy handling for the end-user. However, sensor layers or spots have some limitations in their dimensions, including longer response time than dissolved indicators or sensor particles and restriction to perform 2D imaging. Another versatile sensor format is sensor particles. It combines the advantages from both water-soluble indicators and sensor layers including shielding from interference from the sample and indicator dye, high selectivity, and high dye loading. Sensor particles exhibit higher signals, possibility for 3D imaging, versatility in tuning sensing properties within the polymer matrix, and last but not least, shorter response time for monitoring fast processes [63].

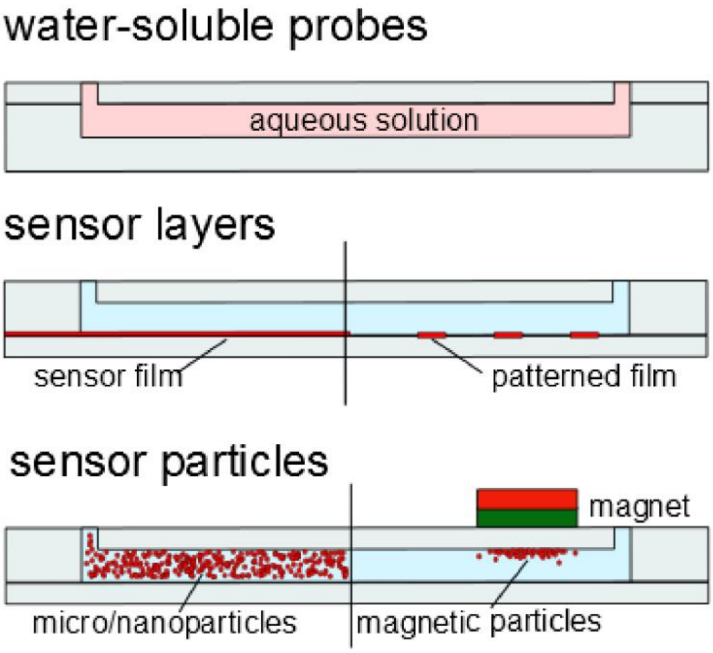
water-soluble probes
aqueous solution
sensor layers
sensor film
patterned film
sensor particles
magnet
micro/nanoparticles
magnetic particles

Figure 2.2: Different optical oxygen sensor formats used in microfluidic systems.

Oxygen indicators

Oxygen sensitive dyes are used as water-soluble probes or embedded in host polymers to form sensor layers or particles. The water-soluble indicator approach is straightforward but is compromised by the issues discussed above. Only a few reports make use of dissolved indicators for microfluidic oxygen imaging [59,64]. The number of available water-soluble indicators is limited and compromised by low quantum yields in water. Furthermore, most oxygen sensitive dyes are lipophilic and therefore are embedded into a host polymer. A systematical, detailed study of used optical oxygen indicator has been reviewed by Quaranta et al. [65], and some other review papers on optical oxygen sensing [51,52]. Commonly used indicators in microfluidic oxygen imaging are summarized in table 1. These oxygen indicators have been used for macro-scale applications before and were adapted into microfluidic format.

Table 2.1: Commonly used optical oxygen indicators shown in microfluidic system application used either as indicator dissolved in the sample or embedded into a host polymer.

Indicator	Sensor format	Encapsulated matrix	Reference
ruthenium tris(2,2′-dipyridyl) dichloride hexahydrate (RTDP)	Dissolved in PBS	N/A	59,64,66
Platinum(II) octaethylporphyrin ketone (PtOEPK)	Sensor layer	Polystyrene (PS)	55,56,67
Pt(II) meso-tetra(pentafluorophenyl) porphine (PtTFPP)	Sensor layer	poly(dimethylsiloxane) (PDMS)	68–70
	Sensor layer	Polystyrene (PS)	29,70,71
	Sensor particle	PSMA	37

Sensor layers

Sensor layers are the most commonly applied format of optical sensors in microfluidics. It can be deposited from a so-called 'sensor cocktail' (polymer matrix material, indicator and additives dissolved in a suitable solvent) onto a substrate by spin coating, screen printing, spray coating, knife coating, inkjet or pin-printing. The deposited film is then allowed to dry, polymerize or cure. The sensor layer can be used either as un-patterned film or patterned film. The latter can be fabricated either by coating only a small area or by completely coating a substrate followed by a lift-off process. Another possibility to create patterned sensors is to apply a photolithographic curing process of photo-patternable matrices.

Nock et al introduced novel methods for the fabrication of polymer microfluidic systems with polymer-encapsulated integrated optical oxygen sensors [55,56]. The full fabrication process is illustrated in figure 2.3. In this system, PtOEPK suspended in a microporous PS matrix was spin-coated onto glass substrates to form sensor films with the desired thickness. For sensor patterning, the PDMS stamp was brought into conformal contact with the PtOEPK/PS layer. The custom patterned sensor layer was created by reactive ion etching (RIE) and integrated with the fluidic parts by oxygen plasma bonding. This repeatable fabrication approach is used for measurement of locally varying oxygen distribution in microfluidic channels.

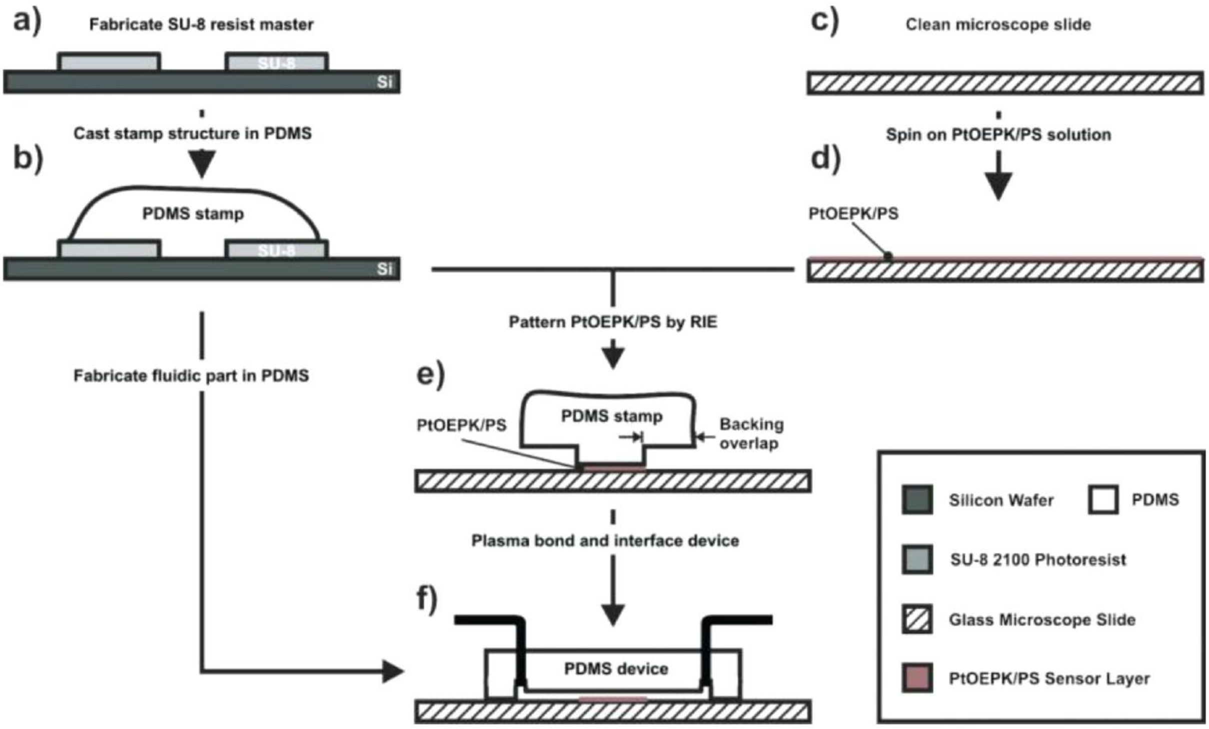
a) Fabricate SU-8 resist master
SU-8
Si
Cast stamp structure in PDMS
b)
PDMS stamp
SU-8
Si
Fabricate fluidic part in PDMS
c) Clean microscope slide
Spin on PtOEPK/PS solution
d)
PtOEPK/PS
Pattern PtOEPK/PS by RIE
e)
PtOEPK/PS
PDMS stamp
Backing overlap
Plasma bond and interface device
f)
PDMS device
Silicon Wafer
PDMS
SU-8 2100 Photoresist
Glass Microscope Slide
PtOEPK/PS Sensor Layer

Figure 2.3: Schematic of the sensor fabrication process depicting stamp fabrication in PDMS (a, b), spin-coating of the sensor layer (c, d), pattern transfer into the sensor layer by RIE (e), and integration with a PDMS microfluidic device by plasma bonding (f) (Reprinted from [56] with permission from Royal Society of Chemistry).

Furthermore, Nock et al. [67] introduced another simplified fabrication process: a thin-film sacrificial metal layer was used as an intermediate mask during the fabrication process to produce arbitrarily-shaped optical oxygen sensor patterns at micron resolution (feature sizes down to 3 µm). This potentially enables the integration of multiple sensor patches for single cell analyzing systems. Recently, Grist et al. [72] introduced a new method using mask-less laser ablation to pattern PS thin film and shows the compatibility with standard PDMS plasma bonding. The fabrication of layers is generally compatible with micro-fabrication techniques, which might facilitate their use. However, sensor layer integration adds one more step to chip fabrication. Another challenge is the integration of oxygen sensor into the microstructures. Until now, there is no satisfactory technique to integrate sensor layers into ready-made bonded devices.

Some general study on the impact of the sensor matrix on the performance of oxygen sensor was reviewed by [73]. More specifically, in previous applications in microfluidic oxygen imaging the most predominantly used polymer encapsulation matrices are polystyrene (PS) [55,56,60,74] and poly(dimethylsiloxane) (PDMS) [68,69,75–77]. Both of them show good oxygen permeability and bio-compatibility. But PDMS was reported to absorb hydrophobic small molecules and the consequences in microfluidic applications was discussed [78].

Sensor particles

Sensor micro/nanoparticles have become versatile analytical tools and that is why several reviews addressed their fabrication and application [79,80]. Various preparation procedures are reported, such as adsorbing indicator molecules to particle surfaces, polymerization, precipitation or grinding indicator-loaded matrix bulk materials. Sensor particles combine the advantages from dissolved indicators and indicator-encapsulated sensor layers. They can exhibit simple and flexible application in microfluidic systems just by adding to the fluid and provide an additional protection for interference by the sample. Compared to sensor layers, nanoparticles provide fast response in real time and enable monitoring of fast processes. Moreover, photo-bleaching plays a minor role since the sensing element is not static and permanently exchanged by the flow [81]. Magnetic particles combined with sensor properties are an elegant way to perform measurements in microfluidic channels [79]. They can be added to the fluid and be collected inside a microfluidic channel from outside by a magnet allowing the in-situ generation of sensor spots with high brightness at desired positions.

2.2.3 Challenges for oxygen imaging in microfluidics

Optical oxygen sensors are well suited for the application and integration in microfluidic devices. However, to fully exploit the potential of optical oxygen sensors in microfluidics the sensing chemistry has to fulfill several demands including high brightness, the capability to be applied as a thin film (below 1 µm thickness), good photostability, compatibility with sample, cheap or established imaging systems, simple and microfluidic production compatible preparation steps, compatibility with the chip materials and low or no toxicity.

The brightness of the applied sensors is critical because of the reduced dimension and limited working volume in microfluidic devices. Sensor layers or dissolved indicators might not deliver sufficient signals as commonly applied in a macro-scale. Microfluidic oxygen imaging benefits from recently published oxygen sensors with enhanced brightness [82,83]. Brighter sensors enable the preparation of thinner films compared to macroscopic sensors. This leads to fast response times or instant response. In most microreactor applications, it is necessary to follow reactions in real time. Herein, nanometer-thin sensor layers and nanometer-sized sensor particles employing the light harvesting principle to enhance the brightness have shown real-time response [84]. Brighter dissolved indicators or sensor particles can be applied in lower concentrations minimizing potential interference with the sample. Moreover, the detection system has to be compatible with the applied sensor chemistry. Apart from the spectral compatibility of the indicators with excitation sources, filters and detectors, the detection principle is critical. The drawbacks of intensity imaging were already discussed above. Lifetime imaging is the best choice but often not available for researchers because of the cost-intensive equipment. Recent development employs ratiometric imaging with color CCD cameras for a low cost approach [29].

In order to suppress background fluorescence or scattering from polymeric chip material or biological material, long-wavelength (above 600 nm) excitable and emissive indicators or sensor material is preferable. In addition, excitation with red-light excitation is less harmful for cells than UV or blue light. Promising indicators for such applications are NIR emitting probes such as Pt(II) and Pd(II) complexes with π-extended benzo-naphtoporphyrins [82], as well as azabenzoporphyrins [85]. However, it is important to mention that CCD chips of microscope cameras, as well as some photodetectors, exhibit low sensitivity in NIR dye's spectral region [54].

Another critical aspect is the microfluidic chip production and the chip materials. When sensor layers are integrated, sensor materials have to withstand steps of microfluidic chip production, e.g. bonding at high temperatures or plasma treatments. In addition, the chip materials have to be compatible with sensor materials. Background fluorescence from the chip material might hamper the detection by decreasing the signal-to-noise ratio. The adherence of sensor layer to microfluidic channel walls is critical since shear stress can lift it off. When indicators are not covalently bounded to sensor matrix, some sensor components can migrate into the chip material and influence long-term performance and shelf-life of sensors.

Another challenge for oxygen imaging is the possible falsification of experimental results by singlet oxygen. The dynamic quenching process of oxygen sensors causes the production of singlet oxygen. Ungerböck et al showed that in microfluidic devices the production of singlet oxygen can be critical due to the micro-scale and can bias the accuracy of detection [37]. The small amount of oxygen inside a microfluidic channel together with the high excitation light intensities of microscopic set-ups often used in microfluidic imaging leads to distorted results or degradation of the sensor materials.

Microfluidic systems often deal with biological or medical applications. Therefore, the toxicity of the integrated sensor materials is an important factor for an ideal sensing setup. Compared to the toxicity due to generated singlet oxygen, the toxicity due to the dye plays a minor role, because the dye is encapsulated in a polymer matrix and thus is excluded from direct contact with the investigated biological material. Also, singlet oxygen is considered toxic to biological substance [86]. Singlet oxygen, however, can diffuse through the matrix material and can negatively affect cell growth before it returns to its ground state. Possible ways to reduce toxic effects of singlet oxygen are to decrease excitation light intensities or the dye loading (leading to a reduced production of singlet oxygen) or to increase the diffusion path lengths between sensing layer and biological material to increase the probability for singlet oxygen deactivation.

2.3 Optical measurement system

The optical measurement system is another important component of oxygen imaging in microfluidic devices. According to Kuswandi et al. [87], it can be classified into two approaches: the 'off-chip' approach, where macro-scale excitation and detection techniques are coupled to micro-scale detection areas, and the 'on-chip' approach, which aims at direct integration of miniaturized excitation and/or detection techniques into microfluidic devices, which has not been realized for imaging yet.

It is advantageous to apply optical equipment already in use into microfluidic labs, such as fluorescent microscopes or other optical equipment. In microfluidic imaging the 'off-chip' is released since it employs available high performance instrumentation, e.g. fluorescence microscopes, applied with sensing chemistry or customized instrumentation.

A good example of typical, minimum 'off-chip' optical measurement setup is illustrated in figure 2.4. It consists of a light source to excite the indicator dye, a filter to detect only the emission light, a microscope for luminescence detection, and a camera for image recording.

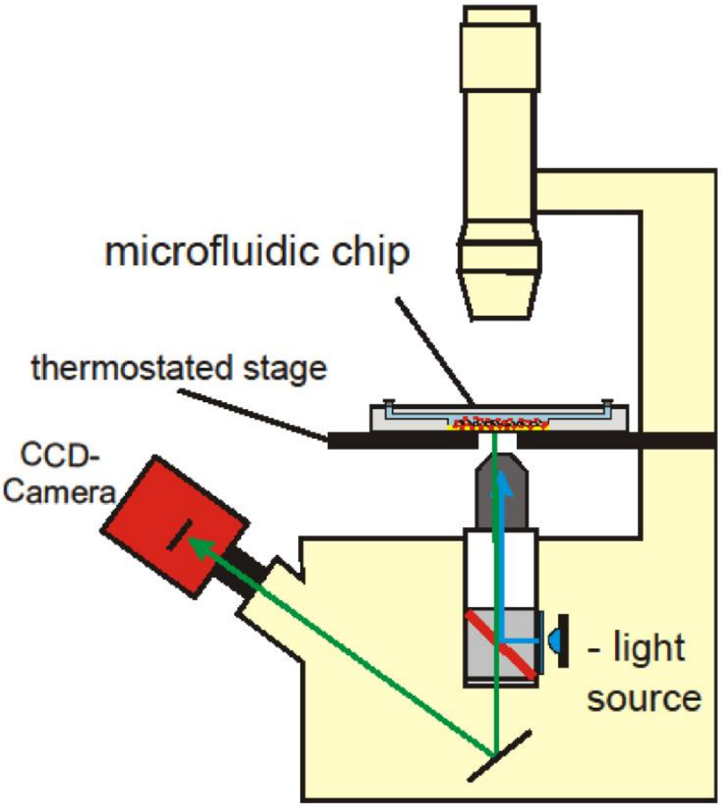

Figure 2.4: A typical setup scheme for oxygen imaging systems.

2.4 Application of oxygen imaging in microreactors and microfluidic systems

2.4.1 Monitoring oxygen gradients in microfluidic systems

Optical sensors have been applied to various microfluidic systems to monitor oxygen gradients with different sensing formats and detection methods. Park et al developed an oxygen microgradient chip, which employs electrolysis to control the oxygen microgradients within a tissue or culture sample without generating bubbles [88]. In this microsystem, the dissolved oxygen gradient (in the range of 0 to 40% dO2) was imaged by the luminescence intensity of a laminated oxygen-sensitive luminophore membrane (Oxysense, Inc), and employing a microscope with a CCD color camera (figure 2.5).

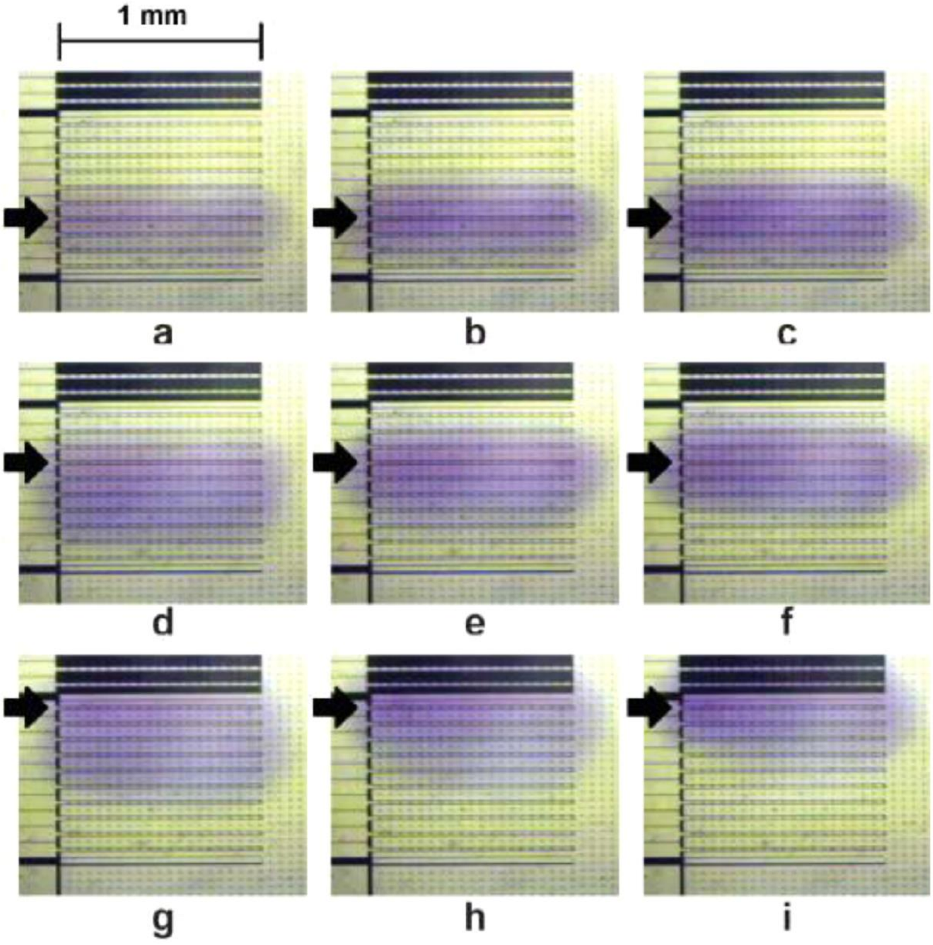

Figure 2.5: (a)–(i) Time-lapse images of the patterned oxygen microgradient as it is moved around using ten horizontal microelectrodes (each 20 mm 6 1 mm). Video capture frames are 20 s apart and were taken with a white light microscope (Reprinted from [88] with permission from Royal Society of Chemistry).

Laterally varying oxygen levels inside microfluidic devices were studied by Thomas et al. [68]. A new approach for regulating oxygen on a microfluidic chip was demonstrated by pumping pre-equilibrated aqueous solutions of different dissolved oxygen compositions through gas control channels to modulate the oxygen levels in neighboring stagnant chambers. To monitor the changing oxygen levels within the fluidic chamber in real-time and continuously, PtTFPP in PDMS thin film has been used as an oxygen sensor inside a PDMS device [69]. A multilayer sensor design, created by sandwiching the PtTFPP-PDMS with a layer of Teflon AF followed by a second PDMS layer, effectively mitigating the dye cytotoxicity while providing a substrate for cell attachment. This system uses an X-Cite metal halide as light source, and an inverted microscope and a CCD color camera to capture intensity imaging.

A method to generate oxygen and chemical concentration gradients in a single microfluidic device via the formation of an oxygen gradient in a chamber has been described by Wang et al [77]. A PDMS film containing PtOEP as oxygen sensor, a mercury lamp, and detection set up including an inverted microscope with a CCD camera are used in this system to perform intensity-based imaging. The oxygen gradient dynamics were quantitatively controlled using a simple exchange between the aerial oxygen and the oxygen-free conditions in the gas-permeable PDMS microchannel device and were systematically investigated. The device is suitable for potential medical applications. Ratiometric oxygen measurement, another possible method to overcome the drawbacks of intensity measurement, has been applied to oxygen imaging in microfluidic systems. Ungerböck et al. [29] applied a self-made sensing film of PtTFPP and a fluorescent reference dye in PS, employing the principle of light harvesting, to further increase signal intensity and a CCD color camera for relatively simple and low-cost yet reliable signal read-out. The sensing set up was used to monitor spatially varying oxygen levels of microfluidic systems containing human cell culture. In Ochs et al. [89], a computational model for estimation of cellular respiratory activity in microfluidic systems was verified using commercially available sensor foils and a commercially available imaging device.

Furthermore, Ungerböck et al. [37] evaluated multifunctional optical sensor particles (MOSePs) [90] with incorporated magnetic and sensing functionalities regarding their applicability in microfluidic devices. The magnetic properties of these particles served to separate the particles from the surrounding solution to form in-situ sensor spots within microfluidic channels, while read-out was accomplished outside the chip. These magnetic sensor spots exhibited advantageous features of sensor layers (high brightness, convenient usage) combined with the benefits of dispersed sensor particles (ease of integration). Different read-out methods were evaluated and critically discussed, including fiber optic as well as 2D read-out using RLD and RGB imaging.

2.4.2 Determination of oxygen concentration in microfluidic systems for cell culture

Microbial or mammalian cell culturing has been most commonly applied for microfluidic systems. Correspondingly, oxygen imaging has been conducted to study oxygen tension in microbioreactors. Sud et al. [59] performed oxygen imaging in a PDMS microbioreactor containing living cells by applying wide-field time-domain fluorescence lifetime imaging (FLIM) of oxygen-sensitive dye ruthenium tris(2,2'-dipyridyl) dichloride hexahydrate (RTDP) (figure 2.6). The single pixel lifetime values were used for obtaining an average signal over the whole detection area.

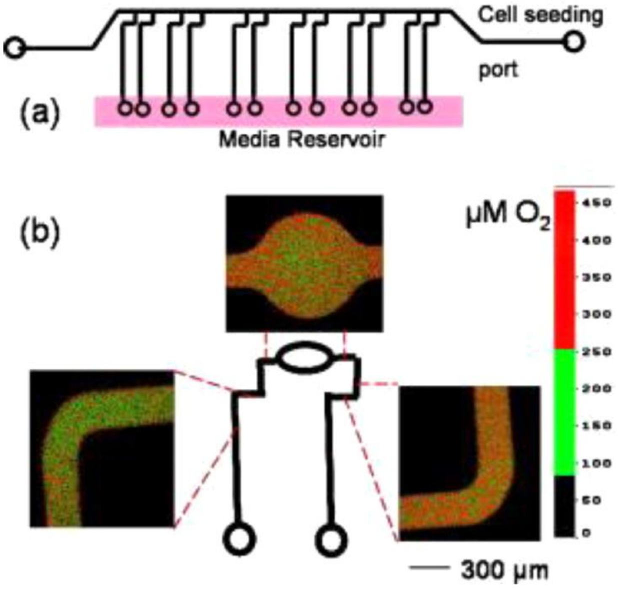

Figure 2.6: oxygen measurements from a closed-loop PDMS bioreactor for continuous cell culture of C2C12 mouse myoblasts. (a) Device schematic. Channel shape was an isosceles trapezoid with a height of 30μm and an upper (lower) PDMS layer of 180 μm(402 μm). Each of the six loops has a right and left valve separating it from the others. (b) Oxygen distribution images at different points of a single loop (binary scale in μM) (Reprinted from [59] with permission from SPIE).

From the same working group, Mehta et al performed oxygen concentration measurement at the upstream and downstream of the cell culture channels at different cell densities and different flow rates [64]. Both fluorescence intensity and lifetime methods were used in this work and the results agreed with a mathematical model that downstream oxygen concentration decreases with increased cell density and decreased flow rate through the microfluidic channels.

Combined with computerized microfluidics and mathematical models, in situ oxygen sensing opens new windows in microphysiologic study with oxygen gradients and low oxygen tensions.

In a following publication [66], Mehta et al. optimized the design of microfluidic bioreactor and the oxygen imaging system was also optimized by replacing former expensive imaging set up by LED light and silicon photodiode, which is more affordable for a broad range of application.

The use of optical oxygen sensors was compatible with glucose sensors in microfluidic systems, which was demonstrated by Lin et al. [75]. Oxygen and glucose sensors were both integrated into a microchannel device culturing mammalian cells. Oxygen sensitive dye $Ru(dpp)_3Cl_2$ dissolved in PDMS was filled into microtrenches within the microfluidic channel wall. A matrix-assisted layer-by-layer (LbL) coating technique [91] was used for encapsulation of the sensors. The detection set up included a fluorescence microscope for intensity imaging, where the single pixel intensity values were only used for obtaining an average signal of each sensor.

Oxygen sensors was studied by Wang et al. [76] for the potential of monitoring and mapping of local oxygen concentration in 3D micro-patterned cell culture systems. Each oxygen sensing bead is composed of a silica core loaded with both an oxygen sensitive $Ru(Ph_2phen_3)Cl_2$ dye and oxygen insensitive Nile blue reference dye, and a poly-dimethylsiloxane (PDMS) shell rendering biocompatibility. $Ru(Ph_2phen_3)Cl_2$ and Nile blue florescence images were recorded focusing on the top and bottom surfaces of micro-wells containing Caco-2, a human colon carcinoma cell.

2.4.3 Measuring single-cell oxygen consumption rates in microfluidic devices

Among the single-cell analysis, oxygen imaging was used for measuring single-cell oxygen consumption rates in microfluidic devices. Molter et al. [92] developed a microwell array device, which is able to diffusionally isolate single cells and enables the quantitative measurement of oxygen consumed by a single cell with fmol/min resolution in a non-invasive and relatively high throughput manner. A frequency-domain lifetime-based oxygen sensing technique was used in earlier publications [93,94]. Laser light was used to excite a phosphorescent sensor based on platinum and the emission signal was collected by a CCD camera using a technique exploiting the phosphorescent properties of the sensors called the optimized rapid lifetime determination (ORLD) technique [95,96].

Similar oxygen imaging in microwell arrays was conducted by Huang et al. [97]. PtOEP sensor layer was incorporated into microwells. A modified commercial digital micromirror device (DMD) projector was used to modulate an LED light source [98], and phase-based phosphorescence lifetime detection was used. This work shows the oxygen consumption rate of cells exhibiting a good linear relationship with diameter of the microwells, ranging from 400 to 1000 μm and containing approximately 480 to 1200 cells within a microwell.

The same data collection method was used in work by Etzkorn et al. [99], in which a method to seed arrays of single cells inside microfabricated fluidic traps was demonstrated. A custom-made dendron-modified Pt-porphyrin oxygen sensor was embedded into a photo-patternable resin to microfabricate sensor ring structures around each single-cell trap site. Then the sensor rings can be optically interrogated to determine the oxygen concentration levels in the vicinity of the cell of interest.

Some optimization was done by Zhu et al by adding plasticizer ethoxylated trimethylolpropane triacrylate (SR454) to the dye-photoresist sensor mixtures to improve the oxygen sensitivity [100] (figure 2.7). In this work, microfabrication process conditions, cell adherence and oxygen sensitivity resulting from patterned structures were studied. It is promising that the developed methods provide a feasible way to miniaturize optical sensors for single cell analysis with precise control of sensor volume and response.

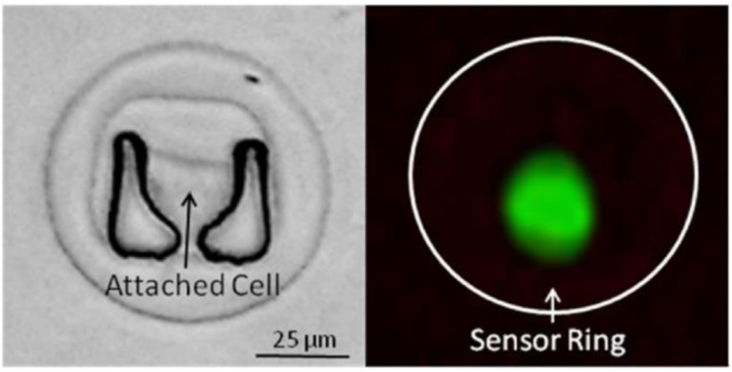

Figure 2.7: (a) Optical microscope image of a trapped, attached cell. (b) Fluorescent image of an attached cell stained with Calcein AM with the sensor ring highlighted with a white circle (Reprinted from [99] with permission from IOP Publishing).

2.4.4 Oxygen imaging for chemical reaction related applications of microfluidic systems

Oxygen imaging is a versatile tool to gain a better understanding of chemical reaction related applications of microfluidic systems. The diffusion coefficient of dissolved oxygen (DO) was measured in a microchannel using UV-LED induced intensity-based fluorescence method by Chen et al. [57]. Mass transfer between oxic and anoxic de-ionized (DI) water was quantitatively visualized in a Y-shaped microchannel. Oxygen-sensitive ruthenium (tris (2,2'-bipyridine) ruthenium (II) chloride hexahydrate) and a 450 nm UV-LED were used for the optical measurement of a DO concentration field.

Intensity oxygen imaging was performed for real-time chemical reaction monitoring in microfluidic environments by Gitlin et al. [71]. PtTFPP/ PS sensor layers are integrated in a PDMS/ glass-based microreactor to monitor real-time chemical reactions. In this work, an approach combining spin coating and abrasion techniques is used for the integration of thin optical sensor layers into microfluidic channels. This novel approach is capable of coating even curved channels homogeneously with microscale lateral resolution. An alternative format of oxygen sensors has been used for performing oxygen measurements inside microfluidic channels by Ungerböck et al [58]. Nanosensor particles stained with the indicator dye $IrCs_2(acac)$ were used to monitor the oxidation reaction of β-D-glucose to hydrogen peroxide and δ-Dgluconolactone by molecular oxygen in the presence of glucose oxidase inside microreactors with Y-shaped microchannels. Oxygen imaging was performed on an epifluorescent microscope equipped with an LED, optical filters and a gateable camera applying rapid lifetime determination (RLD) imaging. These experimental results were compared to mathematical models to assess the required model complexity for an accurate description of reagent transport and reaction inside the microchannels.

Oxygen imaging was used to visualize in pore network microfluidic structures by Grate et al. [70,101]. A Pt(II) meso-tetra(pentafluorophenyl) porphine (PtTFPP) in PDMS film serving as the oxygen sensing layer and a bonding surface, or in a polystyrene film coated with a PDMS layer for bonding are used in this silicon-on-glass device (figures 2.8 and 2.9). Fluorescence lifetime imaging using the frequency-domain and wide field fluorescence intensity imaging, equipped with a CCD camera, was used to generate oxygen gradient images.

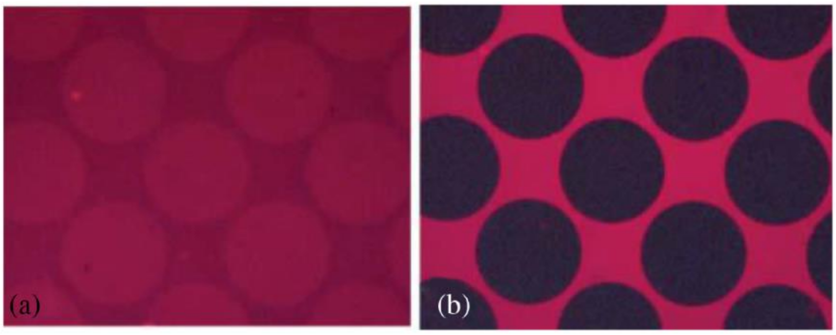

Figure 2.8: Fluorescence intensity images of the PDMS optode film seen from the cover plate side (a) and glass base side (b) of the silicon-onglass micromodel. LED excitation light is provided through the cover plate side to the optode film (Reprinted from [70] with permission from Royal Society of Chemistry).

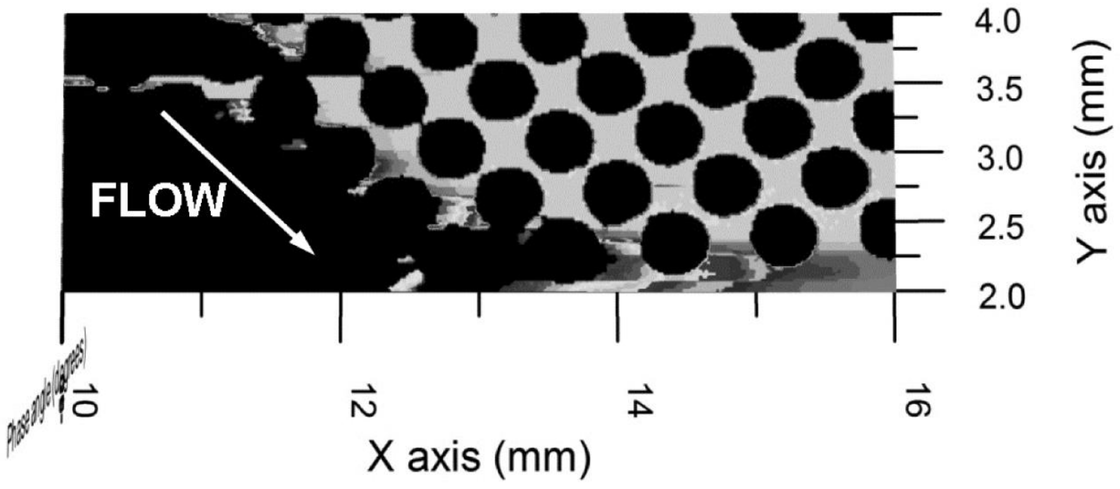

Figure 2.9: Fluorescence lifetime image obtained by a scanning phase technique for an optode in a silicon-on-glass micromodel. The dark region in the lower left corner has high oxygen, and hence little fluorescent intensity, a short lifetime, and a low phase angle, while the regions toward the upper right are anoxic. The gradient was formed in a two-input micromodel. The locations of pillars are apparent as black circles in the anoxic region (Reprinted from [101] with permission from SPIE).

2.5 Conclusion and outlook

Microfluidics or Lab on a chip has become a mature technology and an attractive alternative to existing techniques. However, end-user applications are still rare and the acceptance has to be improved. Research in this field is ongoing and the optical oxygen sensing technique is a perfect fit to the trend of miniaturized analytical tools because of its features including easy miniaturization, high sensitivity, no interaction with analytes, and relatively low cost. Compared with single spot oxygen measurements, oxygen imaging gives us a spatial feedback, which leads to more profound and systematical understanding of diffusion profiles and reactions kinetics in such small scale devices. Herein, spatial resolution of the oxygen concentration can be obtained in the micro- and macro-scale. However, sensor technology (sensor format, read-out system and detection scheme) has to be tailored to the individual applications to achieve best analytical performance. Oxygen imaging in microfluidics has already found exciting applications including visualization of concentration gradients, monitoring of concentrations and chemical reactions and even single cell analysis. In our opinion potential applications for of microfluidic oxygen imaging in the future might be found in:

- Imaging of different chemical parameters in parallel, e.g. oxygen and pH. This can be realized either by using several sensor layers for different parameters or using hybrid sensors, which enable the simultaneous detection of two or more parameters as shown in the macroscopic scale by various authors [102,103].
- Visualization of 3D concentration profiles using confocal microscopy. This will help to elucidate a better understanding of diffusion and reaction kinetics, in particular for complex microfluidic design.
- The combination of intra-cellular imaging and microfluidics has an unrevealed potential. Here, microfluidics offers a distinct control of the cellular environment.
- Imaging of the oxygen concentration in droplet or segmented flow reactors using nano-sized sensor particles which has so far been realized only for single point measurements [33]. Using this kind of principle, the viability of cells and microorganisms can be determined. Highly sensitive detection equipment and high measurement frequency are necessary.
- Monitoring and control for process intensification, e.g. for enzymatic reactors in biocatalytics by imaging the whole microfluidic ensemble with one measurement set-up. This is also feasible for macroscale flow-reactors already used in chemical industry.

2.6 Acknowledgment

Financial support by the European Union FP7 Project BIOINTENSE—Mastering Bioprocess integration and intensification across scales (Grant Agreement Number 312148) and the Marie Curie ITN project EUROMBR—European network for innovative microbioreactor applications in bioprocess development (Grant Agreement Number 608104) is gratefully acknowledged.

3 Oxygen and pH sensing for bioprocess analysis in micro(bio)reactor

Sections of this chapter has been published under the citation:

Viefhues, M., Sun, S., Valikhani, D., Nidetzky, B., Vrouwe, E. X., Mayr, T., & Bolivar, J. M. (2017). Tailor-made resealable micro (bio) reactors providing easy integration of in situ sensors. *Journal of Micromechanics and Microengineering*, 27(6), 065012.

doi: 10.1088/1361-6439/aa6eb9

My contribution for this work is the preparation of the oxygen sensing layer in microfluidic systems, imaging measurement, data process, and writing of the corresponding sections in the manuscript.

3.1 Introduction

Biotechnology has been improving the quality and providing the convenience in our daily life from many perspectives, e.g. the use of enzymes in detergent, the use of microorganism in food industry. Generally, we use biotechnological research for screening of microorganism or biocatalysts with certain feature desired and for optimization of process to achieve high yield of biological products or chemicals and pharmaceuticals[104–106].

During the biotechnological process, it is important to have good monitoring and control over the major physical and chemical parameters which directly or indirectly affect the growing behavior of microorganism or the reaction rate during biocatalytical process. Traditional benchtop scale instruments, for instance stirred tank for microbial applications or biocatalysis, are integrated with a series of sensors, including pH, dissolved oxygen, optical density, CO_2 among others. These sensors allow us to have real-time and continuous monitoring on the physical and chemical parameters, which are used to interpret the consumption of substrate[107], the microbial growth, the yield of products etc. Furthermore, these parameters are usually well controlled for optimization of cell culturing or intensification of biocatalytical reactions.

However, it is challenging to implement sensors in small-scaled bioprocess. As we discussed in previous chapter, optical sensors are the most suitable type of sensors for applications of micro(bio)reactor due to its ease of miniaturization and fast response time mainly. Here we present two examples of micro(bio)reactors with integrated oxygen and pH sensors for process analysis in biocatalysis and cell culturing.

In the first example, we introduce the resealable microfluidic flowcell. Resealable devices provide repeat access to the surface of channels of flowcell. It allows one to modify the channel surface easily, for instance enzyme immobilization. Although most microfluidic systems used in laboratory can be re-opened, they are designed and fabricated for single purpose. In another word, each of the chips are different from each other regarding the dimension, location of connectors and sealing or clamping parts. And some part of the setup cannot be adapted to a different experiment. Furthermore, the material of most microfluidic fabricated is polymer based, which is not compatible with many organic solvents or sterilization process. So most of the established microfluidic systems are limited to the applications those they are designed for and are not versatile for different operating conditions since they all have specific type of connectors or sealing strategies. Our resealable microfluidic flowcell system are highly modularized and standardized. It is versatile for different applications. And the good sealing property is ensured by standard chip holder (Micronit Microtechnologies, The Netherlands) (in figure 3.1). Our resealable flowcell consists of two brosilicate glass slides. The channel structure is defined by the gasket dispensed on one side of the glass slides. Then these two slides form a flowcell by stacking together in the chip holder. The chip holder applies sufficient pressure of the chip to ensure good sealing. And all the connector and tubings are located on the chip holder which are isolated from the flowcells. This type of resealable flowcells maximize the flexibility of modification of the surface, and the versatility of using them for different applications. We perform both single-point oxygen measurement and oxygen imaging to investigate the oxygen diffusion through the gasket and the oxygen consumption during glucose oxidation reaction on the chip.

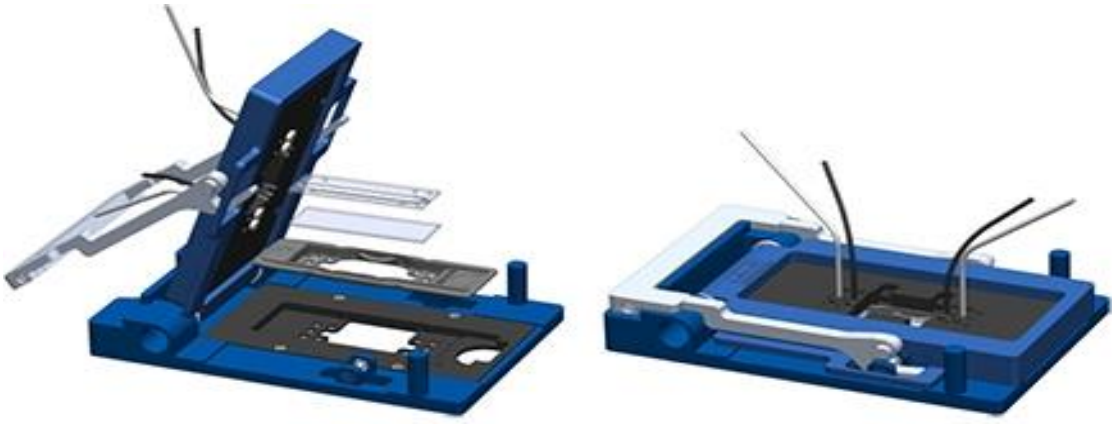

Figure 3.1: Drawing of the chip holder used for the experiments. (Left) exploded view of the resealable flowcell in the open holder with the tubings and optical fibers connected. (Right) drawing of the closed holder.

In the second example, we build a low-cost multiphase micro(bio)reactor for cell culturing. Multiphase (bio)reactor has been well exploded, for example the well-known bubble column reactor. The bubble column reactor has attracted attentions by providing i) enhanced mixing property, ii) an additional gaseous phase, and iii) homogenous distribution of substrate. Different types of multiphase reactors have been invented and studied[108], together with modeling tool to assist design and characterization of them[109]. Not only many efforts have been put into the scale up of these multiphase reactors, but also many studies have been conducted to explore the scale down of them[110–112]. Our collaborators for this project have done great work previously on the design and characterization of the vertical microbubble columns (Figure 3.2) for aerobatic yeast cell cultures[113–115]. They have characterized the oxygen transfer and analyzed reaction kinetics for cultivation in the vertical microbubble columns.

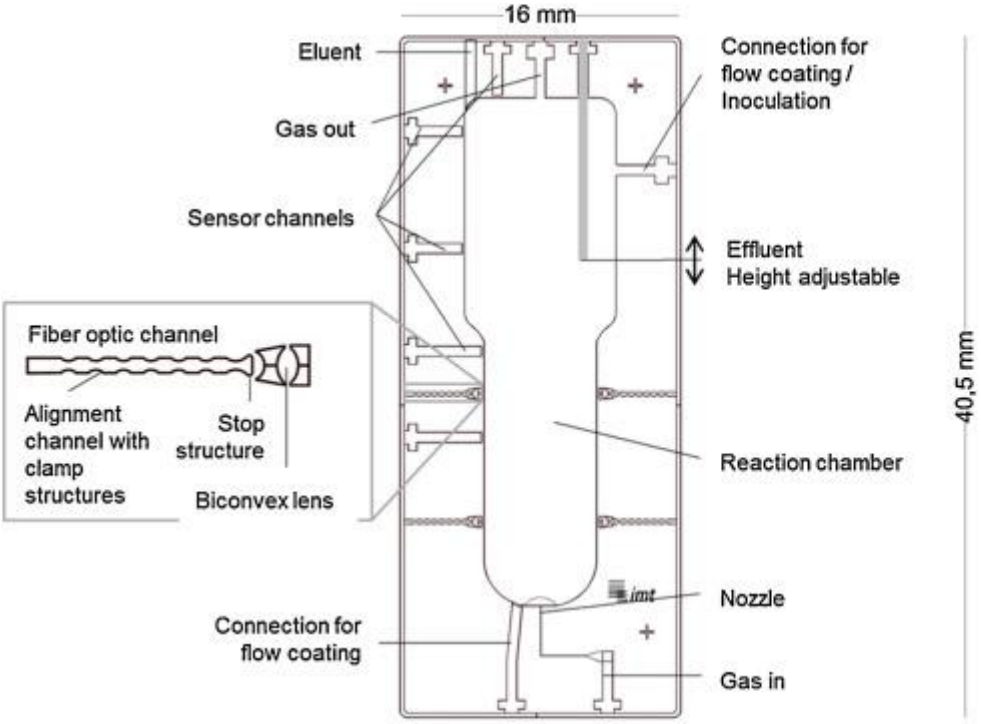
16 mm
Eluent
Gas out
Sensor channels
Fiber optic channel
Alignment channel with clamp structures
Stop structure
Biconvex lens
Connection for flow coating
Connection for flow coating / Inoculation
Effluent Height adjustable
40,5 mm
Reaction chamber
imt
Nozzle
Gas in

Figure 3.2: Multiphase microreactor (mMR), including the reaction chamber, fluidic inlets and outlets, nozzle, adjustable-height effluent tube, fiber optic channels with alignment and clamp structures and biconvex cylindrical lenses for correcting the numerical aperture.

Here in this work, we simplified the fabrication of the reactor, by cutting the cuvette into half and gluing it on a polycarbonate slide, instead of using UV-depth and soft lithography. We integrate glucose, pH, dissolved oxygen, CO_2 sensors, together with optical density measurement into the reactor to obtain real-time and online monitoring of these parameters during cultivation of model microorganism *S. cerevisiae*. To the best of our knowledge, it is the first time that all these parameters (glucose concentration, pH, dissolved oxygen, CO_2, and optical density) are simultaneously monitored in micro(bio)reactor during cultivation. We believe, micro(bio)reactors with highly implemented sensors will play an important role in the evolution of microfluidic systems for bioprocess technology.

3.2 Materials and Methods

3.2.1 Fabrication of resealable flowcells

The resealable flowcells are produced by dispensing the prepolymer of the gasket onto a plain glass slide (Schott, Germany). The gasket is then cured and formed an elastomer by heating. Thus, no masks or soft lithographic steps are needed, which allows quick and easy in-process adaption of the device layout. The dispensing process is shown in figure 3.3. The final gasket height depends on various dispensing settings. For instance, the supply pressure that is applied to the cartridge containing the prepolymer, thus, the higher the applied pressure is the thicker the dispensed line becomes. The diameter of the dispensing tip also has an impact on the gasket height, so with smaller diameters the dispensed line became thinner. Finally, the gasket thickness can be adapted by tuning the writing velocity during dispensing.

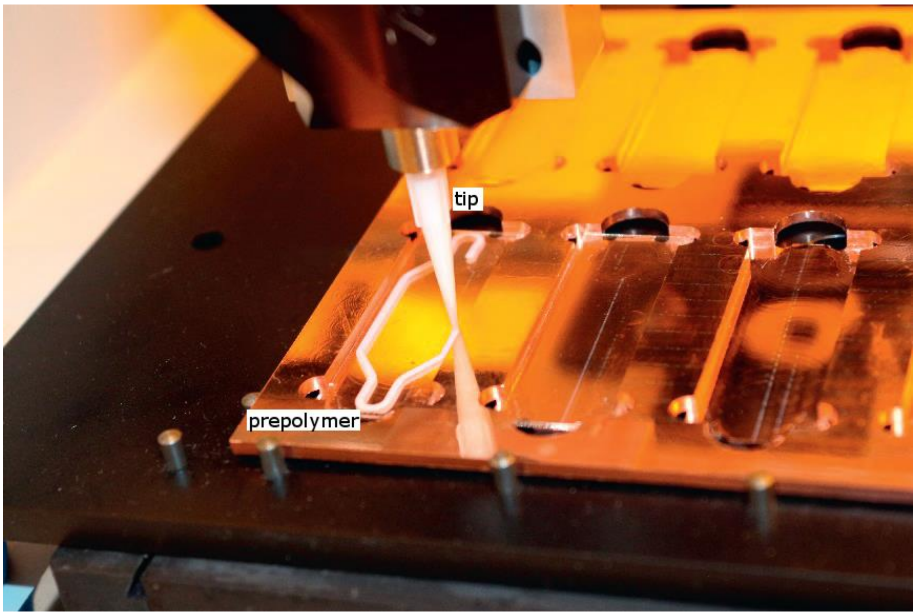

Figure 3.3: Dispensing of prepolymer of gasket onto glass slides. The gasket height depended on the dispensing settings and the respective polymer, e.g. its viscosity. The prepolymer was dispensed to the surface by applying a pressure to the prepolymer cartridge. By controlled movement in x,y,z-direction the flowcell boundary was made.

The gasket is made from two types of material: perfluorinated elastomer (PFE) or medical grade silicone (MED). The prepolymers are cured by heating the material for 10 mins on a hotplate set to 140 °C. Both materials are tested with respect to the chemical resistance against organic solvents and mild acids and bases often used in biocatalytic and enzymatic reactions, i.e. ethanol, isopropanol, acetone, methanol, sodium hydroxide, and hydrochloric acid. Incubation of the flowcells in those chemicals for 60 min does not affect the size, shape or sealing ability of the gaskets.

The outer dimensions of the glass plates are 15 mm×45 mm and the thickness is 1.1 mm for the top part and 0.7 mm for the bottom part. The top glass slide is equipped with through holes at well-defined positions with respect to the gasket structure forming the fluidic inlet and outlet.

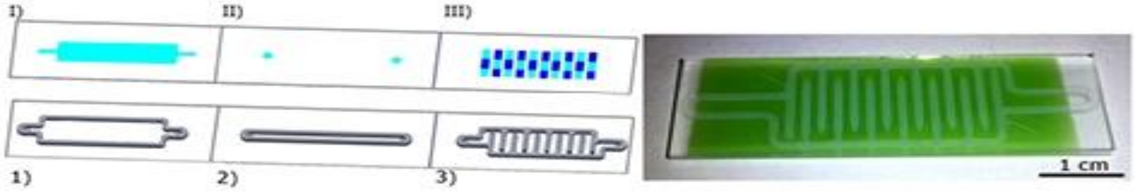

Figure 3.4: (Left) examples of various modules that could be combined to form a tailor-made flowcell. One module from section I–III and one from section 1–3 were selected and stacked. (I) Represents a homogeneous surface modification, e.g. with catalytic biomolecules or sensing layers. (II) Represents a modification for spot measurements. (III) Represents a heterogeneous surface modification, e.g. with two different enzymes. These modifications could also be applied to the fluidic part, i.e. 1–3. (Right) microfluidic chip with meandering channel and oxygen sensing layer (green) as used for the experiments. Please note, this example chip did not contain the access through holes.

The two modular parts are stacked, shown in figure 3.1, and placed into a fluidic connect pro chip holder (Micronit Microtechnologies, The Netherlands), which compresses the stack and results in a liquid tight seal. The 10 mm wide straight and the meandering channel (structures 1 and 3 in figure 3.4) are used in combination with either plain glass slides or slides covered with oxygen sensors. The test setup for determining the leakage pressure of the resealable flowcells, is composed of the flowcell in the holder, a syringe pump with water connected to the flowcell, a pressure sensor connected in series to the flowcell, and a capillary downstream of the resealable flowcell to generate a back-pressure.

3.2.2 Surface activation and enzyme immobilization for flowcells

Before use, the surfaces of the top and bottom part can be functionalized with enzymes or sensing layers, see figure 3.4. Two surface activation protocols are used for the generation of an amino-activated surface on the glass. Glucose oxidase is subsequently immobilized on the modified surfaces by ionic adsorption.

Surface activation

The first step of the surface activation of the top part, containing the gasket, is to clean and to remove the organic residues. The disassembled flowcell is immersed in a mixture of methanol/HCl (1:1) for 30 min, rinsed with deionized water, immersed in sodium hydroxide solution (1 M in water) for 30 min and rinsed with deionized water again. Finally, the flowcell is rinsed with 50 mM potassium phosphate buffer (PPB), pH 7.0. For the N-(2-aminoethyl)-3-aminopropyltriethoxysilane (AAPTES) functionalization the procedure is followed described in previous work[116]. The poly(ethyleneimine) (PEI) surface functionalization is started by incubating a cleaned disassembled flowcell in 5% (v v^{-1}) solution of (3-glycidoxypropyl)trimethoxysilane, pH 8.5, for 16 h at 25 °C as described in [116]. Afterward, the glass slides are rinsed with deionized water and incubated in a solution of 0.1 g ml^{-1} PEI in water, pH 10.0, at room temperature while gently stirred in an end-over-end rotator. Finally, rinsing with ethanol and deionized water remove weakly bound residues. The surface functionalization can also be performed in an assembled flowcell if only specific regions should be modified, e.g. as shown in figure 3.4(I).

Enzyme immobilization

Enzymes are immobilized on non-modified glass surfaces and surfaces with AAPTES or PEI activation. The flowcell part is placed into enzyme immobilization mixture (6 U ml^{-1} GOX in 50 mM PPB, pH 7.0), and incubated for 2 h without agitation at room temperature. After that, the flowcell is assembled and flushed with 50 mM PPB, pH 7.0, at a flow rate of 50 µl min^{-1} using a syringe pump to remove enzymes that are not strongly bound to the surface. The effluent is analyzed by a coupled peroxidase assay.

3.2.3 Determination of enzymatic activity

colorimetric assay

The activity of GOX is analyzed by a coupled peroxidase assay, i.e. colorimetric assay. The colorimetric dye, quinonediimine, is formed via the reaction

$$\mathrm{D-Glucose + H_2O + O_2 \xrightarrow{\text{Glucose Oxidase}} D-gluconic\ acid + H_2O}$$

$$\mathrm{2H_2O_2 + 4-AAP + DMA \xrightarrow{\text{HRP}} Quinonediimine\ dye + 4\ H_2O}$$

where 4-AAP, DMA, and HRP denote 4-aminoantipyrine, N,N-dimethylaniline, and horseradish peroxidase.

The activity of GOX immobilized in the resealable flowcells is analyzed off-line by flushing the assay mixture through the flowcell, containing the immobilized enzyme, and collecting the effluent at the outlet. The collected samples are stored on ice to quench the reaction in case enzyme is eluted. Afterward, the collected volume is analyzed spectrometrically to determine off-line the hydrogen peroxide concentration. The hydrogen peroxide concentration formed is used to calculate the volumetric activity (U ml^{-1}). The volumetric activity is defined as the amount of hydrogen peroxide produced (mM) per applied residence time. Note: one activity unit (U) is the amount of GOX that produces 1 µmol min^{-1} hydrogen peroxide or consumes 1 µmol min^{-1} oxygen at the condition used. This procedure is referred to as continuous coupled peroxidase assay.

Online oxygen monitoring

Another way to determine the enzyme activity, which is indirect, is to monitor the concentration change of substrates or products of the enzymatic reaction. In this work, the activity of immobilized GOX is determined by flushing 100 mM glucose through the flowcell whilst monitoring the oxygen concentration near the inlet and outlet. The amount of oxygen consumed by the enzyme is calculated from the difference between the two signals and the volumetric activity is calculated by the consumed oxygen concentration per applied residence time.

3.2.4 Fabrication of multiphase microreactor

The multiphase microreactor is assembled by half of the cuvette and a polycarbonate microscope slide. The cuvette is made of polystyrene and has a volume of 1.5 ml. Then we glued this half cuvette on the polycarbonate slide. We placed a modified needle at the bottom of the cuvette and uses it as a nozzle for aeration. We built the inlets and outlets by placing needles into the reactor and connect the needles with tubings.

3.2.5 Sensing materials

Oxygen indicator

platinum(II) *meso*-tetra(4-fluorophenyl) tetrabenzoporphyrin (PtTPTBPF) is synthesized in-house according to the literature procedure [85].

pH indicator

pH sensitive aza-BODIPY dye is synthesized in-house according to the literature procedure [117]. More specifically, the indicator used in this work has two chlorine atoms at the pH sensitive phenol group and an electron-withdrawing carbonamide group. Egyptian blue reference particles ($CaCuSi_4O_{10}$) that are produced according to Berke[118]

Polymers

Polystyrene (PS; average molecular weight = 250 000 g/mol) is purchased from Fisher Scientific. Silicone rubber ELASTOIL® E4 is obtained from Wacker. HydroMed D4 is obtained from AdvanSource, MA, USA.

Recipe for sensor “cocktail”

For air spray, PtTPTBPF (0.45 mg), silicone rubber (30 mg) and polystyrene (15 mg) are dissolved in chloroform (1.5 g) to obtain a sensor “cocktail”.

For microdispensing, different combinations of indicators and polymers are used. Also a layer of polymer is introduced on the substrate sometimes to increase adhesion of sensor layer and substrate. A detailed list of all sensor “cocktails” , together with settings of dispensing are on the following page.

Table 3.1: Composition of different sensor cocktails and cocktails for primary layer used for microdispensing.

Cocktail	D4 (mg)	THF (mg)	Toluene (mg)	Isopropanol (mg)	Water (mg)	Indicator (mg)	E.Blue (mg)	Total (mg)
Primary layer - D4	250	2012.5	862.5	N/A	N/A	N/A	N/A	3125
Oxygen layer in D4	250	N/A	N/A	2937.5	979.17	250	N/A	4416.67
pH layer in D4	500	5175	N/A	N/A	575	1.5	250	6501.5

Table 3.2: Settings for different cocktails for microdispensing.

cocktails	Nozzle size (µm)	Pressure (bar)	Z distance (mm)	Tappet lifting (%)	Rising time (s)	Open time (s)	Falling time (s)	Delay time (s)	Number of pulses
Primary layer - D4	200	0.6	1	90	0.3	0	0.09	0.1	1
Oxygen layer in D4	70	0.6	1	65	0.3	0.1	0.1	0.1	3
pH layer in D4	70	0.6	1	65	0.2	0	0.07	0.1	3

3.2.6 Integration of sensor materials into flowcell and micro(bio)reactor

A thin layer of sensor materials can be integrated on one surface of flowcell chip. The air spray machine together with a computerized numerical control (CNC) machine are used to achieve a homogenous surface[119]. For sensor spot in the microreactor, we use microdispenser to directly deposit small amount of sensing material onto the surface of substrate. To ensure sufficient adhesion of sensing material on the substrate, particular polymer/ silicon rubber/ solvent is used according to the material of substrate. For instance, silicone rubber is used for spraying oxygen sensor onto glass surface because it provides good adhesion on the glass surface. If necessary, physical modification of the substrate surface is also used, i.e. roughened surface.

Airspraying

The spraying device consists of an airbrush (EFBE Spritzautomat 1/2L, 0.2 mm nozzle diameter) fixed to an x–y–z table actuated by stepper motors (two-phase-stepper-motor,). The motors are controlled by a Triple Beast Driver (www.benezan-electronics.de), which also drives a fourth axis extension for the airbrush needle valve and a solenoid valve (SMC) for airflow switching. The opening of the airbrush needle valve in combination with the opening time determines the amount of deposited material. The spraying procedure is automated by using G-Code and LinuxCNC. Adequate layer thickness is verified by checking the signal intensity.

Microdispensing

The microdispenser (MDS 3200A, VERMES) is mounted on a three axis Computerized Numerical Control machine (assembled in-house) run by the freeware LinuxCNC. The guiding programs for the dispensing are written in G Code. In order to facilitate the setting of parameters, a LabView program is created that is able to send predetermined settings to the microdispensing device (RS 232) as well as saving the parameters in a txt file. The microdispensing device works with a piezoelectrically guided tappet, that “shoots” fluid drops (in this case polymer solutions) through a nozzle. The cocktail reservoir is closed from the outside and under pressure.

3.2.7 Readout system

According to different formats of the sensor, spot or whole surface, the different readout systems are chosen. For single or multiple sensor spots, the commercial available fluormeter FireStingO2 or Piccolo2 (PyroScience, Germany) is used with lifetime-based measurement. Additionally, for the whole surface format, we are also able to perform time-resolved oxygen imaging.

Single or multiple spots

An optical fiber (tip diameter 1 mm) is directed to the outer surface of the resealable flowcell, see figure 3.5. The optical fibers are led through access holes in the chip holder and connected to FireStingO2 for the spot on-line oxygen monitoring.

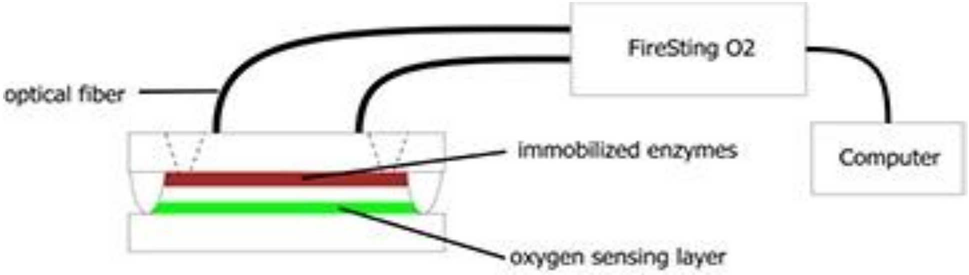

Figure 3.5: Setup for on-line spot oxygen consumption measurement. An oxygen sensitive layer was integrated into the resealable flowcell. Optical fibers were led to the spots of interest through the top of the holder and the signals were monitored in real-time.

For the measurement on the micro(bio)reactor, the fibers connected to FireStingeO2 and Piccolo2 are placed on top of the oxygen and pH sensor spot, respectively, from outside of the wall of the reactor. We use a homemade holder made of polycarbonate to hold and fix the fibers at the same positions during the whole experiments.

Oxygen imaging

Time-resolved oxygen imaging of a large area is performed using a PCO sensiCam (PCO, Kehlheim, Germany) for rapid lifetime determination (RLD) as described by Moser et al [120]. A blue ultra-bright LED with emission maximum at 450 nm (Luxeon Lambert emitter, 5 W, Germany) is applied as the triggered excitation light source for phosphorescence lifetime imaging and combined with a filter set consisting of Schott BG12 and Schott RG 9 (Schott, Germany) as the excitation filter and barrier filter, respectively.

3.2.8 Calibration of the sensors

We calibrate oxygen sensors with the simple two-point calibration. The flowcell, containing the sensing layer, is flushed with air-saturated buffer to determine the phase shift between excitation and emitted light. Afterward, the flowcell is flushed with deoxygenated buffer to again determine the phase shift. For the sensor spot in micro(bio)reactor, we fill the reactor with water, then flush it with air and N_2 alternatively to determine the phase shift at air-saturated and deoxygenated condition.

To calibrate the pH sensor spot, 5 solutions of culturing medium are adjusted to different pH by adding HCl or NaOH, and the pH are measured by pH electrode. Each of these calibration solutions are filled into the reactor, and the phase shift angles are recorded.

3.3 Results and discussion

3.3.1 Characterization of fabrication of resealable flowcells

Fabrication

The advantage of the production using a dispensing robot is that it allows very fast prototyping since the layout of the part could be exported to the instrument directly. Figure 3.6 displays a few examples of layouts that have been fabricated successfully. The ease to adapt the fabrication to different layouts on demand is a powerful asset.

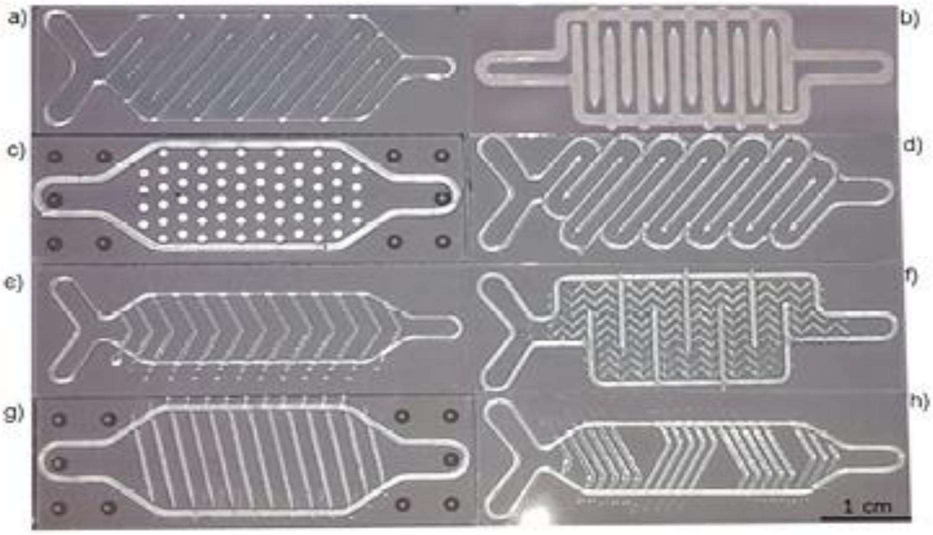

Figure 3.6: Various layouts of structured flowcells that have been successfully fabricated. The structures in (a)–(d) are all of the same height on a single device. In (e)–(f) the structures inside the outline are lower than the height of the outline.

To prove the very good reproducibility of the dispensing production 425 PFE flowcells are made with a single loop, shown in figure 3.4(1), during a period of several months and the gasket height is measured. With the dispensing robot set to dispense a 355 µm high gasket, the resulting mean height is 354 µm with a standard deviation of 6 µm, illustrated in figure 3.7. The total thickness variation for a single flowcell is within instrumental error. The final flowcell height strongly depended on the compression of the gasket. Measurements of 354 µm gaskets revealed a compression of about 10% for usage of the Fluidic Connect Pro holder.

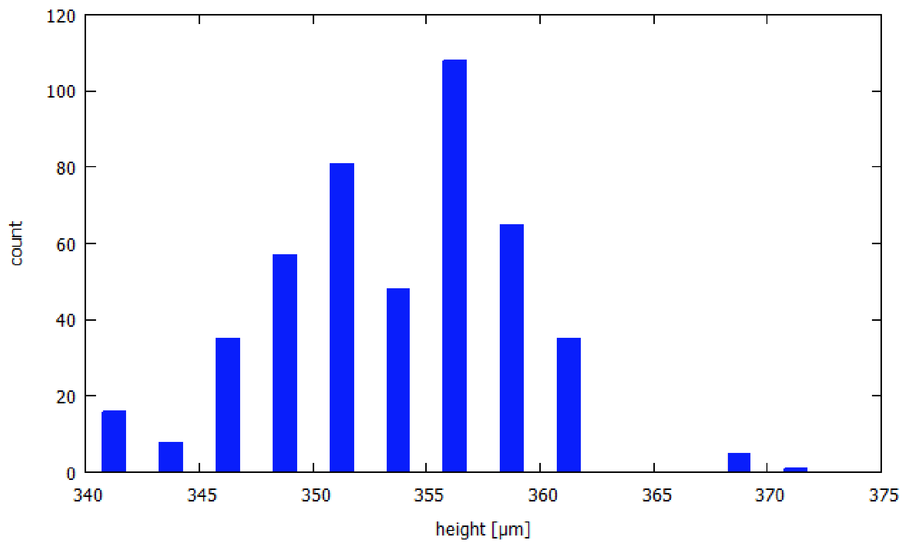

Figure 3.7: Height distribution for one set of dispensing parameters. The mean height is 354 µm with a standard deviation of 6 µm. If a normal distribution is fitted, 95.44 %, which is the definition of 2$\boldsymbol{\sigma}$, of the produced structures have a height in the range of 343 µm and 365 µm.

We achieved a minimum channel width of 450 µm in a meandering channel with a PFE gasket, at a height of 354 µm. However, the minimum height strongly depends on the gasket material and the dispensing tip. So far, the thinnest gasket that led to a sealing flowcell is 70 µm in height.

More complex structures can be made as shown in figure 3.6 in order to for example elongate the path length through the flowcell or serve to assist in mixing or trapping microparticles.

Regarding resealable flowcells with inner structuring one can further distinguish between features that are all of the same height as the outer border, e.g. forming a meandering channel, and features that do not extend to the bottom of the flowcell, e.g. forming ridges. For the latter ones it needs to be taken into account that the elastomeric gasket is compressed when placed inside the holder, thus, the compressed height of the flowcell structure had to be higher than the ridges in order not to block the fluidic path completely.

Sealing performance

A reliable device has to be leak tight for the pressures used during the experiments. For applications with biological samples, e.g. cells, or with enzymes the shear stress and the maximum pressure have to be limited, the latter to about 0.3 bar, to not degrade the samples or destroy weak bindings.

Flowcells are fabricated using two different elastomers to form the gasket consisting of a single closed loop and the maximum operating pressure is determined. During the experiments it is found that the absolute height deviation along a single structure has to be less than 10 µm to get a tightly sealing flowcell. The leakage pressure of 14 flowcells, all made of PFE and with a gasket height of 354 µm, is 0.7 bar +/− 0.1 bar, which is higher than the typical maximum pressures used in biological or enzymatic applications[121–123]. Hence, a reliable and reproducible sealing performance of the resealable flowcells is observed proving the suitability for micro(bio)reactors.

Meandering channels are tested as well and exhibited leakage pressures above 0.45 bar, which is less than for straight flowcells of the same height but still sufficient for many applications. An explanation of the reduced pressure resistance is that slight height variations are observed at the regions where two lines cross each other. This is also in accordance with the observation that the leakage pressure demonstrates poor correlation with the gasket height since the height deviation at the crossing points is almost independent from the total gasket height. In addition, the larger contact area between the gasket and cover resulted in less compression of the gasket. Instead the elastic ferrules connecting the tubing to the flowcell would be compressed more and the glass or support structure in the holder underneath the flowcell could bend.

Flow rates of 8 ml min^{-1} has been tested in a single loop flowcell without observing a leakage for a gasket height of 355 µm. This is in good agreement with calculated flow rates of 7 ml min^{-1} for a hydrodynamic pressure of 0.7 bar and 8 ml min^{-1} for 0.8 bar. Since the devices are aimed at bio or enzymatic applications, no higher flow rates have been tested according to the very high shear stress that would apply to the surfaces of the bio or enzymatic samples. Moreover, the resulting residence time would be too short for oxygen consumption by immobilized enzymes. Nevertheless, with the right combination of gasket material and thickness a maximum operating pressure up to 2.4 bar is achieved.

3.3.2 Transfer of oxygen through the gasket in the flowcells

The oxygen transfer through the gasket is determined in gas phase as well as in liquid phase. For the gas phase the flowcell with a meandering gasket made from MED and straight flowcells made of PFE and MED are tested. We flush the flowcell with nitrogen until no oxygen is measured. Then the nitrogen flow is stopped and the connections are closed. Phosphorescence lifetime images are recorded every minute (demonstrated in figure 3.8(b)) and the oxygen saturation level is plotted versus time (figure 3.8(a)). To measure oxygen resaturation of an aqueous phase, deoxygenated water is flushed through the flowcell. The flowcell is closed and phosphorescence lifetime images are taken, at an interval of one minute.

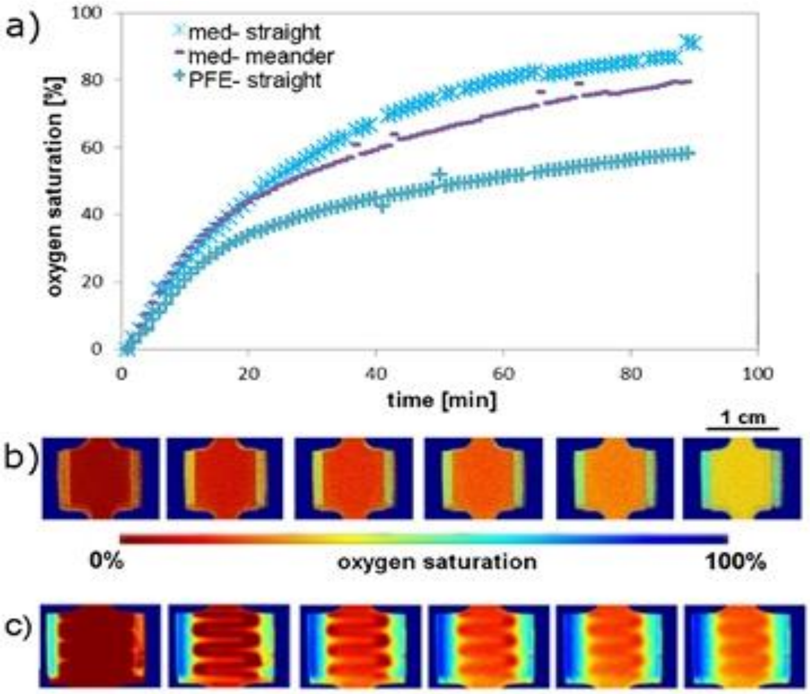

Figure 3.8: Evaluation of the oxygen transfer through the gasket. (a) Oxygen resaturation versus time in the gas phase, two different layouts, straight (figure 3.4(1) and meandering (figure 3.4(3)), and two different materials, PFE and medical silicone. (b) Time-lapse pictures of the first 6 min, 1 per min, of resaturation in the gas phase for a meandering MED channel. A 8 pixel by 8 pixel region of interest was chosen in the center of the fluorescence lifetime image for the numerical evaluation in (a). (c) Time-lapse pictures of the first 6 min, 1 picture per minute, of resaturation in water for a meandering MED channel.

Figure 3.8(a) reveals that the oxygen transfer rate through the gasket was different for all configurations. The medical silicone exhibited a higher oxygen transfer rate than the PFE when comparing structures of the same gasket height. This is assumed due to the following reasons; first, the medical silicone has narrower gasket widths than the PFE reducing the diffusion distance, and second, the medical silicone has a higher gas permeability. A comparison of the straight and meander channels made of MED reveal that the straight channel exhibits a faster re-saturation. One reason for the faster re-saturation of that channel is because the oxygen could diffuse more freely without the ridges.

Regarding the re-oxygenation of water, figure 3.8(c), it is significantly slower than in the gas phase, figure 3.8(b). The MED resealable flowcells reaches 50% oxygen saturation after thirty minutes in the gas phase, whereas in the liquid phase the mean oxygen saturation after thirty minutes is about 20%. In water there is a clear gradient visible from the channel wall to the center of the channel. In contrast, no gradient is visible for the gas phase, figure 3.8(b). This is assumed to be due to the much faster diffusion of oxygen in air versus water.

The results of the permeability test prove two things: first, the gaskets made of PFE and MED are oxygen permeable, but the re-oxygenation is very slow and in many applications the consumption of oxygen would be higher than the replenishing; second, a concentration gradient over the flowcell appears in oxygen consumption applications, which might not be desirable. Additionally, we have shown that integrating oxygen sensing layers inside of the flowcell is a powerful analytical tool. It provides information of the oxygen distribution over the whole chamber, as well as further information on oxygen related enzymatic reactions.

3.3.3 Online oxygen sensing to monitor enzymatic reaction in the flowcells

The resealable flowcells provide the access to the inside of the channels of flowcells, and re-access after the experiment or before the next one. This allows us to modify different functions on different surfaces to achieve to monitor different reactions happening inside of the flowcells. For example, in this case study, we demonstrate the online monitoring of glucose oxidation reaction by oxygen sensing in the flowcell. In order to do that, we modify one side of the flowcell with immobilized enzyme, and the other side of the chip with oxygen sensing layer. Therefore, we are able to monitor the oxygen consumption between the inlet and outlet of the flowcells. Nevertheless, we are also able to provide the information of oxygen distribution inside of the flowcell by oxygen imaging.

In figure 3.9(a) the oxygen concentration is shown for a resealable flowcell with GOX immobilized on a PEI modified surface. The oxygen concentration has been monitored at the inlet and at the outlet of the flowcell. Via the on-line monitoring, a change in the oxygen consumption depending on the flow rate becomes visible. The flow rate, thus, the residence time depending oxygen concentration at the inlet is due to GOX immobilized in the region between the inlet and the position of the optical fiber 5 mm downstream of the inlet.

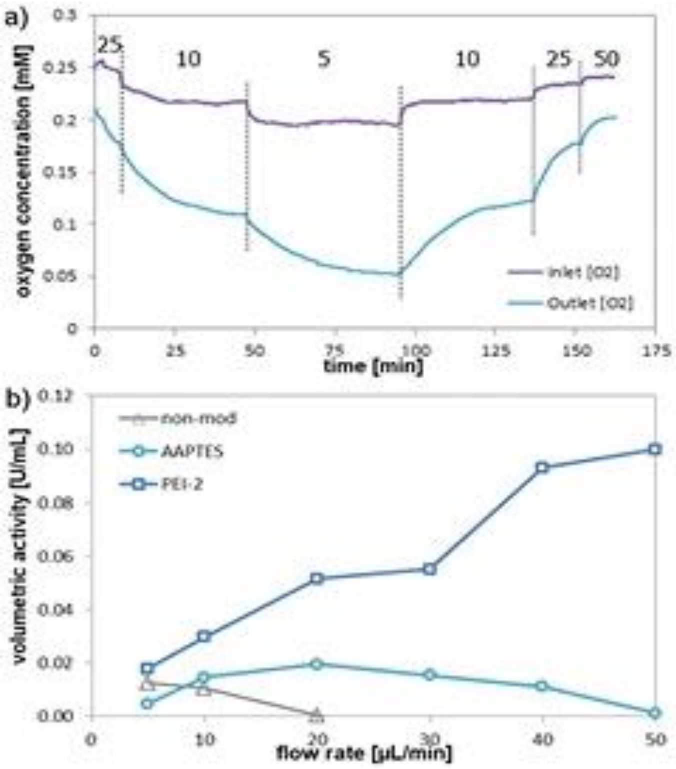

Figure 3.9. On-line monitoring with integrated oxygen sensor. (a) Two point on-line monitoring of oxygen concentration at the inlet and outlet. GOX was bound to a PEI modified surface and a glucose mixture was flushed

at different flow rates through the resealable flowcell, whilst the oxygen consumption was monitored simultaneously. The vertical lines indicate changes of the flow rates in the range of 50 to 5 µl min−1. (b) Volumetric activity of GOX, bound to different modified surfaces, calculated from the oxygen consumption.

The impact of various surface modification on the performance of immobilized enzyme reactor is monitored via on-line measurement exploiting the oxygen consumption as analytical parameter. Figure 3.9(b) shows the volumetric activity of different immobilized enzyme flowcells. The volumetric activity is very low for the non-mofidied flowcell, and it gets lost when the flow rate increases. The volumetric activity is higher for the AAPTES-modified flowcell one but it also decreases when the flow rate increases. It seems that slightly elution of enzyme under continuous flow conditions causes the reduction of enzyme activity.

A quantitative comparison reveales that the volumetric activity of AAPTS- and non-modified flowcells are higher for the off-line method than for the on-line monitoring. It is plausible that, due to analytical limitations of the colorimetric assay, the enzyme elution is not observable with the off-line method.

Regarding the PEI-modified flowcell, which provides higher binding capacities to load enzymes, the volumetric activity is higher and increased with the flow rate. The dependence between apparent volumetric activity and residence time have been attributed to co-substrate (oxygen) limitation in oxidase immobilized microreactors[124] but it can be only probed via direct oxygen measurements. Measurement of the net oxygen consumption indicates that at long enough residence times, the oxygen concentration is depleted to a level of first-order dependency between reaction rate and concentration[124,125]. Additionally, imaging of the oxygen concentration through the microchannel could be performed to support this continuous depletion.

As summary, the comparison between the two analytical methods demonstrate that the on-line monitoring provides a better insight view because the on-line monitoring is not affected by eluted enzymes since the product concentration is directly measured in the flowcell. Therefore, the product concentration in the flowcell is determined without the overestimation of the enzyme activity due to additional products by eluted enzymes. This highlights once again the advantage of the modular character of the resealable flowcell, enabling various modification scenarios and integration of *in situ* sensors.

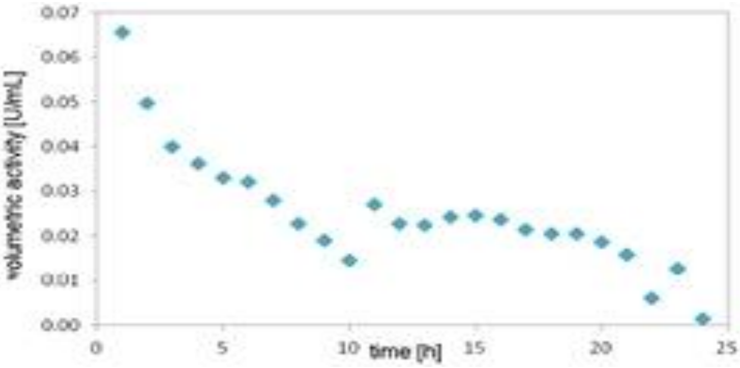

Figure 3.10. Enzyme volumetric activity monitored during a 24 h period. The flowcell surface was activated with PEI for stable binding during the test with a flow rate of 20 µl min^{-1}.

Addtionally, an on-line monitoring experiment is carried out to study the stability of the enzyme during constant perfusion at 20 µl min^{-1}, to prevent oxygen limitation, over a period of 24 h. The results of the long-term measurement are depicted in figure 3.10. The volumetric activity at the beginning of the experiment is comparable to the previous experiments. The subsequent decrease of enzymatic activity could have two causes. First, the enzyme might desorb from the surface. Secondly, the enzymes might have degraded, for example due to the presence of hydrogen peroxide[126]. That effect could be reduced through the addition of catalase to the mixture. These results prove that the on-line monitoring via spot measurements is very effective in detecting slow changes over time as well as events.

In order to investigate the cause of the decay in enzymatic activity during long-term measurements, imaging analysis could be exploited, e.g. labeling the enzymes with a dye and performing surface scanning microscopy to check whether the enzymes detached from the surface. Beyond that in next studies the combined effect of the oxygen concentration and the pH of the substrate solution on the enzymatic conversion could be implemented in the presented devices.

An inspection of the oxygen sensing layer after the long-term measurement reveales that the experiment had no impact on the sensing layer. Furthermore, no changes are observed for the resealable flowcell, thus both, the sensing layer and the resealable flowcell could be reused, the latter is already proven to resist treatment with organic solvents, hydrochloric acid, or sodium hydroxide to remove organic residues if needed.

3.3.4 Oxygen imaging in the flowcells

For oxidase immobilized reactors, there is the hypothesis that, at long enough residence time, oxygen will limit and the calculate volumetric activity will be flow-dependent (the shorter the residence time, the higher the volumetric activity) [19]. On-line sensing provides an insight on that, whereas imaging the oxygen concentration along the whole fluidic path allows to overcome the restriction of using outlet-inlet data. Thus, in addition to the spot measurements near inlet and outlet also the oxygen concentration distribution is imaged.

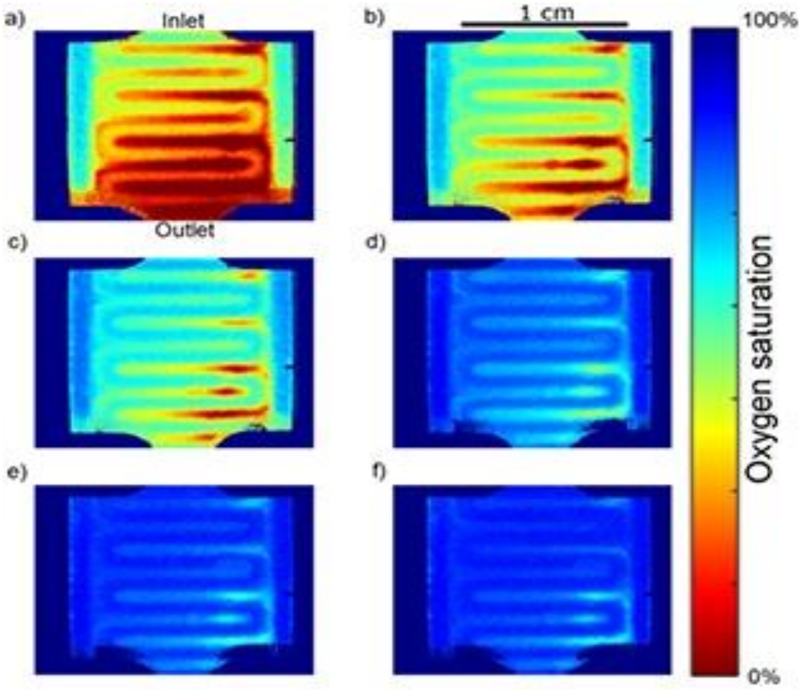

Figure 3.11. Oxygen consumption monitoring of GOX immobilized on a PEI functionalized surface. Images were taken for various flow rates after equilibrium was reached, checked with two point monitoring. Flow rates: (a) 5 µl min^{-1}, (b) 10 µl min^{-1}, (c) 20 µl min^{-1}, (d) 30 µl min^{-1}, (e) 40 µl min^{-1}, and (f) 50 µl min^{-1}.

PEI modification is used because that led to the best binding stability of enzyme in the previous experiments. Pictures of the phosphorescence lifetime are taken, see figure 3.11. The oxygen concentration distribution is determined for six different flow rates between 5 µl min^{-1} and 50 µl min^{-1}. It is obvious that the oxygen concentration at the outlet drops significantly for low flow rates of 5 and 10 µl min^{-1}. This is due to the long residence time and led to an underestimated volumetric activity due to oxygen limitations. Thus, these results further explain and confirm the results that have been gained by the coupled assay and the on-line monitoring. For flow rates of 20 µl min^{-1}–50 µl min^{-1} the gradient of oxygen concentration along the fluidic path is significantly smaller compared to those with flow rates of 5 µl min^{-1} and 10 µl min^{-1}. Thus, it is assumed that for those flow rates no oxygen limitation would lead to underestimated volumetric activities, while at the same time an oxygen depletion by the immobilized enzymes could be observed.

3.3.5 Characterization of the multiphase micro(bio)reactor

We flush the air into the reactor through the nozzle place on the bottom of the reactor. The air goes through the nozzle and forms tiny bubbles in the reactor. The air is preheated to 30 °C by thermobath to prevent heat transfer in reactor during the incubation. The volumetric oxygen mass transfer coefficient (kLa) depends on the air pressure of the nozzle. The kLa ranges between 400 – 800 h^{-1} for the volume of sample of 500 µl. The superficial gas velocity of bubbles is $8.4 * 10^{-3}$ m/s (at 0.174 bar air pressure) determining by an U-tube gas flow meter.

3.3.6 Monitor bioprocess in micro(bio)reactor during cultivation

We cultivate *S.cerevisiae* in the micro(bio)reactor. Initial OD, which medium. From the nozzle on the bottom of the reactor, we bubble moisturized air into the reactor to enhance the aeration during the cultivation. With highly implemented sensor system, we are able to monitor the change of 1) glucose concentration, 2) dissolved oxygen concentration, 3) pH, and 4) optical density over the cultivation.

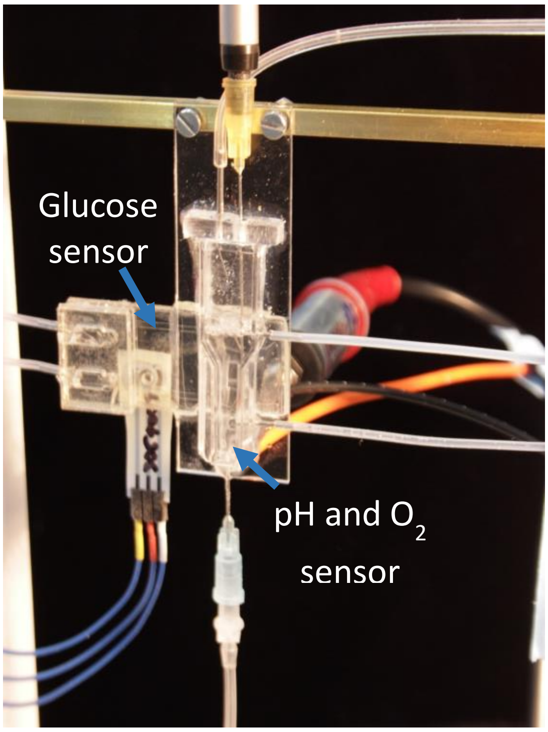

Figure 3.12: Setup of micro(bio)reactor with integrated sensors.

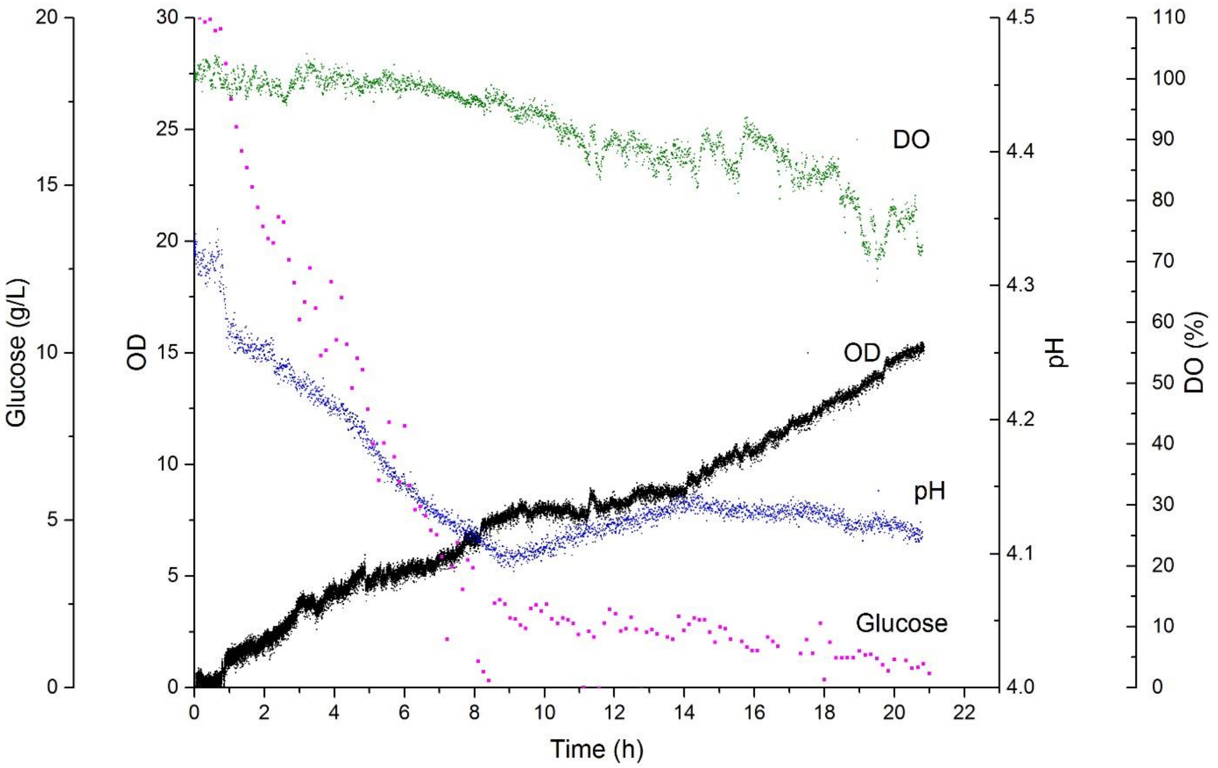

Figure 3.13: Change of glucose concentration, optical density, pH, and dissolved oxygen in micro(bio)reactor during the cultivation of *S. cerevisiae*.

From the figure 3.13 above, we observe the growth of the biomass over the time. And the diauxic behavior [127] is also observed, the growing "step" at hour 8. From the metabolic point of view, the explanation is the switch of the substrate. In our case, *S. cerevisiae* utilizes glucose as carbon source and produces acids and ethanol. Once glucose is depleted (or at low concentration), the cells switch to consume the acids and ethanol accumulated before. This hypothesis is perfectly confirmed by the monitoring of the change of glucose concentration and pH. The glucose concentration in the medium is 20 g/L. After 8 hours of cultivation, the concentration of glucose drops to below 2.5 g/L, which shows that no glucose is available for the cells afterwards. At the hour 8, when the glucose has been depleted, the growing slows down shown by OD measurement. Furthermore, hour 8 is also the turning point where pH stops decreasing. During the first 8 hours of cultivation, *S. cerevisiae* produces acids and accumulates them in the medium, which causes the decrease of the pH. After the hour 8, since the glucose is depleted, the cells start to utilize the acids produced early for further growing. This explains why we observe this slight pH increase after 8 hours of cultivation.

The dissolved oxygen level remains high (above 70% air-saturation) during the whole time. This confirms that by bubbling air continuously into the reactor ensure sufficient aeration for the cultivation. In another word, no oxygen limitation is reached in our reactor. We believe due to the small volume of cultivation, bubbling is a powerful and simple way to achieve sufficient oxygen supply for cultivation.

It is also worth to mention that due to the high biomass concentration achieved, the correlation between transmitted light and OD is not linear anymore, and we do not see the characteristically exponential growth phase.

3.4 Conclusions

Process control is important for biotechnology applications. It becomes challenging when it comes to small-scaled reactor, which means limited space and limited sample volume. We present here the sensing strategy of integration of optical sensors into micro(bio)reactor for bioprocess analysis. We show the single point oxygen measurement and oxygen imaging on flowcell chip with immobilized enzyme. We also monitor several parameters, pH, dissolved oxygen, glucose concentration, and optical density simultaneously and online of the cultivation of *S. cerevisiae* in micro bubble reactor.

The resealabe flowcell presented here is highly modularized and versatile. We can structure different channel layout on the chip. It gives different flow functions, for example enhanced mixing property. Since the flowcell can be easily opened and assembled, we can combine top and bottom layer of the chips with different functions. In the example we have shown here, we have enzyme immobilized on chip, and oxygen sensor deposited on the other chip. By putting these two chips together, we can perform enzymatic reaction in the flowcell and monitor the oxygen distribution over the over surface. Different enzymes can be immobilized by different ways on the chip. And different sensors can be integrated on the chip to give the information of certain parameter that relevant. This concept provides a tool box for easy and quick screening for biocatalysis study.

The bubble micro(bio)reactor has shown great aeration during cultivation. We optimize the design from previous work and build the low-cost version of the reactor. For the first, we implement multiple online sensing systems in such a small reactor to obtain most important parameters during cultivation. From the profile of dissolved oxygen, pH, glucose concentration and optical density, we observe the typical diauxic growth behavior of *S. cerevisiae*. These parameters on one hand provide valuable information of cell culturing, on the other hand give profound information of the miniaturized (bio)reactors compared with (bio)reactors in the size used in conventional study. With the better understanding of the microorganism and the reaction in the micro(bio)reactor and the reactor itself, we believe biotechnology in microscale is very promising.

3.5 Acknowledgement

The research leading to these results has received funding from the People Program (Marie Curie Actions) of the European Union's Seventh Framework Program under REA grant agreement no 608104.

4 Lifetime of phosphorescence from nanoparticles yields accurate measurement of concentration of oxygen in microdroplets and allows to monitor the metabolism of bacteria

Chapter 4 has been published in full under the citation:

Horka, M.*, Sun, S.*, Ruszczak, A., Garstecki, P., & Mayr, T. (2016). Lifetime of Phosphorescence from Nanoparticles Yields Accurate Measurement of Concentration of Oxygen in Microdroplets, Allowing One To Monitor the Metabolism of Bacteria. *Analytical Chemistry*, 88(24), 12006-12012.

doi: 10.1021/acs.analchem.6b03758

*M.H. and S.S. contributed equally.

Abstract

A method to monitor the level of oxygen in microdroplets is presented. Optical sensor nanoparticles are dispersed in the aqueous phase of the microfluidic droplets for culturing bacteria. The oxygen sensor nanoparticles consist of phosphorescent indicator dye embedded in poly(styrene-*block*-vinylpyrrolidone) nanobeads. The nanoparticles are excitable by red light and emit in the near-infrared spectra region which minimizes background fluorescence from biological matter. The biocompatibility of the nanoparticles was proven. Nanoparticles sensors were read out by adapted miniaturized oxygen meters. The instruments can be easily integrated into the microfluidic system by placing it next to the tubing and measuring through the tubing wall. The phosphorescence lifetime-based measurement circumvents the drawbacks of intensity-based measurements and enables the determination of the absolute oxygen

concentration in individual moving droplets. The technique can also be used for monitoring the growth of bacteria in microdroplets. We demonstrate simultaneous measurement of concentration of oxygen and optical density (OD) from micro cultures of *E. coli* and *M. smegmatis*.

4.1 Introduction

Droplet microfluidic technologies allow to encapsulate, isolate and culture small groups of microorganisms[25,26]. The limited (nl to μl) volume of the reactor provides for the so called "stochastic confinement"[128] and effective concentration to measurable levels of metabolic products and secreted molecules. Compared with bulk cultures, culturing bacteria in droplet microfluidic systems is cost-effective as it uses small quantities of reagents, and can be used in high-throughput studies[129,130] because it is straightforward to generate and handle multiple droplet bioreactors. These features make up for an attractive platform for research in microbiology, including analysis of bacterial growth and adaptation in microdroplet chemostats[131], analyzing and sorting bacterial phenotypic diversity and high-throughput directed evolution of bacteria[23,132].

Both diagnostic procedures and research protocols often require the information about the growth rate of microbes. The most commonly used detection methods to characterize and monitor bacterial growth in microfluidic systems are i) detection of fluorescence, *i.e.* fluorescent proteins synthesized by bacteria[133–136] or fluorescent markers[30–32] ii) measurement of changes in optical density of the suspension caused by growth of bacteria[131,137,138], iii) monitoring bacterial enzymatic activity[139–142] or production rate of metabolic products, *i.e.* ethanol[143,144]. It is highly desirable to monitor the concentration of analytes which directly influence bacterial growth, for example concentration of oxygen. Oxygen uptake rate is one of the fundamental physiological parameters of the culture conditions[145]. A recent tutorial review summarized both electrochemical and optical approaches for implementing analysis on concentration of oxygen in microfluidic cell and tissue culture systems[146].

Monitoring oxygen concentration is of vital importance for growth and metabolism of aerobic bacteria in droplet bioreactor, since oxygen concentration could be an important constraint in the limited volume of droplets[147]. An accurate and reliable method for oxygen measurement in droplets could provide an important tool for the use of droplet microfluidic technologies in microbiology. Measurement of concentration of oxygen in droplets, however, presents several challenges: 1) requirement for high sensitivity of sensor and adequate intensity of signal due to the typically small (nl - µl) volume of droplets; 2) preference for miniaturized sensors and detectors that could be easily integrated with a microfluidic chip or a segment of tubing; 3) necessity for the sensor to be biocompatible and inert without any significant influence on the biological processes undergoing in droplets. Within the range of known methods of measurement of concentration of oxygen[51], optical oxygen sensing strategies seem to best comply with the requirements listed above. Optical sensors are highly sensitive with short response time, inert, compatible with miniature volumes and cost-effective.

While there are multiple examples of using optical oxygen sensor in single phase microfluidic systems for monitoring enzymatic reactions[35] and cell culturing conditions[59,60,64,148], and investigation of oxygen transfer[57,58], the reports on measuring oxygen content in droplets are few. The most commonly used format of sensors for microfluidic applications is compatible with the planar structure of the chips: for example, by gluing sensor foil or spraying sensor layer into the microfluidic channels. Droplet microfluidic applications require a different approach - the sensitive element must be in direct contact with the droplet (in biological applications – aqueous phase). Therefore, directly dissolving indicator or dispersing sensor nanoparticles are preferred formats. Abbyad *et al.* introduced oxygen sensitive dye into the aqueous phase[149].

They measured concentration of oxygen in droplets and showed that droplets can be oxygenated or deoxygenated by being carried by air-saturated or oxygen-free oil, respectively. Still, oxygen concentration was not monitored when red blood cells were introduced into the drops. Cao *et al.*[33] stained oxygen sensitive dye into polystyrene nanobeads and mixed oxygen-sensitive nanobeads with cell suspension. The authors used measurement of intensity of fluorescence to monitor concentration of oxygen in droplets during bacterial cultivation. And they retrieved only the relative change of oxygen concentration (i.e. fraction of oxygen consumed during incubation). The accuracy and precision of an intensity-based measurement suffers from uneven distribution of the dye in droplets or the geometry of the droplets, photo bleaching, and variations of the instrument. In a similar approach, Mahler et al.[147] dispersed oxygen-sensitive nanoparticles in cell culturing media and used lifetime-based measurement. They monitored only concentration of oxygen in a group of pl volume droplets trapped in a 3D printed micro-incubator.

Here we present a solution that offers on-line, real-time, and accurate measurement of concentration of oxygen in individual droplets in a microfluidic culturing system. We use optical oxygen sensitive nanoparticles in combination with phosphorescence lifetime-based measurement enabling the determination of absolute concentration of oxygen. We compare optical density (OD) and oxygen level in droplets during cultivation of *E. coli* and *M. smegmatis*. We also investigate oxygen transfer rate (OTR) from carrier oil phase to droplets and through tubing wall of microfluidic cell culturing system.

4.2 RESULTS AND DISCUSSION

4.2.1 Tubing-based microfluidic cell culturing device

We fabricated the microfluidic device using Teflon Fluorinated Ethylene Propylene (FEP) tubing (ID = 0.8 mm, OD = 1.6 mm) and customized fluidic connectors (Figure 4.1c and Figure 4.12). These connectors provide convenient flexibility to the tubing-based microfluidic system. Together with automation system, we are able to use tubings and connectors to build various functional modules, *e.g.* a module for fusion of two droplets with different contents, a module for splitting droplets into two parts and a module for sorting droplets. In this work, the microfluidic cell culturing system consists of two parts: a module for generation of droplets and another one for incubation of the colonies (Figure 4.1a). The module for generation of droplets comprises a T-junction. A three-way Teflon connector allows us to introduce the aqueous phase into the hydraulic line that carries the continuous liquid (oil). We generate aqueous droplets of desired volume by controlling the interval over which the aqueous phase is injected into the T-junction module. The average volume of droplets in this work is 4 µl. And we fix the rate of flow of the continuous liquid to 20 ml/h. Once formed, the droplets flow into the module for incubation. In this module, we place fibers on opposite sides of tubing for measurement of OD, and attach the Piccolo2 detector to the wall of the tubing for measurement of concentration of oxygen. We measure and record information of OD and concentration of oxygen in each droplet when they pass through the detection unit (Figure 4.1b). We control the flow of droplets through the system with a set of external valves connected to pressurized reservoirs of oil and to outlets maintained at ambient (atmospheric) pressure. We use a custom written Lab View script to control all valves. This highly automated system enables precise handling of droplets for bacterial culturing[131,150].

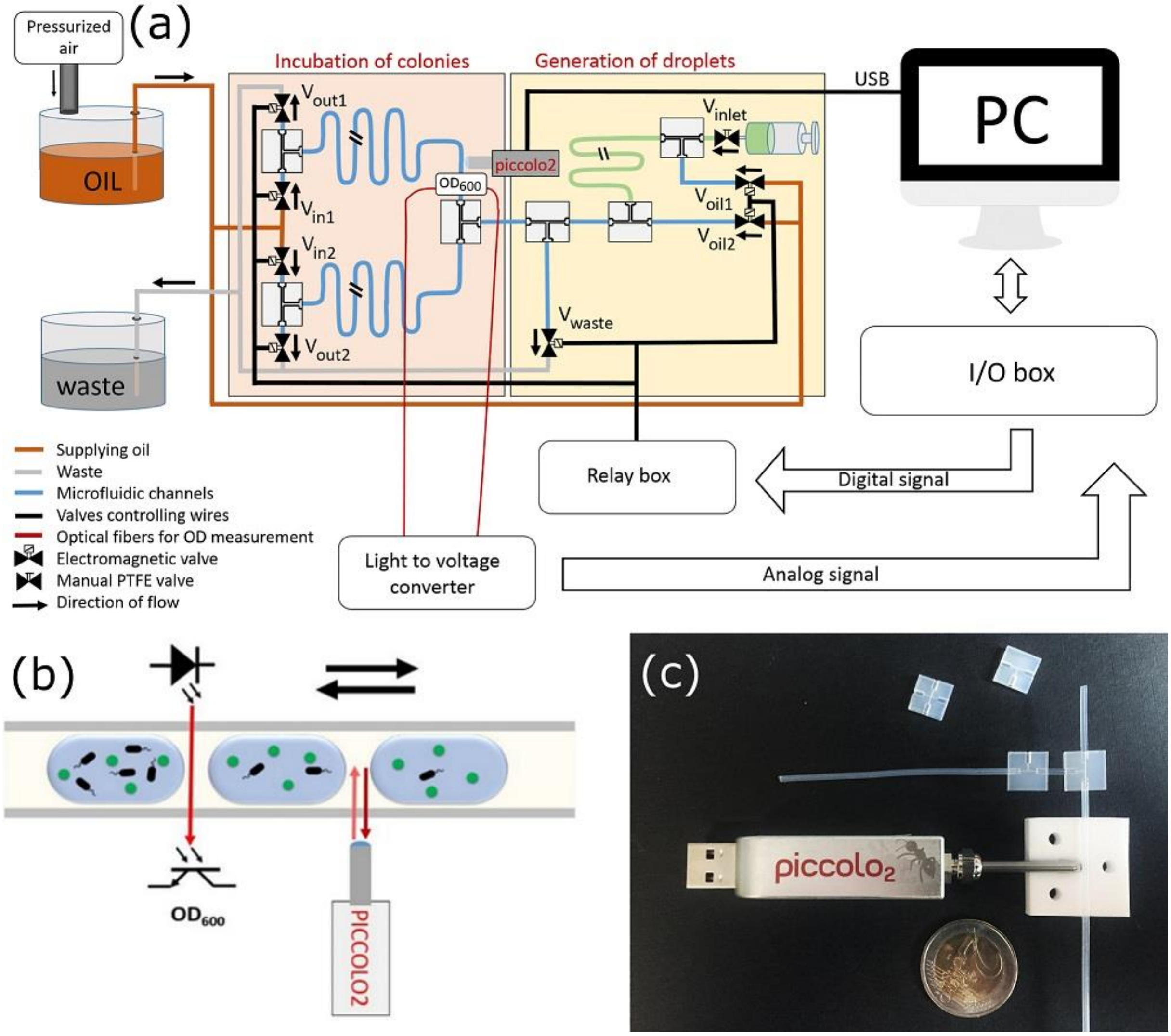
(a)
Pressurized air
OIL
waste
Incubation of colonies
Generation of droplets
V_{out1}
V_{in1}
V_{in2}
V_{out2}
piccolo2
OD600
V_{inlet}
V_{oil1}
V_{oil2}
V_{waste}
USB
PC
I/O box
Relay box
Digital signal
Analog signal
Light to voltage converter
Supplying oil
Waste
Microfluidic channels
Valves controlling wires
Optical fibers for OD measurement
Electromagnetic valve
Manual PTFE valve
Direction of flow
(b)
OD600
PICCOLO2
(c)
piccolo2

Figure 4.1: (a) Scheme of microfluidic cell culturing system including two parts: generation of droplets and incubation of colonies; (b) zoom-in of detection unit in the incubation part including measurements for Optical Density (OD) and concentration of oxygen in droplets; (c) picture of tubings connected by customized fluidic connectors and with Piccolo2 placed next to it and fixed by a homemade holder (only bottom part is shown).

4.2.2 Compatibility of oxygen sensor nanoparticles and microfluidic cell culturing system

Oxygen sensor nanoparticles are made by entrapping oxygen indicator dye Platinum(II) *meso*-tetra(4-fluorophenyl)tetrabenzoporphyrin (PtTPTBPF) in poly(styrene-block-vinylpyrrolidone) (PSPVP) nanobeads. The indicator PtTPTBPF is excited by red light and emits in near-infrared wavelengths (above 700 nm). This range of frequencies is particularly compatible with measurements on biological systems because it minimizes background fluorescence and has little interference with cells151. Additionally, other optical channels, i.e. channels for autofluorescence or fluorescent protein/ markers, are still available for simultaneous measurements. The core-shell structure of the PSPVP nanobeads makes it possible to disperse the beads in aqueous phase and to immobilize oxygen indicator in the lipophilic core formed by nonpolar polystyrene blocks152,153. Furthermore, using nanoparticles with sensing dye entrapped shows the great advantages over directly dissolving indicator dye in droplets. The nanoparticle structure shields the sensor molecules and prevents any interferences from the sample i.e. proteins. Nevertheless, many of the indicators possess extreme low solubility in aqueous solutions. Also sensor nanoparticles exhibit short response time, no dye leaching, and long storage period154, which are ideal for microfluidic applications. The nanoparticles have an average diameter of 180 ± 5 nm, together with TEM images reported by Ehgartner et al.35.The spectral properties of this oxygen sensor nanoparticles are compatible with the miniaturized, commercially available, phosphorescence lifetime-based read-out instrument Piccolo2 (Figure 4.1c) equipped with a focusing lens, as reported recently119. The Piccolo2 can measure through the wall of a tubing (or other transparent materials e.g. polycarbonate, polystyrene, PDMS, and glass) at any location of the microfluidic system. By using lifetime-based measurement, instead of intensity-based measurements, we are able to accurately characterize oxygen concentration in microdroplets. The lifetime is an intrinsic property of oxygen sensor nanoparticles and is not affected by instrument variations, sample turbidity, or ambient environment. Details of optical oxygen sensing principle and full calibration curves of the oxygen sensor nanoparticles at room temperature (20 °C) and incubation temperature (37 °C) are available in the supporting information.

To check that the oxygen sensor nanoparticles are not affected by the procedures used to treat the growth media for bacteria, we compared the calibration curves of the sensor nanoparticles before and after five cycles of autoclave procedure (121 °C for 15 minutes). We have not seen any significant change in the sensitivity of the nanoparticles to concentration of oxygen (Figure 4.6). Besides, the sensor nanoparticles show effects on the growth of neither Gram positive (*S.epidermidis*) nor Gram negative (*E.coli*) strains. We check the survival rate of both *S.epidermidis* and *E.coli* with different dilution factors of sensor nanoparticles suspension (Figure 4.7a). We also obtain same growth curves of *E. coli* with and without oxygen sensor nanoparticles present in LB media (Figure 4.7b).

4.2.3 On-line real-time measurements of concentration of oxygen in microdroplets

First of all, we demonstrate that the oxygen sensor nanoparticles yield an accurate and reliable measurement of concentration of oxygen in the following settings: i) in a bulk solution, ii) in continuous flow in a tubing and iii) in microdroplets flowing in a tubing (see Table 1). We prepared both oxygen free and air saturated aqueous solutions with suspended oxygen sensor nanoparticles. We then measured the phase shift angle and calculated lifetime for oxygen free condition (τ_0) and lifetime for air saturated condition (τ). The ratio of τ_0 and τ defines the calibration curve for a given batch of sensor nanoparticles. The difference of this ratio is negligible between the measurements from continuous (single phase) flow and from microdroplets in the tubing, which shows the feasibility of using oxygen sensor nanoparticles for measurements of concentration of oxygen inside microdroplets. The resolution of this oxygen sensor nanoparticles for low oxygen range (50 µM) and high oxygen range (air-saturation) are 0.07 µM and 0.12 µM, respectively (1 atm, 20 °C).

Table 4.1: Comparison of signal (phase shift) recorded from oxygen sensor nanoparticles and calculated lifetime (τ) from the same solutions at oxygen free and air saturated conditions of settings i) in a bulk solution, ii) in continuous flow in a tubing, and iii) in microdroplets flowing in a tubing.

Dimensions	oxygen free		air saturated		τ_0/τ
	phase shift / °	τ_0 / µs	phase shift / °	τ / µs	
bulk	55.68±0.01	58.29±0.02	23.77±0.01	17.52±0.01	3.33
continuous flow	55.18±0.07	57.21±0.15	23.88±0.02	17.62±0.02	3.25
microdroplets	55.15±0.03	57.15±0.06	23.87±0.04	17.61±0.03	3.25

We carry out the measurement of concentration of oxygen in microdroplets at a frequency of 10 Hz (the sampling frequency is limited by electronics of Piccolo2). When each droplet passes through detection unit, we are able to acquire 7 – 8 measurements on each of the droplets. Our acquisition system records both the phase shift angle and the intensity of phosphorescence from the nanoparticles (Figure 4.2a).

The quality of the signal recorded from the droplet depends on the particular part of the drop that is illuminated. The droplets are confined by the walls of the tubing and in the first approximation they acquire the shape of cylinders truncated with hemi-spherical caps. When the excitation light passes through the cylindrical body of the droplet, which is the longest optical path, we detect high intensity of signal from phosphorescent nanoparticles. In contrast, we detect low intensity of signal when measuring on the cap of the droplet. Similarly, when measuring at continuous liquid (oil), which contains no nanoparticles, the signal intensity is negligible. We use the intensity of the signal as a parameter to select the measuring window for reading the phase shift angle, *i.e.* the signal that provides reliable information on oxygen concentration inside the droplets. The average value of phase shift angle is then used to calculate lifetime of phosphorescent nanoparticles and to determine concentration of oxygen in the droplets. Interestingly, while the signal intensity is prone to variation, coming from the geometry of the droplet, the synchronization of the measurement to the passage of the droplet *etc.*, the phase shift angles of droplets at same level of oxygen are the same in each of the droplets with non-identical content of nanoparticles (different in signal intensity). Once again, it shows the advantages of using lifetime-based measurement over intensity-based measurement.

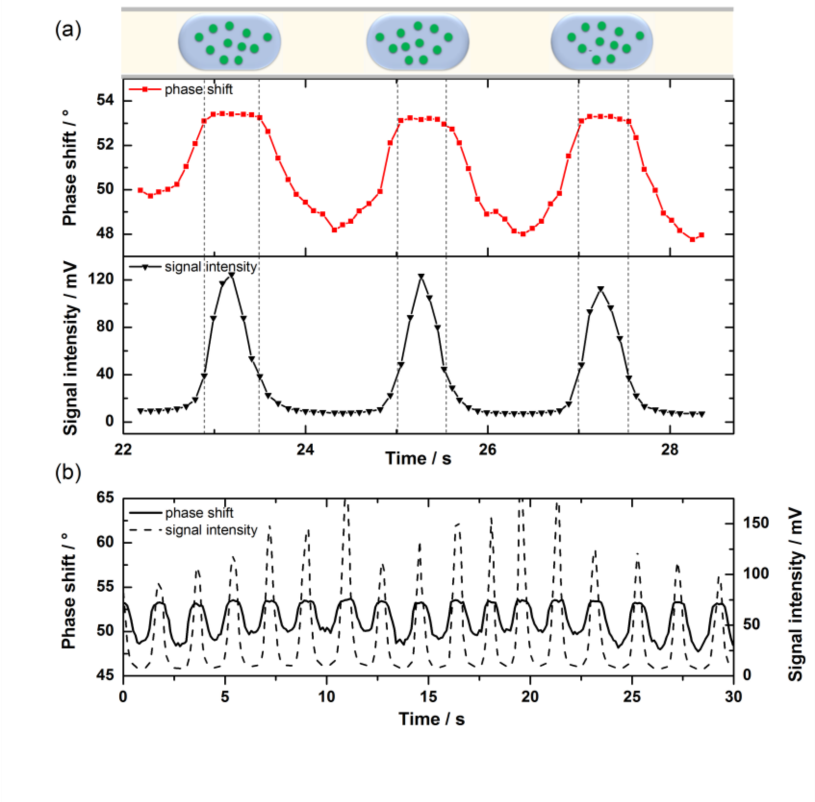

Figure 4.2: (a) Illustration of corresponding phase shift angle and signal intensity recorded when measuring at different positions of droplets or oil. High signal intensity indicates measuring in cylindrical body of the droplet. Low signal intensity indicates measuring at caps of the droplet. When measuring at oil, there is negligible signal intensity. (b) Example of online sensing data of a train of droplets. Phase shift angle is recorded into log only when signal intensity is above 40 mV. The average value of phase shift angle of this train of droplets is 53.27 ± 0.18 degree.

4.2.4 Monitoring bacterial growth and concentration of oxygen in microdroplets

We grow two species of bacteria, *Escherichia coli* ATCC 35218 and *Mycobacterium smegmatis PCM 661 (Polish Collection of Microorganisms)* in microdroplets. In each experiment, we generate 10 identical droplets. We seed bacteria in the mixture of fresh media (LB medium for *E. coli* and Middlebrook medium enriched with Middlebrook OADC for *M. smegmatis*) and oxygen sensor nanoparticles. In addition, we also formed control sets of droplets that contained only the fresh media and oxygen sensor nanoparticles. In the experiment we cycle the droplets back and forth in the incubation part of the system. Every 10 minutes, we record both OD at $\lambda = 600$ nm and oxygen concentration from each droplet to obtain the evolution of concentration of oxygen and optical density (Figure 4.3 and Figure 4.4). We calculate the mean values of OD and oxygen concentration for the ten droplets in each set. The error bars represent the standard deviation of this mean. The OD measurements show a typical exponential growth curve of *E. coli* in microdroplets, while, in the control set, OD remains at almost zero level. This indicates that we do not have cross-contamination (*i.e.* transfer) of bacterial cells between the droplets during incubation.

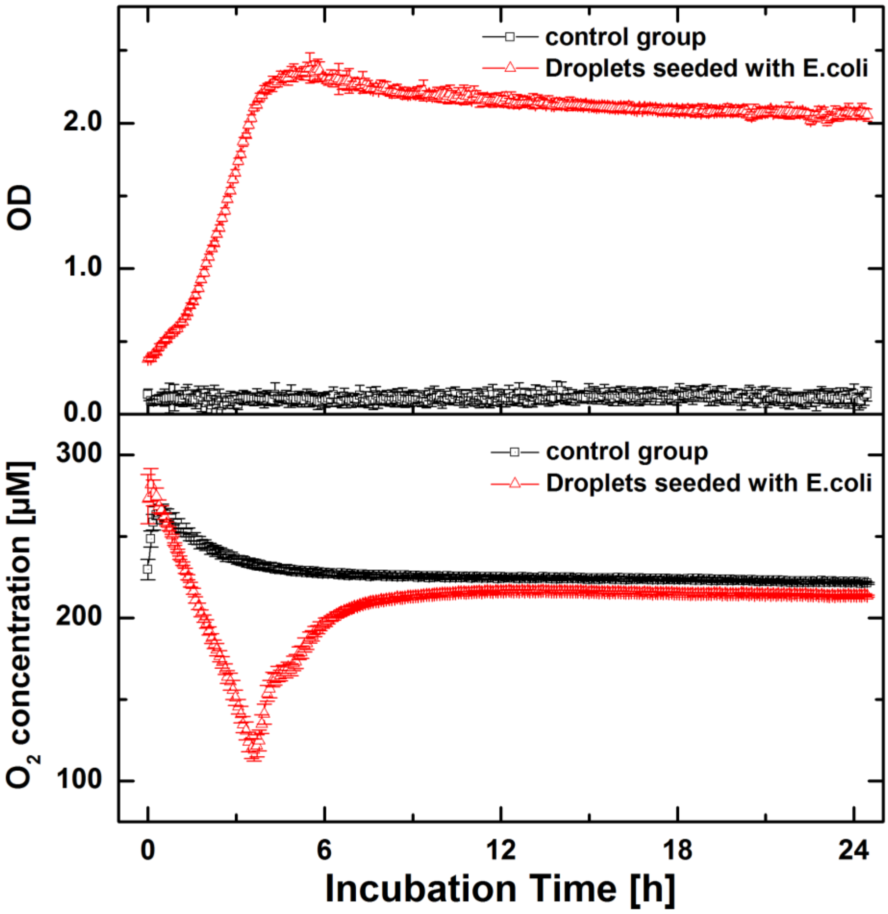

Figure 4.3: Monitoring of OD (Top) and concentration of oxygen (Bottom) during 24 hours incubation of control set of droplets and experiment set - droplets seeded with *E. coli* ATCC35218.

In both sets, the evolution of oxygen concentration shows a small hump at the very beginning of incubation. This small increase of oxygen concentration in droplets is due to two reasons: i) continuous liquid (FC40) has a higher solubility of oxygen than the aqueous phase. There is a non-negligible mass transfer of oxygen from oil to droplets. We observed fast transfer of oxygen from air-saturated oil to a single deoxygenated droplet when flowing in the tubing (Figure 4.8). ii) The droplets are generated at room temperature (20 °C), and only later transferred to the incubation part of the system that is maintained at a higher temperature (37 °C). The calibration curves show that the phase-shift recorded from the oxygen sensor nanoparticles is sensitive to temperature. So before the droplets reach the incubation temperature, there is a small difference of measured and real oxygen concentration in droplets.

The most significant effect that we observe is the decrease of oxygen concentration in the droplets containing *E. coli*. We observe a simultaneous increase of OD in these droplets, reflecting the first, exponential phase of growth of the colony of microbes. This is consistent with that in the exponential growing phase, *E. coli* has the greatest oxygen consumption rate. This huge amount of oxygen consumed in the exponential growth phase leads to the substantial decrease of oxygen concentration in the droplets. We do not observe this phenomenon in the control group.

Eventually, the concentration of oxygen in the droplets reaches an equilibrium level. From the growth curve of *E. coli* in droplets, we can see the bacteria are at the stationary phase, characterized by a limited oxygen consumption rate. The fluorinated oil provides sufficient oxygen supply to the droplets which compensates the oxygen consumed by bacteria in the droplets. The transfer of oxygen from oil into the aqueous phase is a rather fast process. We show that a single oxygen-free droplet needs around 15 seconds to reach air-saturation after immersion in air-saturated oil (FC40) in our microfluidic system (Figure 4.8). The fluorinated oil (FC40) has a much higher oxygen solubility than water. And in this droplet microfluidic culturing system, the volume of continuous phase (oil) is hundreds times of the volume of droplets in the system. Nevertheless, the Teflon FEP tubing shows good oxygen permeability (Figure 4.10). So we haven’t observed complete oxygen depletion in our study. The stable value of oxygen concentration in droplets are similar in both experimental and control group droplets.

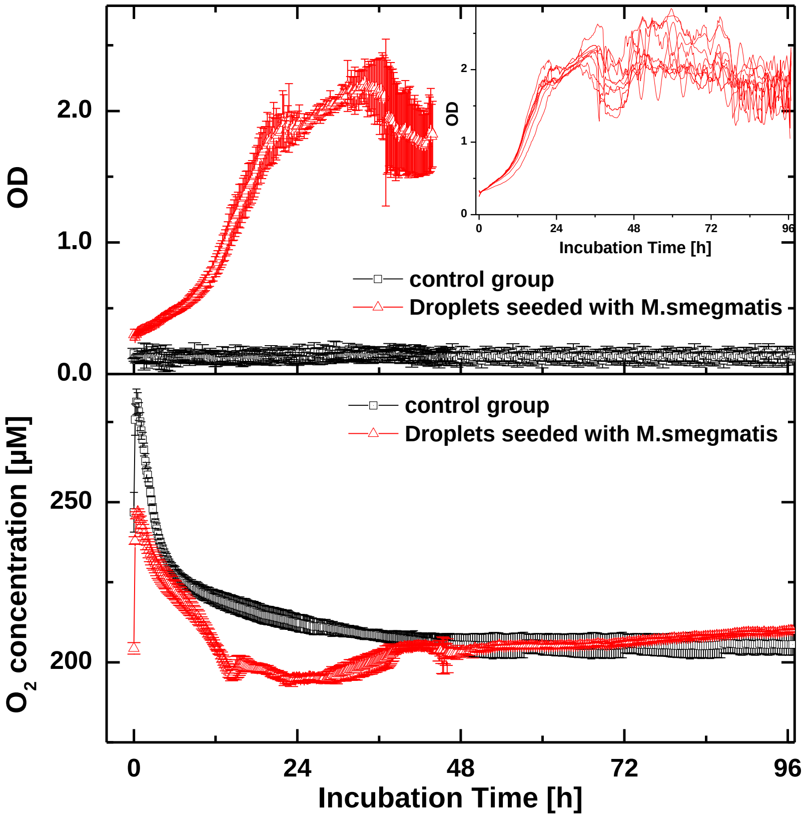

Figure 4.4: Monitoring of OD (top) and concentration of oxygen (bottom) during 96 hours incubation of control set of droplets and droplets seeded with *M. smegmatis* PCM661; inset: OD measurement of each of 10 droplets seeded with *M. smegmatis* during 96 hours incubation.

We also performed an analogous set of experiments to the ones described above but with *M. smegmatis*. *M. smegmatis* comes from the same genus (*Mycobacterium*) as a pathogenic factor for tuberculosis (*Mycobacterium tuberculosis*). *M. smegmatis* grows slowly (a doubling time of 3 to 4 hours) and has an tendency to clump[155]. The clumps cause fluctuation in the OD measurement. We added Tween 20 in the growth media to reduce clumping, but the OD measurement still shows substantially higher error bars for each measurement (Figure 4.4 and the inset) than in the case of *E. coli*. Meanwhile, monitoring of the oxygen concentration is not influenced by clumping of *M. smegmatis*. The relative standard deviation of each measurement point is comparable to the experiment with *E. coli* (Figure 4.3). The oxygen concentration is decreased during exponential growing phase, but it remains at a high level. On one hand, the long doubling time gives small rate of oxygen consumption by *M. smegmatis*. On the other hand, the oil phase supplies oxygen into droplets during incubation. We still detect a slight difference of oxygen concentration between the experimental set and the negative control set. The oxygen sensor nanoparticles provide a feasible method for measuring the concentration of oxygen also in cultures of bacteria that aggregate. This potentially can be adapted to detect growth of slow growing bacteria by monitoring oxygen uptake.

4.3 Conclusions

We have shown accurate online phosphorescence lifetime-based measurement of dissolved oxygen inside of microdroplets using oxygen sensor nanoparticles. These sensor nanoparticles show great potential for biological applications in microfluidic systems since they are autoclavable, not interfering with microorganism, easy to integrate with microfluidic devices.

We demonstrated simultaneous monitoring of both the concentration of oxygen and OD in droplets during incubation of *E. coli* and *M. smegmatis*. It is the first time we reveal the profile of absolute values of oxygen concentration in each droplets during bacterial incubation. The oxygen sensor nanoparticles are robust in non-perfect suspensions, *i.e.* clumping cell culture. The accurate characterization of dissolved oxygen will be useful in engineering of oxygen supply in the microenvironment for bacterial growth in droplet microfluidic culturing systems.

Other applications of droplet microfluidic technologies could also benefit from accurate characterization of oxygen concentration in droplets with this simple tactic of measuring oxygen concentration in small volumes. The system certainly allows for fundamental studies of oxygen transfer and mass transfer in microfluidic systems.

4.4 Materials and methods

4.4.1 Preparation of oxygen sensor nanoparticles and calibration

Oxygen sensor nanoparticles were prepared by staining oxygen sensitive dye Platinum(II) *meso*-tetra(4-fluorophenyl)tetrabenzoporphyrin (PtTPTBPF) in poly(styrene-*block*-vinylpyrrolidone) (PSPVP) beads. The oxygen sensitive dye PtTPTBPF was synthesized in-house, and has absorption maximum at 430 nm and 614 nm, and emission wavelength at 760 nm[151]. The preparation of sensor nanoparticles was following the procedure reported by Borisov *et al.*[154]. Briefly, PSPVP polymer emulsion is diluted with the mixture of THF and water. PtTPTBPF is dissolved in THF and added dropwise into polymer emulsion. Then we concentrated the emulsion under reduced pressure until all ethanol is removed. The oxygen sensor nanoparticles were calibrated at both 20 °C and 37 °C (see Figure 4.5).

Frequency-domain lifetime measurement (phase shift) was conducted by Fiber-Optic Oxygen Meter Piccolo2 (Pyro Science GmbH, Germany) equipped with focusing lens (GRINTECH GmbH, Germany) which enables detection in microfluidic channels. The excitation light is focused to an area about 80 µm inside the channel[119]. Measuring frequency used in this work is 10 Hz.

This method has an intensity-modulated light as excitation source. The time lag between absorption and emission causes the delay of emission light to modulated excitation light. This delay is recorded as angle of phase shift (φ). The relation between phase shift angle and lifetime of oxygen sensitive probe is described below[156]:

$$\tau = \frac{\tan \varphi}{2\pi f}$$

Where φ is phase shift angle (dphi); f is the frequency of modulation of light source.

4.4.2 Microfluidic cell culturing device

We fabricated similar system to Cybulski *et al.* work[150]. We built a single T-junction to generate droplets with the same content and incubating module to culture bacteria. Our system was extended by Piccolo2 reader to measure oxygen level in passing droplets. First, we use a syringe pump to fill up aspiration tube with aqueous solution. During this procedure the manual valve close to the syringe and valve V_{waste} are opened. Then we close the manual valve (V_{inlet}) and remove the rest of solution by oil from valve V_{oil2}. After pressure is stabilized in the tubing, the system is ready to generate droplets for incubation. To generate droplets, valve V_{oil1} is switched on while valve V_{waste} is opened to maintain constant hydrodynamic resistant in the system. After the generation, we flow the droplets into incubation part by switching valves V_{oil2} and $V_{out1.}$ After the generation of a set number of droplets system moved automatically to incubation state. During this state we open the valves V_{in1}-V_{out2} and V_{in2}-V_{out1} alternatively to cycle the droplets back and forth.

In our system we have two independent readouts from each droplet: oxygen concentration *via* Piccolo2 and optical density *via* custom build electronic. We use the signal from Piccolo2 in feedback loop to count droplets. We measure OD at 600 nm with red LED and a light to voltage converter (TSL257, ams AG, formerly TAOS). Voltage signal is filtered and gained by custom made electronic and then acquired by National Instruments I/O device (SCB68). We collect samples with a frequency of 20kHz. For each droplet we measure mean value from 50% of samples from middle part of the droplet. The time needed for a droplet to pass under OD reader is around 700ms therefore the result for each droplet is calculated from around 7000 samples.

During the demonstration of oxygen measurement in droplets (Figure 4.2), we used two syringe pumps (World Precision Instruments, USA) to generate droplets *via* a T-junction built by fluidic connector.

4.4.3 Bacteria and Media used

We used two species of bacteria: fast growing *Escherichia coli* ATCC 35218, and slow growing *Mycobacterium smegmatis* PCM 661 (Polish Collection of Microorganisms). We cultivated *E. coli* in LB medium (Roth, Germany) with addition of 100 µg/ml ampicillin (Roth, Germany), and *M. smegmatis* in Middlebrook 7H9 (BD, New Jersey, USA) medium enriched with OADC enrichment (BD, New Jersey, USA), plus 1% Tween 80 (Sigma Aldrich, Germany) (in order to avoid clumping of bacterial cells).

For each experiments we used freshly seeded bacteria in final optical density 0.2, which we diluted with nanoparticles, reaching 20x diluted sensors.

4.5 Supporting information

Characterization of optical oxygen sensor nanoparticles and investigation of oxygen transfer in microdroplets cell culturing system.

4.5.1 Optical Oxygen Sensing Principle

The sensing principle of most optical oxygen sensors is based on collisional quenching. The decrease of intensity and lifetime of oxygen sensitive probe is proportional to the amount of oxygen molecules present, which is described by an adapted Stern-Volmer equation from the two-site model[9]:

$$\frac{F_0}{F} = \frac{\tau_0}{\tau} = \left(\frac{f}{1 + K_{SV1} \times [O_2]} + \frac{1 - f}{1 + K_{SV2} \times [O_2]}\right)^{-1}$$

where F_0 (τ_0) and F (τ) are the luminescence intensities (lifetime) in the absence and presence of the quencher, oxygen; K_{SV1}andK_{SV2} are the Stern-Volmer constants, which describes the quenching efficiency for two micro-environment ; f is the distribution coefficient between the two media, and $[O_2]$ is the oxygen concentration in the sample.

In this model, the sensor molecules are assigned to two different micro-environments within the hosting polymer, with different oxygen permeability. K_{SV1}, K_{SV2} and f are identical for the same batch of nanoparticles. A full calibration of oxygen sensor nanoparticles at 20 °C and 37 °C are done in bulk solution (see Figure 4.5) to identify the values for K_{SV1}, K_{SV2} and f. For use of oxygen sensor nanoparticles in microfluidic system, we perform *in-sit*u calibration by a simplified two-point calibration to identify lifetime of oxygen sensor nanoparticles at air saturated and oxygen free conditions by using air-saturated water and anoxic aqueous solution of 0.1% wt of sodium sulfite.

4.5.2 Calibration of Oxygen Sensor Nanoparticles

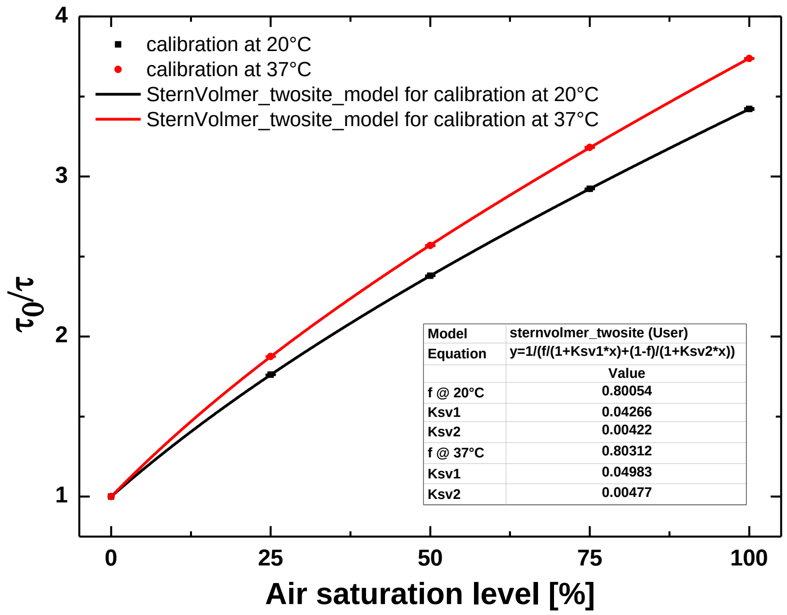

Figure 4.5: A full calibration for PSPVP oxygen sensor nanoparticles at 20 °C and 37 °C to determine values forK_{SV1}, K_{SV2} and f. Oxygen sensor nanoparticles are dispersed in DI water in a closed glass vial. Gases with different concentrations of oxygen are flushing through oxygen sensor nanoparticles dispersion to obtain different air saturation level in the dispersion. Calibration gases are produced by mixing nitrogen and compressed air using a computer controlled gas mixing device (Vögtlin Instruments, Switzerland). Phase shift angle (dphi) are recorded by Piccolo2 to calculate lifetime of oxygen sensor nanoparticles at different concentrations of oxygen.

4.5.3 Autoclavability and Biocompatibility of Oxygen Sensor Nanoparticles

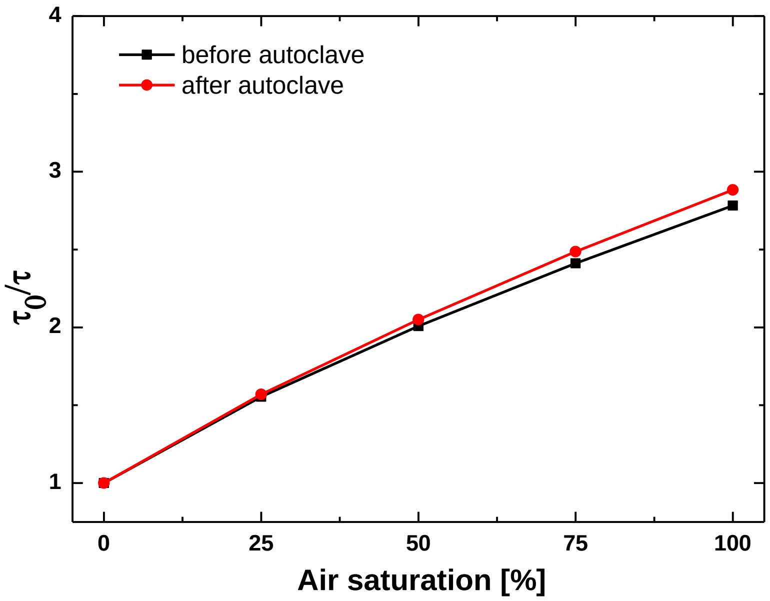

Figure 4.6: Full calibration of oxygen sensor nanoparticles before and after autoclave (5 cycles of autoclaving of 15 minutes at 121°C). Very similar oxygen sensitivity is shown by comparing calibration curves. Oxygen sensor nanoparticles remain nearly same properties after autoclave.

We determine the influence of oxygen sensor nanoparticles on Gram-negative and Gram-positive bacteria: *Escherichia coli* ATCC 35218 and *Staphylococcus epidermidis* DSMZ 20044. We dilute the particle stock solution (10 mg/ml) 5 times in LB (Luria/Miller) medium (Roth, Germany), autoclave it and use it as an initial solution for series of multiple dilutions. We perform our experiment with 96 well microdilution format. In each wells of 96 well plate (Greiner, Germany), we add 90 µl of particles and 10 µl of bacteria to achieve final density of inoculum of 1x10^5 CFU/ml. We measure OD_{600} value in multiwell plate reader (Synergy HTX, Biotek, USA) before and after 18 h of incubation in 37°C. The survival rates of *S. epidermidis* and *E. coli* at different dilutions of sensor nanoparticles are shown in Figure 4.7a. We also compare the growth curves of *E. coli* in LB media and in LB media with oxygen sensitive nanoparticles. We incubated 100 µl *E. coli* suspensions (1x10^5 CFU/ml) with and without oxygen nansensor particles diluted 10 times and measured OD_{600} every 10 minutes (shaking 2 minutes linearly before each read out). We haven't observed any significant difference in the shape of bacterial growth curves with or without sensor nanoparticles (see figure 4.7b).

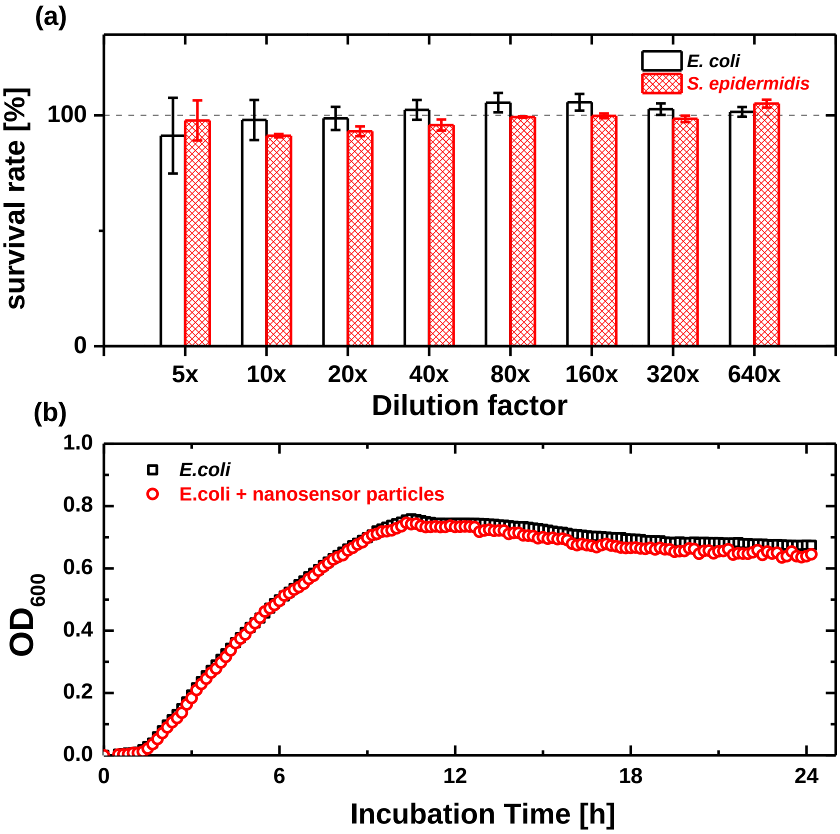

Figure 4.7: (a) Survival rate of Gram-negative and Gram-positive bacteria: *Escherichia coli* ATCC 35218 and *Staphylococcus epidermidis* DSMZ 20044 after 18 hours incubation at 37°C in the suspension of oxygen sensor nanoparticles in LB (Luria/Miller) medium (Roth, Germany) at a series of multiple dilutions; (b) Growth curves of *E. coli* ATCC 35218 in LB media and in LB media with oxygen sensitive nanoparticles (at concentration 1 mg/ml) for 24 hours incubation at 37°C.

4.5.4 Fast Oxygenation of Low Oxygen Microdroplets by Carrier Oil (FC40) in Microfluidic Culturing System

We deoxygenate aqueous solution to generate a single droplet with low oxygen concentration and measure the change of oxygen concentration in the droplet while moving it by oil phase (experimental procedure is described in figure 4.9). A fast transfer of oxygen from air saturated oil to low oxygen droplet is shown in figure 4.8. The droplet reaches air-saturated level after about 10 seconds circulation in the bacterial incubation part of microfluidic culturing system.

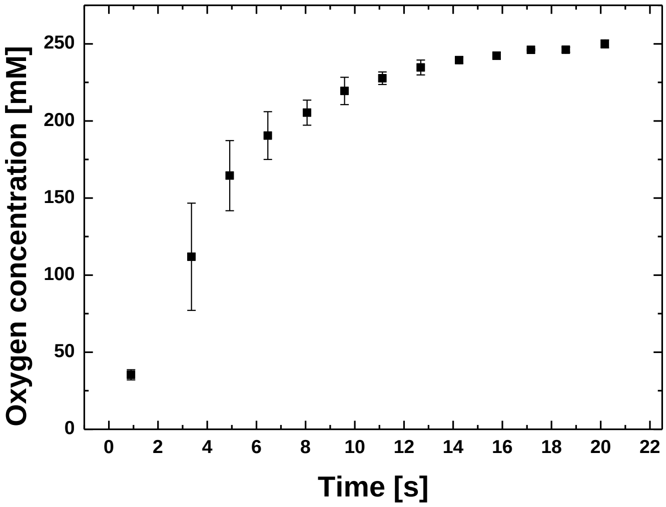

Figure 4.8: Kinetic of oxygen transfer from air saturated carrier oil (FC40) to oxygen low aqueous droplet while moving in the bacteria incubation part of microfluidic culturing system.

Due to very fast oxygen transfer from FC40 oil to oxygen free solution we had to build slightly different system with changed control algorithm. Idea was to generate only one droplet and move it back and forth with higher possible frequency. Moreover, in previously described culturing system distance between droplets generator and detection point was to long therefore we had also minimized that. We did it by moving generation of droplet possibly close to oxygen reader. Moreover, algorithm follow level of oxygen directly before droplet generation therefore we could measure almost beginning of oxygen transfer from oil to droplet. Herein we did readout 7 readouts from each droplet with time intervals ca. 700 msec. Time of intervals was limited by system inertia going from valve delay, oscillating of material volume due to pressure flow, and also dynamic behavior of droplet. Another point worth to mention here is difficulty in filling aspiration tube by solution with constant low oxygen level. Mainly because oxygen can also transfer through tubes from ambient atmosphere and also it should be take a count that oxygen may transfer from material structure. To avoid this problem aspiration tube (yellow dashed rectangle) was dip overnight in 2% solution of sodium sulfite. To obtain the same conditions as in previously described droplets culturing system we kept incubation part surrounded by air (out of sodium sulfite solution).

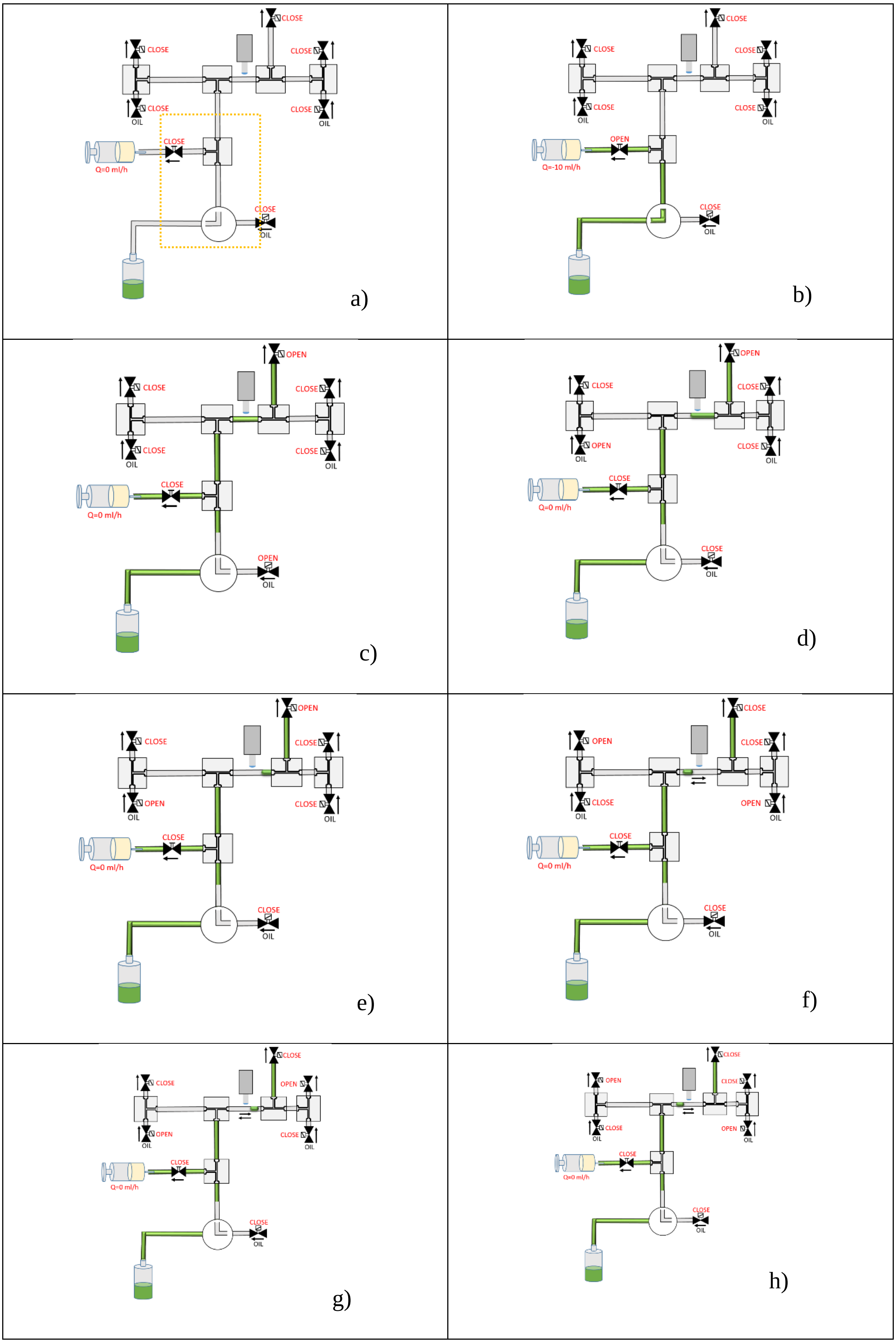

CLOSE
CLOSE
CLOSE
CLOSE
CLOSE
OIL
OIL
CLOSE
Q=0 ml/h
CLOSE
OIL
a)
CLOSE
CLOSE
CLOSE
CLOSE
CLOSE
OIL
OIL
OPEN
Q=-10 ml/h
CLOSE
OIL
b)
OPEN
CLOSE
CLOSE
CLOSE
CLOSE
OIL
OIL
CLOSE
Q=0 ml/h
OPEN
OIL
c)
OPEN
CLOSE
CLOSE
OPEN
CLOSE
OIL
OIL
CLOSE
Q=0 ml/h
CLOSE
OIL
d)
OPEN
CLOSE
CLOSE
OPEN
CLOSE
OIL
OIL
CLOSE
Q=0 ml/h
CLOSE
OIL
e)
CLOSE
OPEN
CLOSE
CLOSE
OPEN
OIL
OIL
CLOSE
Q=0 ml/h
CLOSE
OIL
f)
CLOSE
CLOSE
OPEN
OPEN
CLOSE
OIL
OIL
CLOSE
Q=0 ml/h
CLOSE
OIL
g)
CLOSE
OPEN
CLOSE
CLOSE
OPEN
OIL
OIL
CLOSE
Q=0 ml/h
CLOSE
OIL
h)

Figure 4.9: Schematics of experimental procedure for generating low oxygen droplet: a) droplets generation module was left over night in sodium sulfite solution (1 wt%) to remove oxygen from material structures, b) in

next step water solution with NPs which was initial deoxidize by argon was sucked *via* syringe pump to aspiration tube and left until rest of oxygen was removed by surrounding sodium sulfite, steps (c-d) were performed automatically controlled by custom LabView program. c) water solution was driven by oil to detection point, d) when oxygen level was lower than 50mM then valves switched occur and droplet was formed (e). Figures (f-h) shows cycling of droplet with possibly higher frequency of passing under detection point (~1.5 Hz).

4.5.5 Oxygen Transfer From Ambient To Inside of Tubing of Microfluidic Culturing System

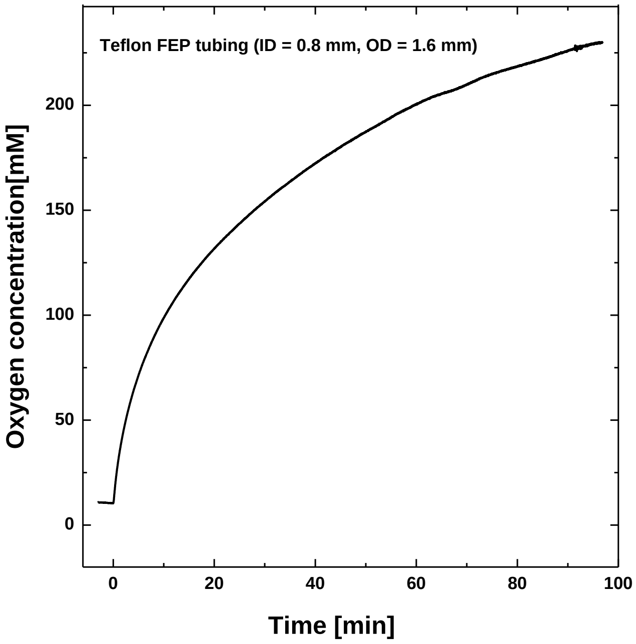

Figure 4.10: Oxygen concentration in Teflon FEP tubing (ID = 0.8 mm, OD = 1.6 mm) after filling with water with low concentration of oxygen.

4.5.6 Determination of Oxygen Concentration in Each Individual Microdroplet

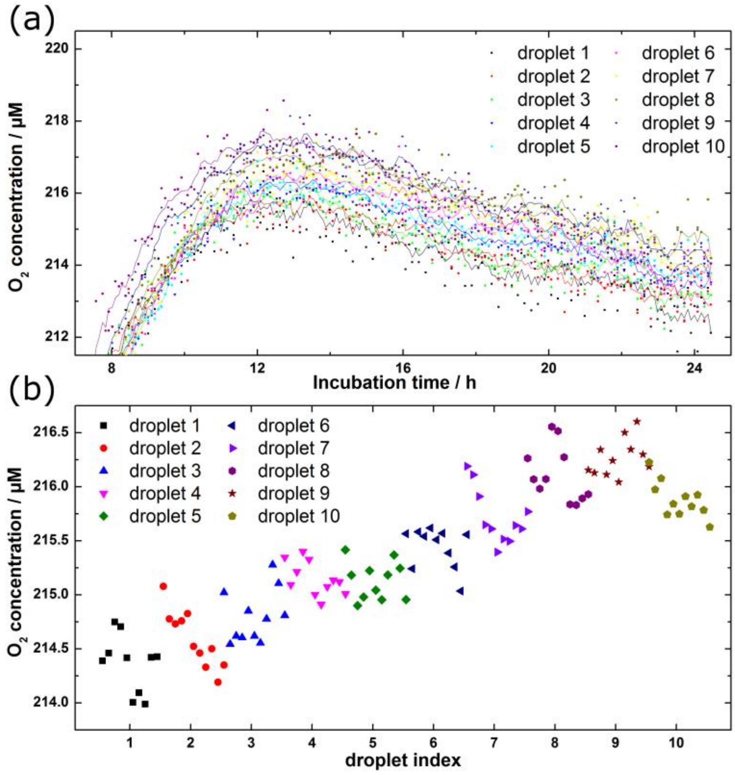

Figure 4.11: (a) Oxygen concentrations in each of the droplets seeded with *E. coli* ATCC35218 between 12 to 24 hours of incubation. (b) Ten consecutive measurements of oxygen concentration in each of the ten droplets seeded with *E. coli* ATCC35218 during one hour (hour 16.7 – 17.6) of incubation.

Figure 4.11 illustrates the determination of oxygen concentration in each individual microdroplet. After the first 12 hours of incubation of droplets seeded with *E. coli*, the concentration of oxygen in the droplets is stable. Interestingly, we observe that there is small difference of oxygen concentration in each droplet due to the sequence of the droplets in the train. In experiment, we generate a sequence of 20 droplets. The first 10 droplets are the control group (containing only the fresh media and oxygen sensor nanoparticles) to check if there is any cross-contamination. And they are labelled as control 1 – 10. After the control group, we generate the experiment group droplets, which are seeded with *E. coli*. They are labelled as droplet 1 -10. Droplet 1 is in the middle of the whole sequence of the droplets, and droplet 10 is at the very end of the sequence. The large number droplets (e.g. droplet 9 and 10 in Figure 4.11) is in direct contact with or closer to ambient oil on one side. Therefore, it benefits most from the oxygen transfer from oil to droplets. The following droplets are only in contact with limited amount of oil, since there is only a finite amount of oil between each pair of droplets and because very little oil bypasses the droplets when they flow. A subtle trend of oxygen concentration is shown in Figure 4.11a from the head to the tail of the train of the droplets. And Figure 4.11b presents ten consecutive measurements of oxygen concentration in individual droplets during one hour (hour 16.7 – 17.6) of incubation. We confirmed this trend of increasing amount of oxygen when droplets are closer to ambient oil. This information could be interesting for researchers working with large number of droplets in microfluidic cell culturing systems.

4.5.7 Technical Drawing of Teflon FEP Fluidic Connector

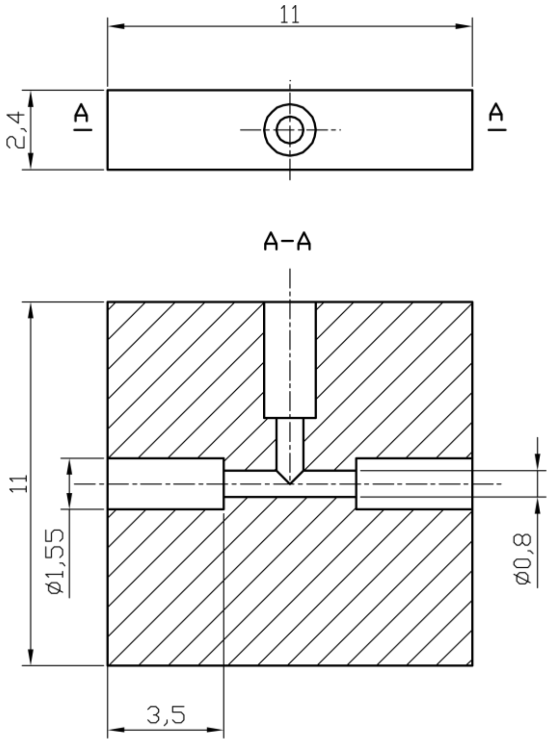

Figure 4.12: Technical drawing of Teflon FEP connector (unit mm).

4.6 Acknowledgement

This work has received funding from the People Programme (Marie Curie Actions, Multi-ITN) of the European Union’s Seventh Framework Programme for research, technological development and demonstration under grant agreement no° 608104 (EUROMBR) and the European Research Council Starting Grant 279647. PG additionally acknowledges support from the Foundation for Polish Science with the Idee dla Polski programme.

5 Using pH sensor nanoparticles to monitor pH change in droplets during cell culturing

5.1 Introduction

Using droplets microfluidic for biological experiments

Droplet microfluidics have become an emerging tool for biological experiments [26]. The droplets provide the so-called “stochastic confinement” [128]. Each of these confinements serves as a separated bioreactor, when with encapsulation of single cells or small populations of microorganisms. These nanoliter- to microliter-sized bioreactors separate single or small population of cells from the bulk and provide an effective volume to detect the molecules excreted by the cells and then accumulates to a higher measureable concentration in droplets than in the bulk. With the capability of precise handling and online monitoring, droplet microfluidics has been used to perform experiments in a well-controlled manner and in a great quantity for statistic or high throughput purpose.

For different applications, pH plays a role

With the merits of droplet microfluidics, it has been applied in different fields of microbiological study: i) screening and selection of new / rare species; ii) tests of antibiotic susceptibility; iii) physiological study on single cell or small populations of bacteria; iv) biotechnological applications; and v) detection or isolation or pathogens. Among all these applications, monitoring of pH plays an important role. On one hand, cells need to grow in suitable range of pH. It is fundamental to determine the optimal range of pH for the strain in biotechnology industry. The certain range of pH may also be the selecting criteria for a new industries strain. On the other hand, change of pH indicates the metabolic activities of cells. When growing cells in droplets, the molecules excreted by the cells can effectively fluctuate the pH in the droplets. The fluctuation of pH indicates the physiological condition of the cell. This indicator can in selection of new species, in tests of antibiotic susceptibility, and the isolation of pathogens. For example, chapman medium (Mannitol Salt Agar) is used to detect pathogen *Staphylococcus aureus* by change of pH. Chapman medium is a selective and differential medium, which encourages the growth of *S. aureus* while inhibits the others. The growth of *S. aureus* causes the decrease of pH in the medium. When pH is below 6.8, the color of the indicator dye Phenol Red in the medium changes from red to yellow.

Previous work on pH measurement in droplets and its limitations

The most common way to measure pH is using electrode, which is an electrochemical method. Several works have miniaturized the electrode and integrate it into the single phase microfluidic systems to monitor and control the pH in real-time [157–159]. Also, optical methods for pH sensing have been adopted [35,160–166]. For pH measurement in droplets, the sensor has to be dispersed in the droplet, instead of dispense on the surface of substrate in single phase microfluidics. Therefore, optical approach is the only option here.

Two examples have shown pH measurement in microdroplets by fluorescence intensity-based measurement. Mashaghi et al. dissolved pH sensitive fluorescein in the droplet [167]. Fluorescein is poorly soluble in water. It could easily leak into organic phase and cause the decrease of the fluorescence intensity in droplet. Also biological matters, which were not used in this study, could interfere with fluorescein. Funfak et al. immobilized pH sensitive dye in the polymeric particles and dispersed the particles in aqueous phase [34]. Shielding dye molecules in the polymer matrix can prevent the leakage of the dye and avoid the interaction between dye molecules and cells. But the author still observed continuous change of the fluorescence intensity of the pH sensitive beads in the droplet with constant pH. We believe this approach requires further validation and improvement. In both studies, the authors used either inverted fluorescence microscope or homemade flow through fluorometer for readout. Both of them are bulky and expensive.

Nanoparticles sensors with lifetime-based measurement to monitor pH and oxygen simultaneously

Here we propose a method of using nanoparticle sensor with lifetime-based measurement to monitor pH in droplets. The readout device Piccolo2, a miniaturized fluorometer, is portable and can measure at different locations in different microfluidic systems. We embed the pH sensitive dye in the core-shell structured nanoparticles. It prevents the leakage of the dye into oil phase and the interference with cells. The lifetime-based measurement gives accurate information on pH because it is not affected by ambient light, dye bleaching, or instrument variations like intensity-based measurement. But the further investigation shows the unstable energy transfer within the nanoparticles which causes dynamic changing of the property of the optical sensors. Therefore, we could not provide accurate information of pH in droplets. Further optimization of the sensor design is needed for working within complex media.

In this work, we validate the feasibility of using nanoparticles sensors to measure pH in microdroplet. And we tried to demonstrate the monitoring of pH, concentration of oxygen, and optical density at the same time in droplet cell culturing system. During the investigation of identifying pathogenic strain *S. aureus* from non-pathogenic strain *S. epidermidis* based on the difference of their metabolic profile in selective medium, we found the problem with pH nanoparticles.

5.2 Results

5.2.1 Measuring principle for pH sensing and its calibration

The optical pH indicator used in this study is a fluorescent dye. It was earlier developed and modified in our group. Several derivatives of the pH indicator dyes were developed for a broad range pH measurement. These indicator dye exhibit Photoinduced Electron Transfer (PET) effect. Jokic et al. discussed the principle and the advantages of this set of dyes for pH sensing[11]. Briefly, this aza-BODIPY dye shows higher fluorescence intensity and longer fluorescence lifetime at high concentration of hydrogen ions than at low concentration of hydrogen ions.

The fluorescence lifetime is relatively short, usually in the range of nanoseconds. To detect the lifetime of luminescent material at nano seconds, it requires extreme complicated and expensive instruments. And these instruments are very bulky. It does not serve the purpose of measurement for microfluidic system and it does not have the versatility to use the sensing setup for different microfluidic cell culturing system between different laboratories. Thus, we used the modified dual lifetime referencing method to detect the change of short-lifetime pH indicator. This method is compatible with our miniaturized fluorometer Piccolo2. For single frequency measurement with Piccolo2 for long-lifetime luminescent indicator (e.g. Platinum-based oxygen indicator), the excitation light source is modified sigmoidally. At different concentrations of the analyte, the indicator exhibits different intensity and lifetime of luminescence. The different length of the lifetime causes the different length of the delay of the emission light, which results in the different angle of phase shift from the excitation light to the emission light. This information of phase shift is recorded for calculation of the concentration of the analyte. In the modified dual lifetime referencing method, two luminescent indicators are used. One indicator has long lifetime (as shown as P in Figure 5.1), which can be measured by the device. The other indicator is short lifetime (as shown as F in Figure 5.1), which cannot be measured by the device. During the measurement, two frequencies of the excitation light are generated. The device records the phase shift information from the overall signal from the two indicators (as shown as TS in Figure 5.1). We assume the phase shift recorded at the lower frequency of measurement is mainly contributed by long-lived indicator. Then the lifetime of this indicator is calculated. And this information is used to calculate the lifetime from the other indicator from the measurement at high frequency. In this work, we use the oxygen indicator as the long-lived indicator and the pH indicator as the short-lived indicator for the modified dual lifetime referencing method. This approach is originally from Ehgartner et al.[35]. During the cell culturing in droplets, we are able to measure pH and concentration of oxygen simultaneously.

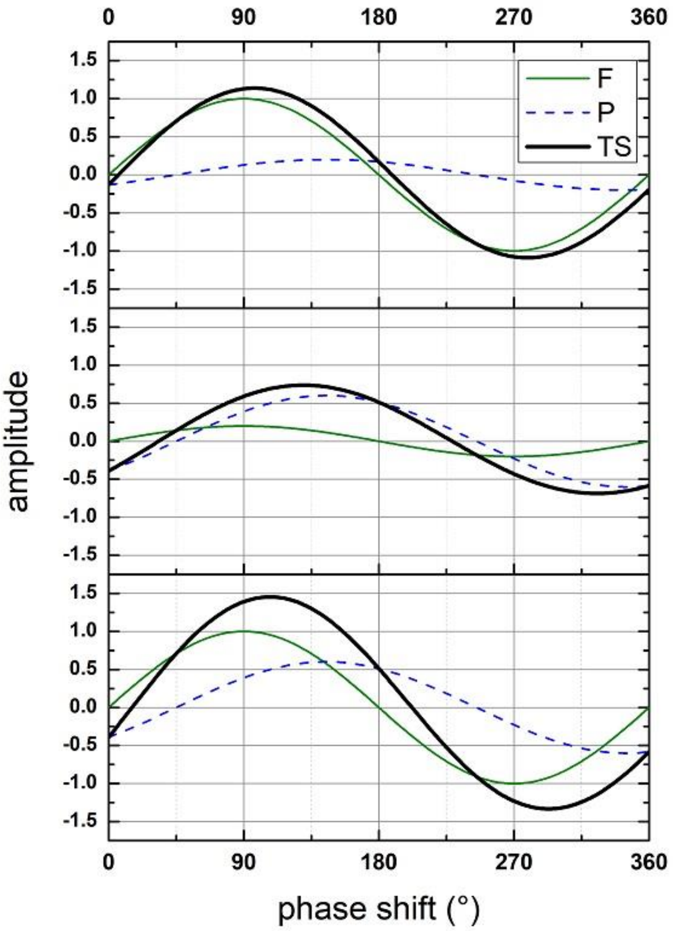

Figure 5.1: Illustration of modified dual lifetime referencing method. F represents the signal from short-lived indicator; P represents the signal from long-lived indicator; TS represents the total signal.

To measure two analytes, pH and concentration of oxygen, both of them need to be calibrated before use. We calibrate the sensor system at different pH and different concentrations of oxygen. For the calibration of measurement of pH, the cotangent value of phase shift of the sensor fits the boltzmann function at each oxygen level. When presenting the full calibration in three dimensions, each point on the calibration surface present the signal corresponding to one pH value at certain oxygen concentration.

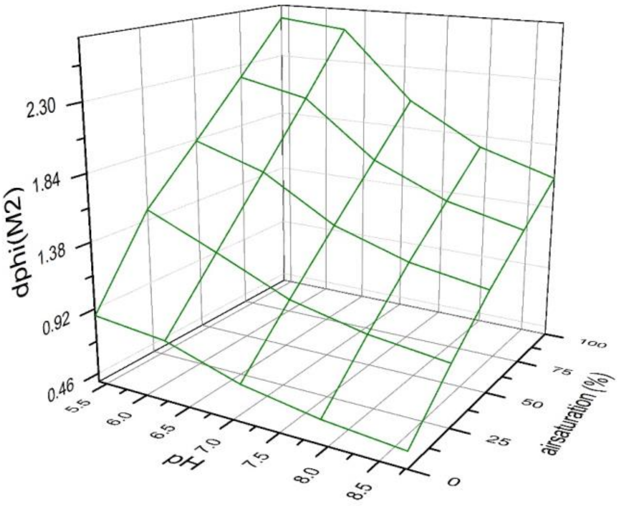

Figure 5.2: 3D calibration surface for pH and concentration of oxygen dual sensor nanoparticles.

5.2.2 Extended dynamic range of optical pH sensor

The dynamic range of optical pH sensor, which is defined by its pKa value, is usually limited to 2-3 units of pH. The pka value + or – 1 defines the working range of this sensor. This limitation is due to the definition of pH. As described in Henderson-Hasselbalch equation, pH is the sum of the pKa values and the log of the concentration of the conjugate base divided by the concentration of the weak acid. pKa value is the negative of the log of acid dissociation constant.

$$\mathrm{pH} = \mathrm{pKa} + \log\frac{[A^-]}{[HA]}$$

The limitation could be overcome by mixing a couple of or several pH indicators together. Strobl et al. built a broad range pH sensor by different aza-BODIPY dyes which have different pKa values. Following this concept. We stained the nanopartilces with two different kinds of pH indicator dye aza-BODIPY. They have different apparent pKa values. From the Figure 5.3, we can see one sensor is working for the range of 4.4 to 6.4, while the other one is working for the range of 6.1 to 8.1. First, the calibration function of each of these sensor nanoparticles fits the Boltzmann function. Then we mixed these two kinds of sensor nanoparticles together and calibrated the mixture. We still achieved a good fit of the sensor to Boltzmann function. The pKa value of the mixture of the sensors is 6.53, which is located between the pKa values from these pH sensors. And we are also able to extend the dynamic range to more than 3 units of pH.

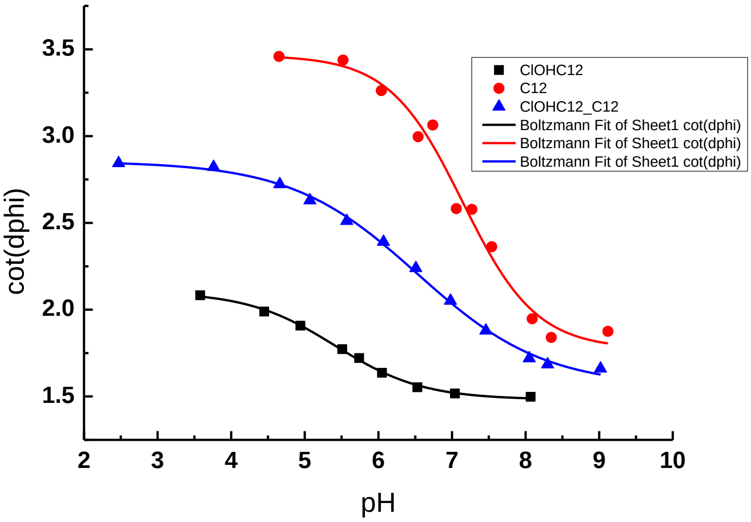

Figure 5.3: Boltzmann function fit for calibration of measurement of pH.

Table 5.1: Parameters for Boltzmann fitting for calibration of pH sensor nanoparticles with different indicator dye entrapped.

aza_BPDIPY Dye	A_1	A_2	x_0	dx	R^2
ClOHC12	2.10	1.48	5.41	0.60	0.99
C12	3.47	1.77	7.15	0.50	0.98
mixture	2.85	1.56	6.53	0.86	0.99

5.2.3 Validation of measurement of pH in droplets

Droplets have such a unique geometry from bulk solution or single phase microfluidics. Each of the droplets has a shape like a capsule. The droplets are separated by continuous phase, usually fluorinated oil. The oil carries the droplets and flows them in the tube. Between the wall of the tube and the droplet, there is a thin layer of oil to prevent the contact of them. Considering the measurement of pH in droplets, the excitation light has to pass through, first the wall of the tube, then a thin layer of oil before reaching the pH sensitive nanoparticles dispersed in droplets. Therefore, we validate the measurement of pH in droplets before the experiments with cells.

We prepared 7 buffer solutions at different pH values. All samples are at air-saturated condition and at room temperature. We collected the signal of phase shift from each samples and obtained calibration curve by plotting cotangent values of phase shift at different pH values. After this, we generated droplets using these solutions. Each group of the droplets has the same pH values as in bulk. Since the high solubility of oxygen in fluorinated oil, small numbers of droplets in the system, and no oxygen consumption by cells in the droplets, we assumed the droplets were all air-saturated in this experiment. Again we collected all the signal of each samples and plotted them out for a calibration curve.

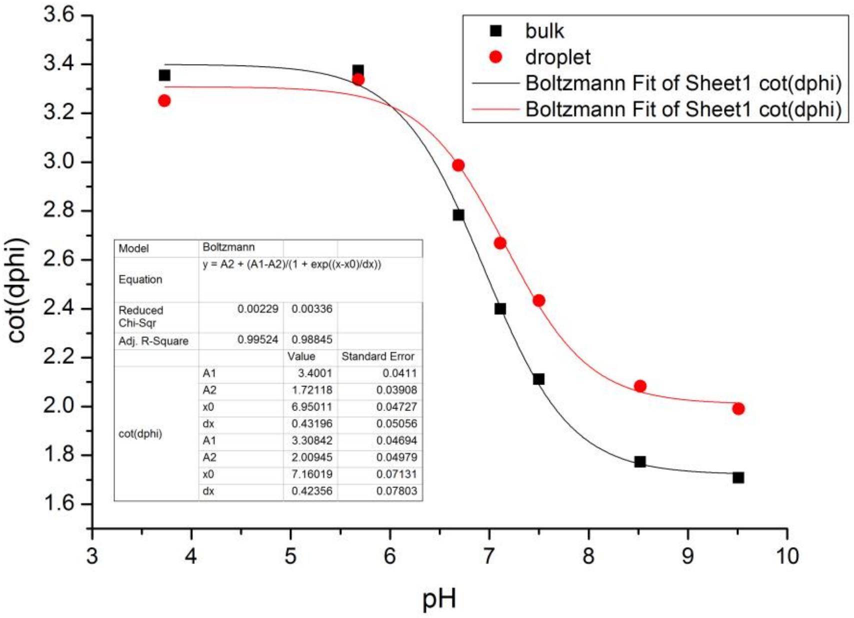

Model	Boltzmann		
Equation	y = A2 + (A1-A2)/(1 + exp((x-x0)/dx))		
Reduced Chi-Sqr	0.00229	0.00336	
Adj. R-Square	0.99524	0.98845	
		Value	Standard Error
cot(dphi)	A1	3.4001	0.0411
	A2	1.72118	0.03908
	x0	6.95011	0.04727
	dx	0.43196	0.05056
	A1	3.30842	0.04694
	A2	2.00945	0.04979
	x0	7.16019	0.07131
	dx	0.42356	0.07803

Figure 5.4: Comparison of measurement of pH in bulk and in droplets.

Two curves of calibration of measurement of pH sensors in bulk and in droplets have similar behaviors. The sensors show the feasibility for measurement of pH in droplets. But there is a

)

significant difference of the parameters defined by the Boltzmann function. In this case, a calibration for pH measurement in droplets is necessary.

5.2.4 Fabrication of the microfluidic culturing system

We fabricated the microfluidic culturing systems with Teflon FEP tubing (inner diameter: 0.8 mm) and customized Teflon fluid connectors, similar to previous work [36]. This time, we have three inlets to generate droplets with different contents. After generation of droplets by a three-way Teflon connector, we flow the droplets into the incubation part and cycle them back and forth. We control the flow of droplets through the system with a set of external valves connected to pressurized reservoirs of oil and to outlets maintained at ambient (atmospheric) pressure. We use a custom-written Lab View script to control all valves. In the detection part, we placed fiber on both sides of tubing for measurement of OD. And we attached piccolo2 to the wall of tubing by a holder to measure the concentration of oxygen.

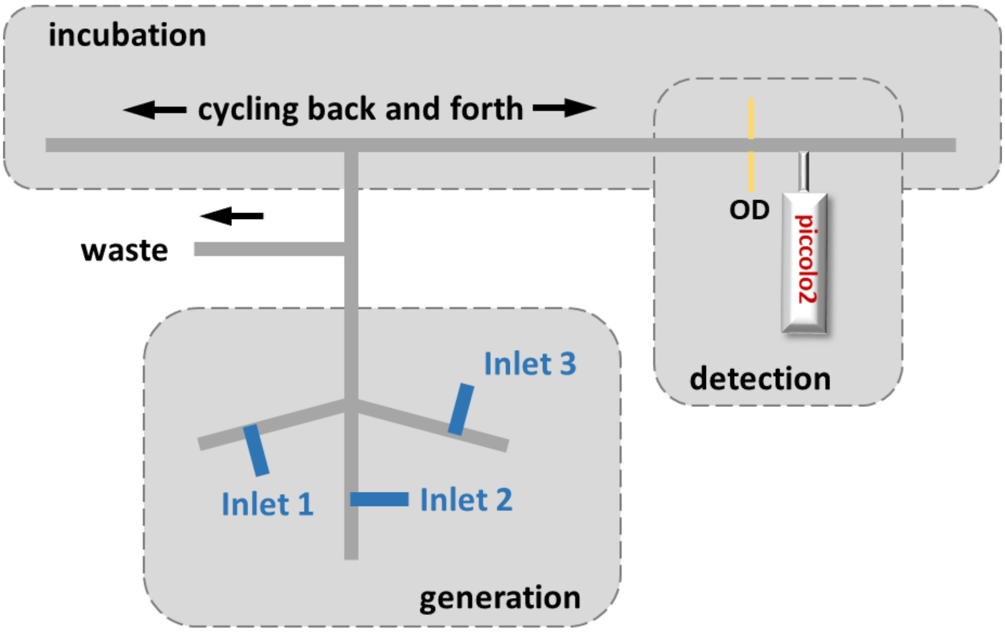

Figure 5.5: Scheme of the microfluidic culturing systems.

5.2.5 Selection of the data from measurement

Collection of data from measurement is a critical part of the measurement in droplets. Data should be collected promptly and properly. Only the data collected from measurement on the droplets is interesting to us. So we first designed the trigger to control the measurement of Picoolo2 to minimize the working time during the cultivation. Optical density measurement is the trigger we used to turn on or turn off the Picoolo2 measurement. The optical density measurement can tell us the position of the droplets in the system. We only turn on the picoolo2 for measurement before the droplet passing by, in order to save the lifetime of the device.

When the droplets are under the detection of piccolo2, the sensor nanoparticles in the droplets show high in signal intensity for the measurement by Piccolo2. On the contrary, when measuring at oil phase, there is no signal detected by Piccolo2 since there is no sensor in the oil phase. So we used the signal intensity as criteria to collect the data.

For the data we collected from each droplet, it consists 8 to 10 measurement when they pass by Piccolo2. In this one set of measurements from one droplet, the first and the last measurements usually give very high or low values. This is because the first or the last measurements are usually at the head or the tail of the droplet. The droplet has a cylinder shape with caps at two ends. The round shape of the caps is like a lens which can affect the optical measurement. So we eliminate the data from first and the last measurement on each droplet.

Moreover, we applied another filter to the data remained. We calculate the average value of the data left from cutting of first and last measurement. Then we compare the average value to the data from each measurement. If the difference of them is greater than the criteria we set, i.e. 10% of average value, we eliminate this measurement too. We calculate the average of the data from the rest of the measurement. And we only use this final average value to calculate the pH and concentration of oxygen for each droplet.

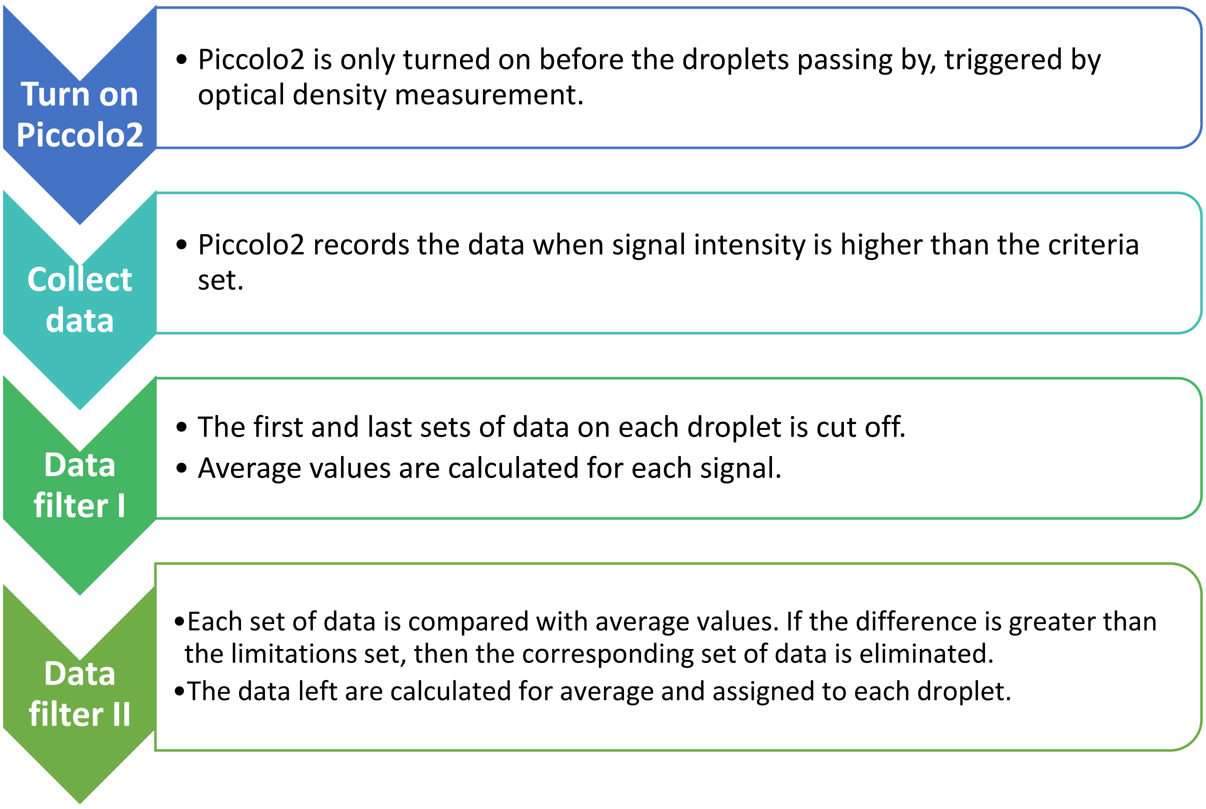

- Piccolo2 is only turned on before the droplets passing by, triggered by optical density measurement.

- Piccolo2 records the data when signal intensity is higher than the criteria set.

- The first and last sets of data on each droplet is cut off.
- Average values are calculated for each signal.

- Each set of data is compared with average values. If the difference is greater than the limitations set, then the corresponding set of data is eliminated.
- The data left are calculated for average and assigned to each droplet.

Figure 5.6: Workflow for data selection from each droplet.

5.2.6 Identification of pathogenic strain by the difference of change in pH during cultivation

We grew two species of bacteria, *S. aureous* and *S. epidermidis* in microdroplets. We adapted the recipe for Mannitol Salt Agar (Chapman medium) for this experiment. The adapted medium has high concentration of salt, mannitol as main carbon source, and a small portion of glucose. This medium has no agar for use in liquid form and no phenol red since we are using pH sensor nanoparticles to monitor pH. Additionally, we added 0.1% w/w of Tween 80 in the medium to reduce the clumping of the cells.

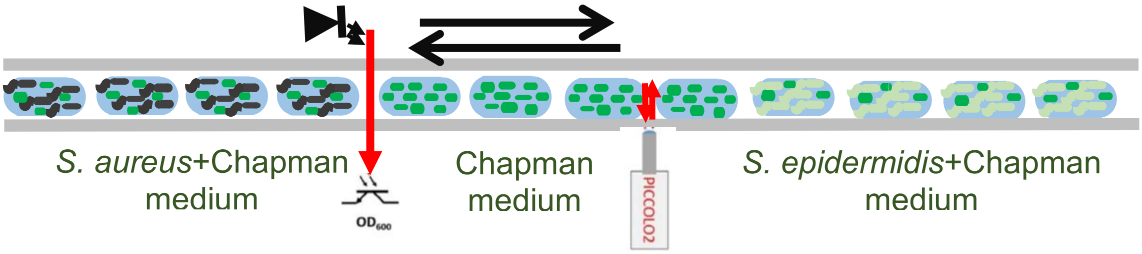
S. aureus+Chapman medium
Chapman medium
S. epidermidis+Chapman medium
OD600
PICCOLO2

Figure 5.7: Illustration of experiment of incubation of droplets with different composition i) seeded with *S. aureus*, ii) seeded with *S. epidermidis*, iii) seeded with no cells in single batch of cultivation.

In each experiment, we generated three groups of droplets: i) seeded with *S. aureus*, ii) seeded with *S. epidermidis*, iii) seeded with no cells (Figure 5.7). The only difference of control group and experimental group is the control group are not seeded with cells. They are in the system to check if there is any cross-contamination during the culturing. After the generation of the droplets, we cycled them in the tubing. Every 30 minutes, they passed by the detection unit for OD and pH and concentration of oxygen measurement.

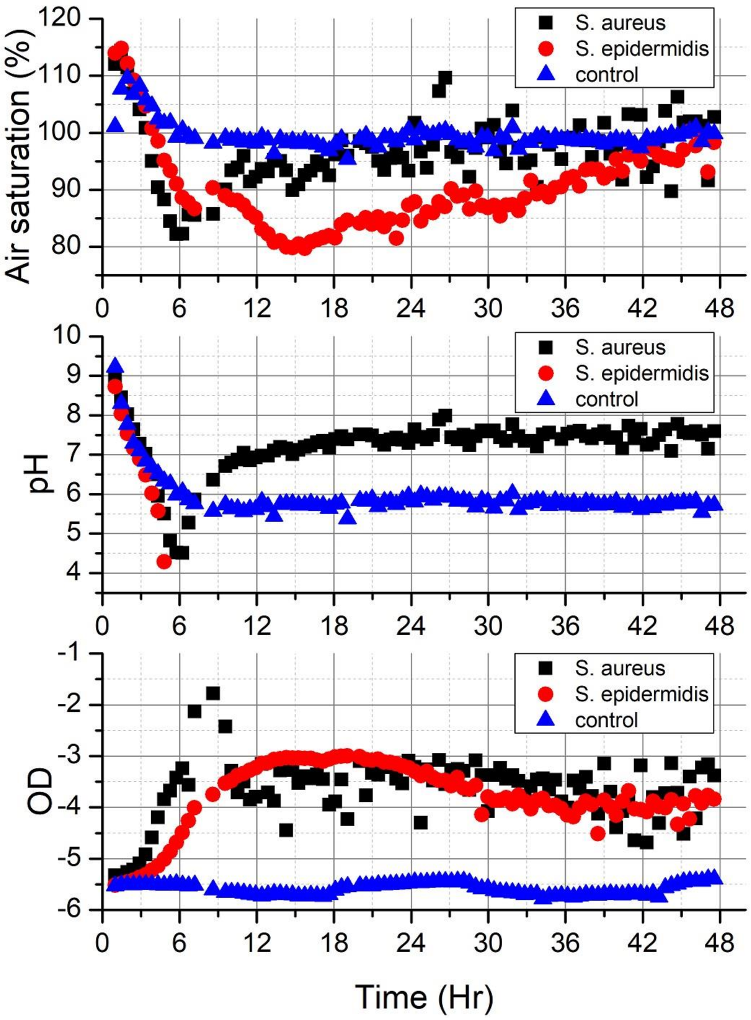

Figure 5.8: Measurement of the concentration of oxygen, pH and optical density in droplet culturing *S. aureus*, *S. epidermidis* and control group.

First in the optical density measurement, the OD indicating voltage values show the growth of *S. aureus* and *S. epidermidis* in droplet but not in control group. It confirms that there was no cross-contamination in the system. But *S. epidermidis*, which is adaptable to chapman media, should not grow, or grow very little in this case. We didn't observe this. The *S. epidermidis* grew almost as much as *S. aureus* in chapman media.

The level of oxygen was almost the same for all three kinds of droplets. The size of the droplets is in the µl range, and the space between the droplets is big. So we didn't observe oxygen limitation in the experiment. The air-saturation level in all droplets remained above 80% during the whole incubation.

The pH measurement has significant change during the first 6 hours of incubation. This significant change appeared also in the measurement of oxygen. We suspect that the media is interacting with the nanoparticles sensor, thus affects the measurement. After the 6 hours, this influence is very slight and the measurement tends to be stable. The pH measurement of *S. epidermidis* was out of range (too low). We didn't obvious pH drop in the droplets seeded with *S. aureus*. The cells didn't grow properly in this media as shown from the optical density measurement, as well as the sensor nanoparticles didn't work properly either due to the interference from the media. We investigated the effect of media on the sensor nanoparticles in the following section.

5.2.7 Effect of culturing media on the pH sensor nanoparticles

Chapman medium used is a selective medium for *S. aureus*. It contains high concentration of salt and surfactant to reduce clumping of cells. We noticed the medium used affected the signal from the pH nanoparticles. This change of signal happened at the beginning of adding nanoparticles in the medium and lasted about 6 to 10 hours. There was no further change during the rest of the experiment.

This change in signal always shown during the calibration of the sensors. Each group of droplets was made of media solutions at defined pH. After generation of the droplets, they circulated in the system and were measured every hour. From the figure 5.9, we can see the signal decrease during the first 9 hours in contact with media.

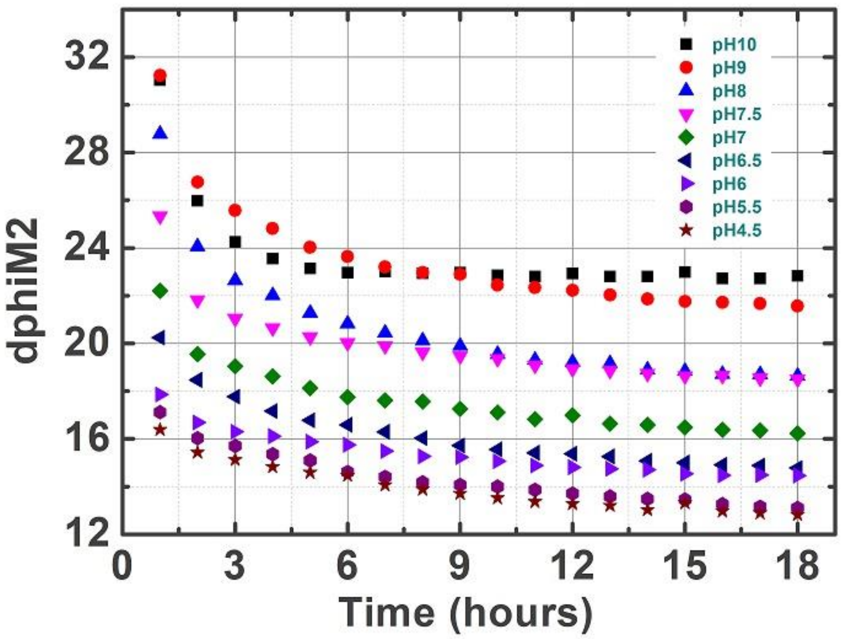

Figure 5.9: Signal of pH measurement on the calibration droplets over 18 hours.

To fully understand the effect of culturing media on the pH sensor nanoparticles, we separated each ingredient in the medium and checked its effect on the sensor signal (as listed in Table 5.2).

Table 5.2: compositions of samples for experiment to check the effect of chapman medium on pH sensor nanoparticles. Each sample only contains a single ingredient from adapted chapman medium.

sample	description	water	mannitol	dextrose	NaCl	beef extract	PCD	Tween 80
AR1	Mannitol	25ml	0.25g	0	0	0	0	0
AR2	dextrose	25ml	0	0.025g	0	0	0	0
AR3	NaCl	25ml	0	0	1.875g	0	0	0
AR4	beef extract	25ml	0	0	0	0.1g	0	0
AR5	PCD	25ml	0	0	0	0	0.25g	0
AR6	Tween 80	25ml	0	0	0	0	0	0.25g

We performed the modified dual lifetime referencing measurement on these samples and compared each of the signals.

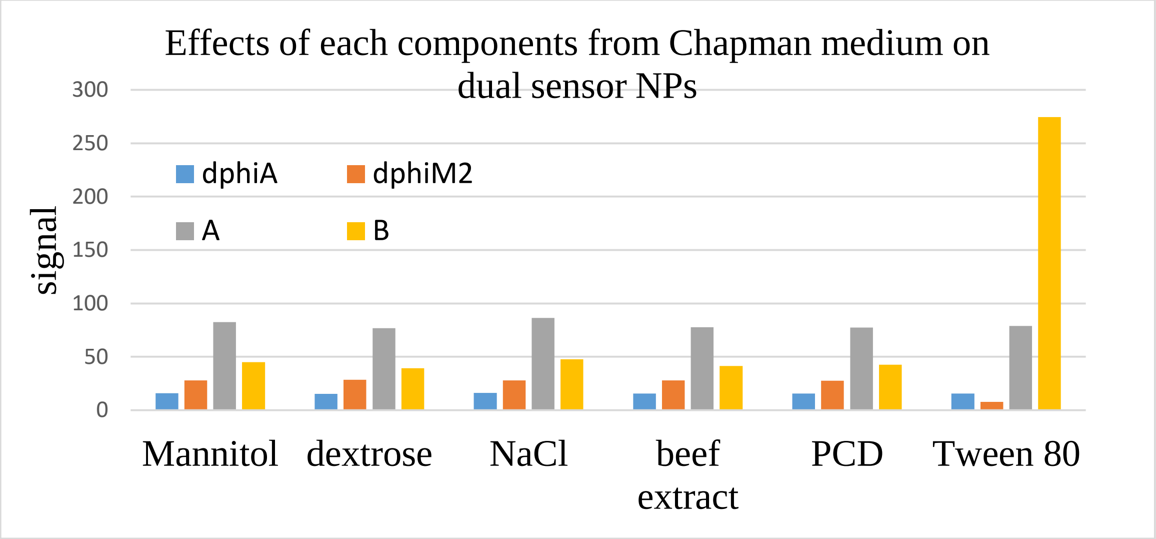

Figure 5.10: Signals from modified dual lifetime referencing method of samples with single ingredient of chapman medium.

Clearly we can see that the sample with Tween 80 only causes the great increase of B value which results in the decrease of dphiM2 values. These two changes indicate the increase of the signal from pH NPs. Consider Tween 80 as a surfactant, which is amphiphilic, it could change the interface tension of the shell and the core of PSPVP NPs, which causes the relocation of the dye from the shell (hydrophilic) to the core (hydrophobic) of the PSPVP NPs. This changes the distance of the antenna dye Zn-Schiff base and the pH indicator dye (aza-BODIPY).

Effect of surfactant on pH sensor nanoparticles

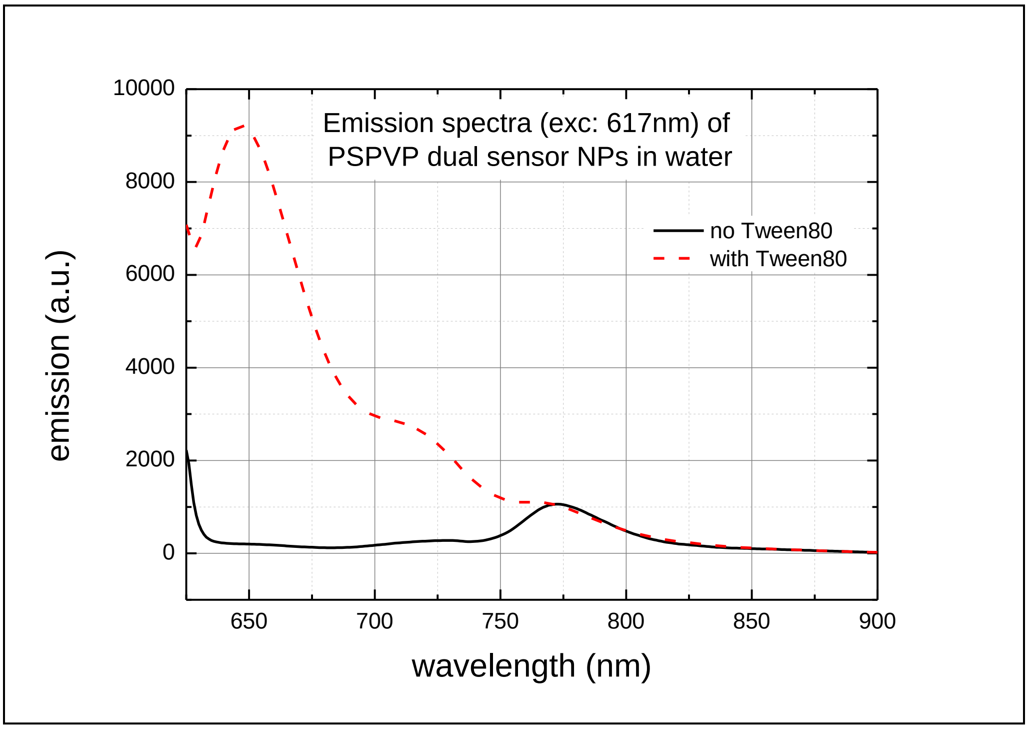

Figure 5.11: emission spectra (exc: 617 nm) of sample AR5 (no Tween 80) and AR6 (with Tween 80).

We confirmed that the energy transfer system in pH sensor nanoparticles is not working anymore. We measured the emission spectra of sample AR5 (no Tween 80) and AR6 (with Tween 80). We observed the high emission of sample with Tween 80 at wavelength of 645 nm, which is the emission from Zn-Schiff base. Conversely, we didn't observe this emission from the sample without Tween 80. This tells us the emission from Zn-Schiff base is no longer absorbed by aza-BODIPY dye, which means the energy transfer system is no longer existed.

Effect of concentration of salt on pH sensor nanoparticles

We did the calibrations of NPs in the mediums without Tween 80. We prepared two sets of calibration samples. One group has low concentration of NaCl (0.75% w/w). The other group has regular concentration of NaCl (7.5% w/w). This experiment is to check the apparent pKa values of NPs in these two mediums to define the dynamic range (working pH measurement range).

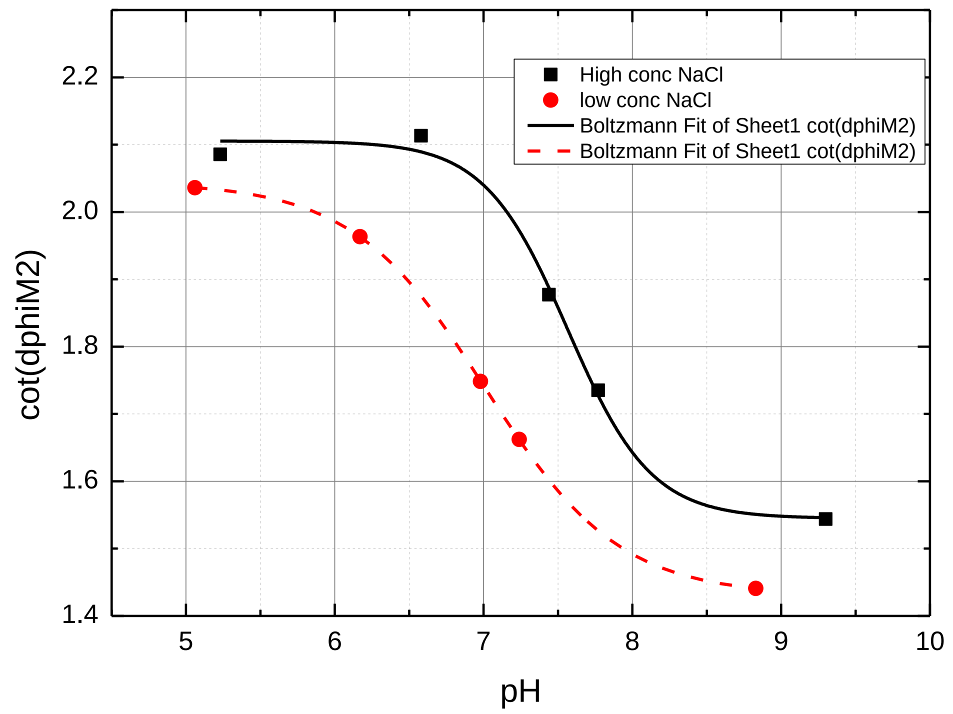

Figure 5.12: Calibration curves of pH sensor nanoparticles in adapted chapman medium with high concentration of NaCl and low concentration of NaCl.

NPs in the medium with low concentration of NaCl has the apparent pKa value at 7.01, which is similar with previous investigation. And the apparent pKa value of NPs in the medium with high concentration of NaCl is above 7.57, which is confirmed with what we have observed in Warsaw two weeks ago. So the medium with low concentration of NaCl gives us more suitable dynamic range (pH 6-8) to work with our applications.

5.3 Discussion

5.3.1 Extended dynamic range of optical pH sensor by using different aza-BODIPY building block

A broad dynamic range is always a feature desired for optical pH sensors. In the work from Strobl [117], the mixture of different derivatives of aza-BODIPY shows great potential for measurement of pH from 3 to 10. In the mixture, the author used the indicator molecules and dissolved them in the organic solvent. And they measured the signal change of intensity of fluorescence from fluorometer. This sensing setup is straightforward. The different kinds of pH indicators can work for their ranges. The overall signal is contributed from different indicators. And this fluorescence intensity change is directly recorded by fluorometer.

However, the nanoparticle sensor system is much more complicated than using pH indicator molecules directly. In the core–shell-structured nanoparticles, the pH sensitive dye is located in the hydrophilic shell, together with antenna dye Zn Schiff base. The distance between the antenna dye and acceptor dye affects the efficiency of energy transfer. Due to the slight difference in chemical structures of the aza-BODIPY derivatives, they stay at slightly different regions in the shell of the nanoparticles. Therefore, the overall signal contributed from each part of pH nanoparticles in the mixture is not equal. Based on the principle of modified dual lifetime referencing method, this difference of the intensity gives unequal sensitivity of the sensor to different range of pH. For this reason, we only used one kind of pH sensor nanoparticles in our experiments.

5.3.2 Potential of our tubing based microfluidic system

One of the biggest advantages of this tubing based microfluidic system is the flexibility and versatility. The architecture of the microfluidic system is built up by connecting tubes together with custom made fluidic connectors. With the help of electromagnetic valves, we are able manipulate fluid precisely in the tubing. Therefore, modules with different functions, e.g. generation, fusion, splitting of droplets, can be easily built and they allow one to perform complicated handling of fluid in the system.

Another highlight of this system is automation. With different signals generated by the sensors integrated in the system, we are able to receive real-time information about the position, movement, and composition of the droplets in the system. Therefore, we created different feedback loops in the logarithm to realize real-time monitor and control of the droplets during experiments. We believe these features of the system offer the possibility to perform more sophisticated experiments in droplet microfluidic system.

5.3.3 Potential improvement for optical pH sensing in droplets

pH is of great important during cell culturing in droplets. We tried to resolve the measurement of pH in droplets by using the core-shell-structured nanoparticles with an energy transfer system. We encountered significant influence of cells or metabolites during incubation on the energy transfer system in the optical nanoparticle sensors, which results in the constant change of optical properties.

To widen this nanoparticle pH sensor system, we have to ensure the stable optical properties of pH sensors during the whole course of the incubation. One possible solution could be bond the pH indicator molecules covalently in the nanoparticles. This approach will avoid the change of location of the dye in the nanoparticles during incubation, which could assure the stable and constant energy transfer of the optical sensor system.

A different host – a different type of nanoparticles or matrix could also be used to design a new pH sensor system. If the optical properties of the setup are constant, we could also use intensity-based measurement. This could be alternative plan for pH sensing in droplets during cell culturing. The design of the new sensing system would go through a full process including the stability, selectivity, cross-sensitivity of the sensors, the compatibility of the sensor and cell culturing, and the setup of readout system within microfluidic systems.

5.3.4 Application of machine learning for sensing and droplet microfluidic system

We are in the era that we are facing more data than ever in the history. Microfluidic technology is featured in parallelization and high throughput. These merits result in more data generated from a single experiment than ever before. I believe the combination of microfluidics system and artificial intelligent (AI) can open up new possibility for scientific research.

Machine learning is an important perspective in AI. Tom M. Mitchell provided a widely quoted, more formal definition of the algorithms studied in the Machine Learning field: “A computer program is said to learn from experience *E* with respect to some class of tasks *T* and performance measure *P* if its performance at tasks in *T*, as measured by *P*, improves with experience *E*.” [168]

For example, we use this highly automated droplet-based microfluidic system to achieve high yield of biomass, which is the task *“T”*. Performance *“P”* are the signal from multiple sensors integrated, i.e. OD, pH, and concentration of oxygen. We provide the supervise training to the program first. The high value of OD is the goal here. We do not want to have oxygen limitation for cell culturing. So when the oxygen level is below 25% air saturation, we could ask the system to split one big droplet to two droplets, or to introduce extra oil phase in between droplets. Then the pH is out of the optimal range for cell flowing, the system could merge a small drop of acid of basic to adjust the pH during cultivation. These techniques are not new. They have been used in fermenters for large-scale production for decades. But with droplet microfluidic system, we are able to acquire data from millions of separated droplet-based bioreactors in a much shorter time than in bulk. This big amount of data will definitely promote and accelerate scientific research.

More important, the machine learning could be used to improve the performance and accuracy of a sensor system. The selection of the data measured from sensors requires a lot of efforts.

Human intelligence is usually involved in the data selection. Here we can train the machine to identify the data to decide if it is valuable. So only data collected from reliable and accurate measurement are passed down to calculate the information of analyte. For example, there is an array of sensors measure the same sample. The machine can compare the data collected among different sensors. If one of the sensors is broken, the system could easily leave alone the data from this sensor along in the future events. Machine learning makes the sensor smarter than before.

5.4 Conclusions

We integrated the dual sensor nanoparticles into droplet microfluidic system. We combined the optical-based pH and the concentration of oxygen sensing system with the automated droplet cell culturing system. We first validated the performance of optical sensors for sensing of cell culturing in droplets. Then we demonstrated the cultivation of *S. aureus* and *S. epodermidis* in droplets. We monitored multiple parameters, OD, pH, and the concentration of oxygen of each droplet during cultivation.

We provide an approach to monitor pH reliably in droplet microfluidic. This approach is portable, inexpensive, and it can be used in different system. With the information of change of pH during cell culturing, we can have better understanding of the growth of cells in droplets. And the pH profile during cultivation enables the use of droplet microfluidic system to identify, isolate pathogenic strains. This technique broadens the application of droplet microfluidic for some more sophisticated experiment. It also can be used to study transfer of molecules in droplet microfluidic for fundamental study. The biologists can benefit from this technique to switch more biological experiments in the format of droplet. Also the researchers working on microfluidic can benefit from this technique for a profound understanding of droplets in the system.

5.5 Materials and Methods

5.5.1 Synthesis of the sensor nanoparticles

We prepared the dual sensor nanoparticles by staining oxygen indicator dye and pH indicator dye in the core and shell structure of the poly(styrene-*block*-vinylpyrrolidone) (PSPVP) beads. The procedure of the preparation of sensor nanoparticles is following the procedure reported before by Borisov et al. [154]. Briefly, we dilute the emulsion of PSPVP polymer with mixture of tetrahydrofuran and water, and ethanol and water to swell the core and the shell of the beads respectively. Then we dissolve the sensor dye into the emulsion by adding dropwise. The organic solvents and the emulsion is concentrated under reduced pressure.

The oxygen indicator dye used is platinum(II) *meso*-tetra(4-fluorophenyl)tetrabenzoporphyrin (PtTPTBPF) [151]. The pH indicator dyes used are BF_2-chelated tetraarylazadipyrromethene dye (aza-BODIPY dye) reported by Strobl et al. [117]. The antenna dye used is zinc(II) 2,3-bis(3,3,9,9-tetramethyl-2-hydroxyjulolidine)but-2-enedinitrile (Zn Schiff base). And it is synthesized following procedure from [35,169].

5.5.2 Detection unit

For sensing of pH and concentration of oxygen, we use a fiber-optic fluorometer Piccolo2 (Pyro Dcience GmbH, Germany) for grequency-domain lifetime measurement (phase shift). We integrated a focusing lens (GRINTECH GmbH, Germany) at the end of the fiber to increase the signal intensity for applications in microfluidic systems. The piccolo2 device has an excitation LED which is intensity-modulated. The time lag between absorption and emission causes the delay of emission light to modulated excitation light, and piccolo2 records this lag as phase shift angle (φ). We adapted the original measuring program to a dual frequency program for this work. The sample frequency is 3.3 Hz, which is limited by the electronics.

For optical density measurement, we use a red LED (600 nm) and a light-to-voltage converter (TSL257, ams AG, former TAOS). We filter and gain the voltage signal by customized electronic and acquire the signal by a National Instruments I/O device (SCB68). The measuring frequency is 20 kHz.

5.5.3 Calibration of the dual sensor nanoparticles

For calibration measurement at different oxygen level, we mixed nitrogen and compressed air to obtain gas mixture with different concentration of oxygen. We used mass flow controller (Read Y, Vögtlin Instruments GmbH) and a LabVIEW program to control the ratio of flowrates of nitrogen and compressed air.

For calibration measurement of pH, we prepared buffer solutions (Benzoate, MES, CHES, Tris) with different pKa values. Then we adjusted them to different pH values desired by adding hydrogen chloride or sodium hydroxyl and controlled by measuring with pH electrode (Inlab Micro, Mettler Toledo).

5.5.4 Tubing-based cell culturing microfluidic system

We build the system with FEP tubing (ID = 0.8 mm) and simple custom made connecting modules: T-junctions and X-junctions made by FEP [150]. The system has modular architecture. The operation of the system is similar to the work we reported before [36]. First we fill up the aspiration tubes with aqueous solution. We generate the droplets by injecting a segment of aqueous phase into organic phase. During this process, we keep the constant hydrodynamic resistance to ensure the same size of the droplets. During the incubation, two sets of electromagnetic valves are switching to keep the droplets flowing and switch of directions.

5.5.5 Bacteria and Medium used

The strains used are *Staphylococcus aureus* NCTC 8325-4 and *Staphylococcus epidermidis* DSM 20044. Both strains we received thanks to Jagiellonian University in Krakow, Department of Immunology, Faculty of Biochemistry, Biophisics, and Biotechnology (Prof Joanna Cichy).

We plated bacteria on Brain Heart Infusion Agar (Biocorp, Poland) and after incubation, (37C, 24h) we picked some colonies and moved to fresh mannitol broth to reach density of 0.5 MacFarland's, which corresponds to 1.5 x 10^8 CFU/ml, such bacteria we diltuted twice with water and nanosensors.

The recipe for adapted chapman medium is in table 5.3.

Table 5.3: Composition of adapted chapman medium by A. Ruszczak.

Chapman medium adapted by A. Ruszczak		
category	**ingredient**	**weight (g)**
	water	1000
carbon source	mannitol	10
	dextrose	1
osmotic	NaCl	75
Nitrogen source	beef extract	4
	Peptone casein digest	5
surfactant	Tween 80	1
pH	7.4 +/- 0.4	

5.6 Supplementary information

5.6.1 Temperature during the incubation in droplets

We used a heating plate to increase the temperature of the box for incubation. As seen in the figure below, we maintained the temperature at 37 °C during incubation. We placed a temperature sensor in the incubation box and logged in the change of temperature.

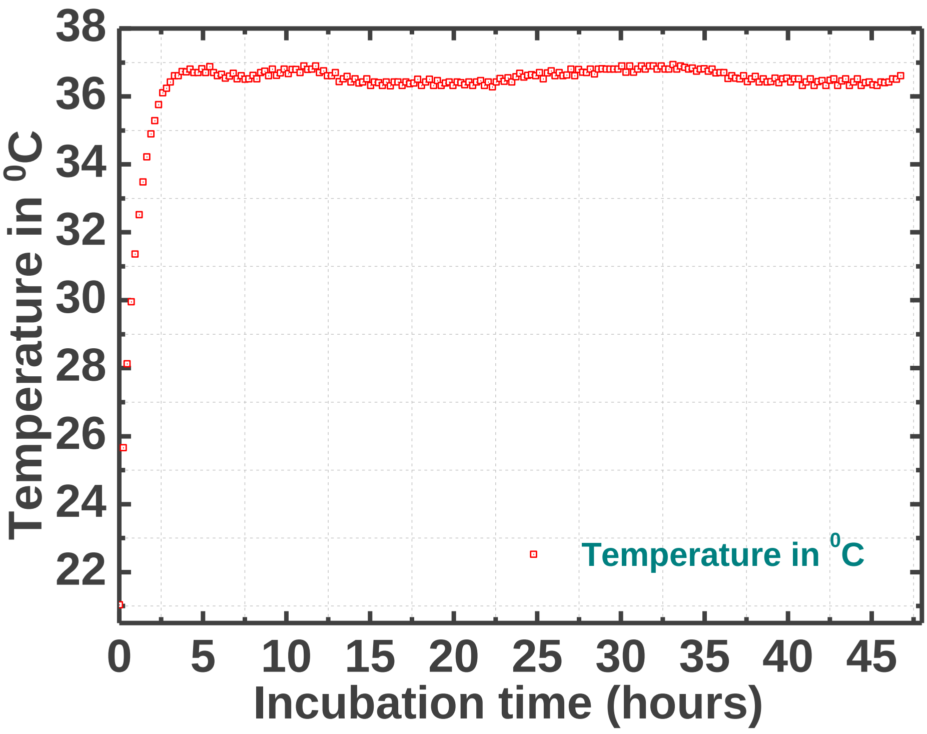

Figure 5.13: Monitoring of temperature during incubation of cells in droplets.

6 Conclusions

In this thesis, we have shown the different approaches to integrate optical chemical sensors into microfluidic systems and micro(bio)reactor. The integrated optical sensors are powerful analytical tools for monitoring (bio)processes in microfluidics. We demonstrate the oxygen imaging of enzymatic reaction in flowcell chips, single-spot oxygen and pH measurement of cultivation of yeast in micro(bio)reacotors. We also present a dedicated approach to measure pH and concentration of oxygen in microdroplets. All the measurement we have done are lifetime-based by using a miniaturized fluorometer. It provides accurate measurement. The entire setup for the measurement is simple and can be easily adapted to different microfluidic systems.

Each microfluidic system or each application requires new design of sensing strategy. This means the new design of sensor matrice, the integration method, the *in-situ* calibration. It would be ideal to have a standard microfluidic platform which is made of same material and uses same connectors. And this microfluidic system is widely used and serves for many different applications. Then the integration of optical sensors will be easy.

The applications we have shown here, online and real-time information of pH and oxygen in (bio)process in microfluidics, demonstrate the possibility of using microfluidic platform for many biological experiments. The combination of microfluidics and optical sensors is so promising. The microfluidics provides the possibility of performing large number of experiments in a short time. And the analytical tool, optical chemical sensors, give the information of reactions in each experiment. By having these features together, we are able to conduct research in a small dimension (e.g. single cell study) and in a large quantity (e.g. statistic study). This would be valuable for the study requires big data.

7 Acknowledgement of previous publications

Several sections of this dissertation have been published elsewhere or are under preparation for publication. The following are acknowledged.

- *Chapter 2 has been published in full under the citation:*

  Sun, S., Ungerböck, B., & Mayr, T. (2015). Imaging of oxygen in microreactors and microfluidic systems. *Methods and Applications in Fluorescence*, 3(3), 034002.
- *Sections of Chapter 3 has been published for publication under the citation:*

  Viefhues, M., Sun, S., Valikhani, D., Nidetzky, B., Vrouwe, E. X., Mayr, T., & Bolivar, J. M. (2017). Tailor-made resealable micro (bio) reactors providing easy integration of in situ sensors. *Journal of Micromechanics and Microengineering*, 27(6), 065012.
- *Chapter 4 has been published in full under the citation:*

  Horka, M., Sun, S., Ruszczak, A., Garstecki, P., & Mayr, T. (2016). Lifetime of Phosphorescence from Nanoparticles Yields Accurate Measurement of Concentration of Oxygen in Microdroplets, Allowing One To Monitor the Metabolism of Bacteria. *Analytical Chemistry*, 88(24), 12006-12012.

8 eferences

(1) Manz, A.; Graber, N.; Widmer, H. M. *Sens. Actuators B Chem.* **1990**, *1* (1–6), 244–248.

(2) Dittrich, P. S.; Tachikawa, K.; Manz, A. *Anal. Chem.* **2006**, *78* (12), 3887–3908.

(3) Cammann, K.; Guibault, E. .; Hall, H.; Kellner, R.; Wolfbeis, O. S. .

(4) Wolfbeis, O. S. *Anal. Chem.* **2000**, *72* (12), 81–90.

(5) Wolfbeis, O. S. *Anal. Chem.* **2008**, *80* (12), 4269–4283.

(6) Wang, X.-D.; Wolfbeis, O. S. *Anal. Chem.* **2013**, *85* (2), 487–508.

(7) *Optical chemical sensors*; Baldini, F., North Atlantic Treaty Organization, Eds.; NATO science series; Springer: Dordrecht, 2006.

(8) McDonagh, C.; Burke, C. S.; MacCraith, B. D. *Chem. Rev.* **2008**, *108* (2), 400–422.

(9) Carraway, E. R.; Demas, J. N.; DeGraff, B. A.; Bacon, J. R. *Anal. Chem.* **1991**, *63* (4), 337–342.

(10) Staudinger, C.; Borisov, S. M. *Methods Appl. Fluoresc.* **2015**, *3* (4), 042005.

(11) Jokic, T.; Borisov, S. M.; Saf, R.; Nielsen, D. A.; Kühl, M.; Klimant, I. *Anal. Chem.* **2012**, *84* (15), 6723–6730.

(12) de Silva, A. P.; Gunaratne, H. Q. N.; Lynch, P. L. M.; Patty, A. J.; Spence, G. L. *J. Chem. Soc. Perkin Trans. 2* **1993**, No. 9, 1611.

(13) Hall, M. J.; Allen, L. T.; O'Shea, D. F. *Org. Biomol. Chem.* **2006**, *4* (5), 776.

(14) Wolfbeis, O. S. *J. Mater. Chem.* **2005**, *15* (27–28), 2657.

(15) Aspray, W. *IEEE Ann. Hist. Comput.* **1997**, *19* (3), 4–15.

(16) Warnock, J.; Berry, C.; Wood, M. H.; Sigal, L.; Chan, Y.; Mayer, G.; Mayo, M.; Chan, Y.-H.; Malgioglio, F.; Strevig, G.; Nagarajan, C.; Carey, S.; Salem, G.; Schroeder, F.; Smith, H. H.; Phan, D.; Nigaglioni, R. H.; Strach, T.; Ziegler, M. M.; Fricke, N.; Lind, K.; Neves, J. L.; Rangarajan, S. H.; Surprise, J. P.; Isakson, J. M.; Badar, J.; Malone, D.; Plass, D. W.; Aipperspach, A.; Wendel, D. F.; Averill, R. M.; Puri, R. *IBM J. Res. Dev.* **2015**, *59* (4/5), 15:1-15:15.

(17) Taylor, G. *Proc. R. Soc. Math. Phys. Eng. Sci.* **1953**, *219* (1137), 186–203.

(18) Aris, R. *Proc. R. Soc. Math. Phys. Eng. Sci.* **1956**, *235* (1200), 67–77.

(19) Casadevall i Solvas, X.; deMello, A. *Chem Commun* **2011**, *47* (7), 1936–1942.

(20) Garstecki, P.; Fuerstman, M. J.; Stone, H. A.; Whitesides, G. M. *Lab. Chip* **2006**, *6* (3), 437.

(21) Anna, S. L.; Bontoux, N.; Stone, H. A. *Appl. Phys. Lett.* **2003**, *82* (3), 364–366.

(22) Huebner, A.; Sharma, S.; Srisa-Art, M.; Hollfelder, F.; Edel, J. B.; deMello, A. J. *Lab. Chip* **2008**, *8* (8), 1244.

(23) Baraban, L.; Bertholle, F.; Salverda, M. L. M.; Bremond, N.; Panizza, P.; Baudry, J.; de Visser, J. A. G. M.; Bibette, J. *Lab. Chip* **2011**, *11* (23), 4057.

(24) Basova, E. Y.; Foret, F. *The Analyst* **2015**, *140* (1), 22–38.

(25) Theberge, A. B.; Courtois, F.; Schaerli, Y.; Fischlechner, M.; Abell, C.; Hollfelder, F.; Huck, W. T. S. *Angew. Chem. Int. Ed.* **2010**, *49* (34), 5846–5868.

(26) Kaminski, T. S.; Scheler, O.; Garstecki, P. *Lab Chip* **2016**, *16*, 2168–2187.

(27) Kaminski, T. S.; Garstecki, P. *Chem Soc Rev* **2017**.

(28) Gruber, P.; Marques, M. P. C.; Szita, N.; Mayr, T. *Lab Chip* **2017**, *17* (16), 2693–2712.

(29) Ungerböck, B.; Charwat, V.; Ertl, P.; Mayr, T. *Lab. Chip* **2013**, *13* (8), 1593–1601.

(30) Courtois, F.; Olguin, L. F.; Whyte, G.; Theberge, A. B.; Huck, W. T. S.; Hollfelder, F.; Abell, C. *Anal. Chem.* **2009**, *81* (8), 3008–3016.

(31) Lyu, F.; Xu, M.; Cheng, Y.; Xie, J.; Rao, J.; Tang, S. K. Y. *Biomicrofluidics* **2015**, *9* (4), 044120.

(32) Scheler, O.; Kaminski, T. S.; Ruszczak, A.; Garstecki, P. *ACS Appl. Mater. Interfaces* **2016**, *8* (18), 11318–11325.

(33) Cao, J.; Nagl, S.; Kothe, E.; Köhler, J. M. *Microchim. Acta* **2014**, 1–10.

(34) Funfak, A.; Cao, J.; Wolfbeis, O. S.; Martin, K.; Köhler, J. M. *Microchim. Acta* **2009**, *164* (3–4), 279–286.

(35) Ehgartner, J.; Strobl, M.; Bolivar, J. M.; Rabl, D.; Rothbauer, M.; Ertl, P.; Borisov, S. M.; Mayr, T. *Anal. Chem.* **2016**.

(36) Horka, M.; Sun, S.; Ruszczak, A.; Garstecki, P.; Mayr, T. *Anal. Chem.* **2016**, *88* (24), 12006–12012.

(37) Ungerböck, B.; Fellinger, S.; Sulzer, P.; Abel, T.; Mayr, T. *The Analyst* **2014**, *139* (10), 2551.

(38) Lasave, L. C.; Borisov, S. M.; Ehgartner, J.; Mayr, T. *RSC Adv* **2015**, *5* (87), 70808–70816.

(39) Terry, S. C.; Jerman, J. H.; Angell, J. B. *IEEE Trans. Electron Devices* **1979**, *26* (12), 1880–1886.

(40) Petersen, K. E. *IEEE Trans. Electron Devices* **1979**, *ED-26* (12), 1918–1920.

(41) Squires, T. M.; Quake, S. R. *Rev. Mod. Phys.* **2005**, *77* (3), 977–1026.

(42) Stone, H. A.; Stroock, A. D.; Ajdari, A. *Annu. Rev. Fluid Mech.* **2004**, *36* (1), 381–411.

(43) Watts, P.; Haswell, S. J. *Curr. Opin. Chem. Biol.* **2003**, *7* (3), 380–387.

(44) Dittrich, P. S.; Manz, A. *Nat. Rev. Drug Discov.* **2006**, *5* (3), 210–218.

(45) Brivio, M.; Verboom, W.; Reinhoudt, D. N. *Lab. Chip* **2006**, *6* (3), 329.

(46) Watts, P.; Haswell, S. J. *Chem. Soc. Rev.* **2005**, *34* (3), 235.

(47) Andersson, H.; Berg, A. van den. *Lab. Chip* **2004**, *4* (2), 98.

(48) Ahn, C. H.; Choi, J.-W.; Beaucage, G.; Nevin, J. H.; Lee, J.-B.; Puntambekar, A.; Lee, J. Y. *Proc. IEEE* **2004**, *92* (1), 154–173.

(49) El-Ali, J.; Sorger, P. K.; Jensen, K. F. *Nature* **2006**, *442* (7101), 403–411.

(50) Andersson, H.; van den Berg, A. *Sens. Actuators B Chem.* **2003**, *92* (3), 315–325.

(51) Wang, X.; Wolfbeis, O. S. *Chem. Soc. Rev.* **2014**, *43* (10), 3666.

(52) Schäferling, M. *Angew. Chem. Int. Ed.* **2012**, *51* (15), 3532–3554.

(53) Grist, S. M.; Chrostowski, L.; Cheung, K. C. *Sensors* **2010**, *10* (10), 9286–9316.

(54) Nock, V.; Blaikie, R. J.; Alkaisi, M. M. *Nanopatterning Nanoscale Devices Biol. Appl.* **2014**, 209.

(55) Nock, V.; Blaikie, R. J.; David, T. Nicolau, D. V., Abbott, D., Kalantar-Zadeh, K., Di Matteo, T., Bezrukov, S. M., Eds.; 2007; p 67990Y–67990Y–10.

(56) Nock, V.; Blaikie, R. J.; David, T. *Lab. Chip* **2008**, *8* (8), 1300.

(57) Chen, J.; Kim, H. D.; Kim, K. C. *Microfluid. Nanofluidics* **2013**, *14* (3–4), 541–550.

(58) Ungerböck, B.; Pohar, A.; Mayr, T.; Plazl, I. *Microfluid. Nanofluidics* **2013**, *14* (3–4), 565–574.

(59) Sud, D.; Mehta, G.; Mehta, K.; Linderman, J.; Takayama, S.; Mycek, M.-A. *J. Biomed. Opt.* **2006**, *11* (5), 050504.

(60) Lam, R. H. W.; Kim, M.-C.; Thorsen, T. *Anal. Chem.* **2009**, *81* (14), 5918–5924.

(61) Lakowicz, J. R. *Principles of fluorescence spectroscopy*; Springer: New York, 2006.

(62) Meier, R. J.; Fischer, L. H.; Wolfbeis, O. S.; Schäferling, M. *Sens. Actuators B Chem.* **2013**, *177*, 500–506.

(63) Borisov, S. M.; Klimant, I. *Analyst* **2008**, *133* (10), 1302–1307.

(64) Mehta, G.; Mehta, K.; Sud, D.; Song, J. W.; Bersano-Begey, T.; Futai, N.; Heo, Y. S.; Mycek, M.-A.; Linderman, J. J.; Takayama, S. *Biomed. Microdevices* **2007**, *9* (2), 123–134.

(65) Quaranta, M.; Borisov, S. M.; Klimant, I. *Bioanal. Rev.* **2012**, *4* (2–4), 115–157.

(66) Mehta, G.; Lee, J.; Cha, W.; Tung, Y.-C.; Linderman, J. J.; Takayama, S. *Anal. Chem.* **2009**, *81* (10), 3714–3722.

(67) Nock, V.; Alkaisi, M.; Blaikie, R. J. *Microelectron. Eng.* **2010**, *87* (5–8), 814–816.
(68) Thomas, P. C.; Raghavan, S. R.; Forry, S. P. *Anal. Chem.* **2011**, *83* (22), 8821–8824.
(69) Thomas, P. C.; Halter, M.; Tona, A.; Raghavan, S. R.; Plant, A. L.; Forry, S. P. *Anal. Chem.* **2009**, *81* (22), 9239–9246.
(70) Grate, J. W.; Kelly, R. T.; Suter, J.; Anheier, N. C. *Lab. Chip* **2012**, *12* (22), 4796.
(71) Gitlin, L.; Hoera, C.; Meier, R. J.; Nagl, S.; Belder, D. *Lab. Chip* **2013**, *13* (20), 4134.
(72) Grist, S. M.; Oyunerdene, N.; Flueckiger, J.; Kim, J.; Wong, P. C.; Chrostowski, L.; Cheung, K. C. *The Analyst* **2014**, *139* (22), 5718–5727.
(73) Amao, Y. *Microchim. Acta* **2003**, *143* (1), 1–12.
(74) Vollmer, A. P.; Probstein, R. F.; Gilbert, R.; Thorsen, T. *Lab. Chip* **2005**, *5* (10), 1059.
(75) Lin, Z.; Cherng-Wen, T.; Roy, P.; Trau, D. *Lab. Chip* **2009**, *9* (2), 257.
(76) Wang, L.; Acosta, M. A.; Leach, J. B.; Carrier, R. L. *Lab. Chip* **2013**, *13* (8), 1586–1592.
(77) Wang, L.; Liu, W.; Wang, Y.; Wang, J.; Tu, Q.; Liu, R.; Wang, J. *Lab. Chip* **2013**, *13* (4), 695.
(78) Toepke, M. W.; Beebe, D. J. *Lab. Chip* **2006**, *6* (12), 1484.
(79) Mistlberger, G.; Klimant, I. *Bioanal. Rev.* **2010**, *2* (1–4), 61–101.
(80) Borisov, S. M.; Mayr, T.; Mistlberger, G.; Waich, K.; Koren, K.; Chojnacki, P.; Klimant, I. *Talanta* **2009**, *79* (5), 1322–1330.
(81) Aigner, D.; Ungerböck, B.; Mayr, T.; Saf, R.; Klimant, I.; Borisov, S. M. *J. Mater. Chem. C* **2013**, *1* (36), 5685.
(82) Niedermair, F.; Borisov, S. M.; Zenkl, G.; Hofmann, O. T.; Weber, H.; Saf, R.; Klimant, I. *Inorg. Chem.* **2010**, *49* (20), 9333–9342.
(83) Borisov, S. M.; Klimant, I. *Anal. Chem.* **2007**, *79* (19), 7501–7509.
(84) Mayr, T.; Borisov, S. M.; Abel, T.; Enko, B.; Waich, K.; Mistlberger, G.; Klimant, I. *Anal. Chem.* **2009**, *81* (15), 6541–6545.
(85) Borisov, S. M.; Zenkl, G.; Klimant, I. *ACS Appl. Mater. Interfaces* **2010**, *2* (2), 366–374.
(86) Cadenas, E. *Annu. Rev. Biochem.* **1989**, *58* (1), 79–110.
(87) Kuswandi, B.; Nuriman; Huskens, J.; Verboom, W. *Anal. Chim. Acta* **2007**, *601* (2), 141–155.
(88) Park, J.; Bansal, T.; Pinelis, M.; Maharbiz, M. M. *Lab. Chip* **2006**, *6* (5), 611.
(89) Ochs, C. J.; Kasuya, J.; Pavesi, A.; Kamm, R. D. *Lab. Chip* **2014**, *14* (3), 459–462.
(90) Mistlberger, G.; Koren, K.; Scheucher, E.; Aigner, D.; Borisov, S. M.; Zankel, A.; Pölt, P.; Klimant, I. *Adv. Funct. Mater.* **2010**, *20* (11), 1842–1851.
(91) Mak, W. C.; Cheung, K. Y.; Trau, D. *Chem. Mater.* **2008**, *20* (17), 5475–5484.
(92) Molter, T. W.; McQuaide, S. C.; Suchorolski, M. T.; Strovas, T. J.; Burgess, L. W.; Meldrum, D. R.; Lidstrom, M. E. *Sens. Actuators B Chem.* **2009**, *135* (2), 678–686.
(93) Dragavon, J.; Molter, T.; Young, C.; Strovas, T.; McQuaide, S.; Holl, M.; Zhang, M.; Cookson, B.; Jen, A.; Lidstrom, M.; Meldrum, D.; Burgess, L. *J. R. Soc. Interface* **2008**, *5* (Suppl_2), S151–S159.
(94) Molter, T. W.; Holl, M. R.; Dragavon, J. M.; McQuaide, S. C.; Anderson, J. B.; Young, A.; Burgess, L. W.; Lidstrom, M. E.; Meldrum, D. R. *IEEE Trans. Autom. Sci. Eng.* **2008**, *5* (1), 32–42.
(95) Chan, S. P.; Fuller, Z. J.; Demas, J. N.; DeGraff, B. A. *Anal. Chem.* **2001**, *73* (18), 4486–4490.
(96) Moore, C.; Chan, S. P.; Demas, J. N.; DeGraff, B. A. *Appl. Spectrosc.* **2004**, *58* (5), 603–607.
(97) Huang, S.-H.; Hsu, Y.-H.; Wu, C.-W.; Wu, C.-J. *Biomicrofluidics* **2012**, *6* (4), 044118.
(98) Huang, S.-H.; Tsai, C.-H.; Wu, C.-W.; Wu, C.-J. *Sens. Actuators Phys.* **2011**, *165* (2), 139–146.
(99) Etzkorn, J. R.; Wu, W.-C.; Tian, Z.; Kim, P.; Jang, S.-H.; Meldrum, D. R.; Jen, A. K.-Y.; Parviz, B. A. *J. Micromechanics Microengineering* **2010**, *20* (9), 095017.

(100) Zhu, H.; Tian, Y.; Bhushan, S.; Su, F.; Meldrum, D. R. *IEEE Sens. J.* **2012**, *12* (6), 1668–1672.

(101) Grate, J. W.; Zhang, C.; Wilkins, M.; Warner, M. G.; Anheier, N. C.; Suter, J.; Kelly, R.; Oostrom, M. George, T., Islam, M. S., Dutta, A. K., Eds.; 2013; p 872522.

(102) Stich, M. I. J.; Fischer, L. H.; Wolfbeis, O. S. *Chem. Soc. Rev.* **2010**, *39* (8), 3102.

(103) Ehgartner, J.; Wiltsche, H.; Borisov, S. M.; Mayr, T. *The Analyst* **2014**, *139* (19), 4924.

(104) Clouthier, C. M.; Pelletier, J. N. *Chem. Soc. Rev.* **2012**, *41* (4), 1585.

(105) Bornscheuer, U. T.; Huisman, G. W.; Kazlauskas, R. J.; Lutz, S.; Moore, J. C.; Robins, K. *Nature* **2012**, *485* (7397), 185–194.

(106) Patel, R. N. *ACS Catal.* **2011**, *1* (9), 1056–1074.

(107) Bolivar, J. M.; Consolati, T.; Mayr, T.; Nidetzky, B. *Trends Biotechnol.* **2013**, *31* (3), 194–203.

(108) Dudukovic, M. P.; Larachi, F.; Mills, P. L. *Chem. Eng. Sci.* **1999**, *54* (13–14), 1975–1995.

(109) Rigopoulos, S.; Jones, A. *Chem. Eng. Sci.* **2003**, *58* (14), 3077–3089.

(110) Losey, M. W.; Schmidt, M. A.; Jensen, K. F. *Ind. Eng. Chem. Res.* **2001**, *40* (12), 2555–2562.

(111) Jensen, K. F. *Chem. Eng. Sci.* **2001**, *56* (2), 293–303.

(112) Günther, A.; Jensen, K. F. *Lab Chip* **2006**, *6* (12), 1487–1503.

(113) Demming, S.; Peterat, G.; Llobera, A.; Schmolke, H.; Bruns, A.; Kohlstedt, M.; Al-Halhouli, A.; Klages, C.-P.; Krull, R.; Büttgenbach, S. *Biomicrofluidics* **2012**, *6* (3), 034106.

(114) Peterat, G.; Schmolke, H.; Lorenz, T.; Llobera, A.; Rasch, D.; Al-Halhouli, A. T.; Dietzel, A.; Büttgenbach, S.; Klages, C.-P.; Krull, R. *Biotechnol. Bioeng.* **2014**, *111* (9), 1809–1819.

(115) Krull, R.; Peterat, G. *Biochem. Eng. J.* **2016**, *105*, 220–229.

(116) Bolivar, J. M.; Nidetzky, B. *Biotechnol. Bioeng.* **2012**, *109* (6), 1490–1498.

(117) Strobl, M.; Rappitsch, T.; Borisov, S. M.; Mayr, T.; Klimant, I. *The Analyst* **2015**, *140* (21), 7150–7153.

(118) Berke, H. *Chem Soc Rev* **2007**, *36* (1), 15–30.

(119) Ehgartner, J.; Sulzer, P.; Burger, T.; Kasjanow, A.; Bouwes, D.; Krühne, U.; Klimant, I.; Mayr, T. *Sens. Actuators B Chem.* **2016**, *228*, 748–757.

(120) Moser, C.; Mayr, T.; Klimant, I. *Anal. Chim. Acta* **2006**, *558* (1–2), 102–109.

(121) Tsukahara, T.; Mawatari, K.; Hibara, A.; Kitamori, T. *Anal. Bioanal. Chem.* **2008**, *391* (8), 2745–2752.

(122) Saias, L.; Autebert, J.; Malaquin, L.; Viovy, J.-L. *Lab. Chip* **2011**, *11* (5), 822.

(123) Rupprecht, P.; Golé, L.; Rieu, J.-P.; Vézy, C.; Ferrigno, R.; Mertani, H. C.; Rivière, C. *Biomicrofluidics* **2012**, *6* (1), 014107.

(124) Bolivar, J. M.; Tribulato, M. A.; Petrasek, Z.; Nidetzky, B. *Biotechnol. Bioeng.* **2016**, *113* (11), 2342–2349.

(125) Bolivar, J. M.; Consolati, T.; Mayr, T.; Nidetzky, B. *Biotechnol. Bioeng.* **2013**, *110* (8), 2086–2095.

(126) Greenfield, P. F.; Kittrell, J. R.; Laurence, R. L. *Anal. Biochem.* **1975**, *65* (1–2), 109–124.

(127) Jones, K. D.; Kompala, D. S. *J. Biotechnol.* **1999**, *71* (1–3), 105–131.

(128) Vincent, M. E.; Liu, W.; Haney, E. B.; Ismagilov, R. F. *Chem. Soc. Rev.* **2010**, *39* (3), 974.

(129) Guo, M. T.; Rotem, A.; Heyman, J. A.; Weitz, D. A. *Lab. Chip* **2012**, *12* (12), 2146.

(130) Kintses, B.; van Vliet, L. D.; Devenish, S. R.; Hollfelder, F. *Curr. Opin. Chem. Biol.* **2010**, *14* (5), 548–555.

(131) Jakiela, S.; Kaminski, T. S.; Cybulski, O.; Weibel, D. B.; Garstecki, P. *Angew. Chem. Int. Ed.* **2013**, *52* (34), 8908–8911.

(132) Boitard, L.; Cottinet, D.; Bremond, N.; Baudry, J.; Bibette, J. *Eng. Life Sci.* **2015**, *15* (3), 318–326.

(133) Huebner, A.; Srisa-Art, M.; Holt, D.; Abell, C.; Hollfelder, F.; deMello, A. J.; Edel, J. B. *Chem. Commun.* **2007**, No. 12, 1218.

(134) Martin, K.; Henkel, T.; Baier, V.; Grodrian, A.; Schön, T.; Roth, M.; Michael Köhler, J.; Metze, J. *Lab Chip* **2003**, *3* (3), 202–207.

(135) Bjork, S. M.; Sjostrom, S. L.; Andersson-Svahn, H.; Joensson, H. N. *Biomicrofluidics* **2015**, *9* (4), 044128.

(136) Shim, J.; Olguin, L. F.; Whyte, G.; Scott, D.; Babtie, A.; Abell, C.; Huck, W. T. S.; Hollfelder, F. *J. Am. Chem. Soc.* **2009**, *131* (42), 15251–15256.

(137) Churski, K.; Kaminski, T. S.; Jakiela, S.; Kamysz, W.; Baranska-Rybak, W.; Weibel, D. B.; Garstecki, P. *Lab. Chip* **2012**, *12* (9), 1629.

(138) Zang, E.; Brandes, S.; Tovar, M.; Martin, K.; Mech, F.; Horbert, P.; Henkel, T.; Figge, M. T.; Roth, M. *Lab. Chip* **2013**, *13* (18), 3707.

(139) Huebner, A.; Olguin, L. F.; Bratton, D.; Whyte, G.; Huck, W. T. S.; de Mello, A. J.; Edel, J. B.; Abell, C.; Hollfelder, F. *Anal. Chem.* **2008**, *80* (10), 3890–3896.

(140) Baret, J.-C.; Miller, O. J.; Taly, V.; Ryckelynck, M.; El-Harrak, A.; Frenz, L.; Rick, C.; Samuels, M. L.; Hutchison, J. B.; Agresti, J. J.; Link, D. R.; Weitz, D. A.; Griffiths, A. D. *Lab. Chip* **2009**, *9* (13), 1850.

(141) Lim, J.; Vrignon, J.; Gruner, P.; Karamitros, C. S.; Konrad, M.; Baret, J.-C. *Appl. Phys. Lett.* **2013**, *103* (20), 203704.

(142) Najah, M.; Mayot, E.; Mahendra-Wijaya, I. P.; Griffiths, A. D.; Ladame, S.; Drevelle, A. *Anal. Chem.* **2013**, *85* (20), 9807–9814.

(143) Abalde-Cela, S.; Gould, A.; Liu, X.; Kazamia, E.; Smith, A. G.; Abell, C. *J. R. Soc. Interface* **2015**, *12* (106), 20150216–20150216.

(144) Churski, K.; Ruszczak, A.; Jakiela, S.; Garstecki, P. *Micromachines* **2015**, *6* (10), 1514–1525.

(145) Garcia-Ochoa, F.; Gomez, E.; Santos, V. E.; Merchuk, J. C. *Biochem. Eng. J.* **2010**, *49* (3), 289–307.

(146) Oomen, P. E.; Skolimowski, M. D.; Verpoorte, E. *Lab Chip* **2016**, *16* (18), 3394–3414.

(147) Mahler, L.; Tovar, M.; Weber, T.; Brandes, S.; Rudolph, M. M.; Ehgartner, J.; Mayr, T.; Figge, M. T.; Roth, M.; Zang, E. *RSC Adv* **2015**, *5* (123), 101871–101878.

(148) Grist, S.; Schmok, J.; Liu, M.-C.; Chrostowski, L.; Cheung, K. *Sensors* **2015**, *15* (8), 20030–20052.

(149) Abbyad, P.; Tharaux, P.-L.; Martin, J.-L.; Baroud, C. N.; Alexandrou, A. *Lab. Chip* **2010**, *10* (19), 2505.

(150) Cybulski, O.; Jakiela, S.; Garstecki, P. *Lab Chip* **2016**, *16* (12), 2198–2210.

(151) Borisov, S. M.; Nuss, G.; Haas, W.; Saf, R.; Schmuck, M.; Klimant, I. *J. Photochem. Photobiol. Chem.* **2009**, *201* (2–3), 128–135.

(152) Nagarajan, R.; Barry, M.; Ruckenstein, E. *Langmuir* **1986**, *2* (2), 210–215.

(153) Haulbrook, W. R.; Feerer, J. L.; Hatton, T. A.; Tester, J. W. *Environ. Sci. Technol.* **1993**, *27* (13), 2783–2788.

(154) Borisov, S. M.; Mayr, T.; Klimant, I. *Anal. Chem.* **2008**, *80* (3), 573–582.

(155) Klann, A. G.; Belanger, A. E.; Abanes-De Mello, A.; Lee, J. Y.; Hatfull, G. F. *J. Bacteriol.* **1998**, *180* (1), 65–72.

(156) Holst, G. A.; Kuehl, M.; Klimant, I. V. Scheggi, A., Ed.; 1995; pp 387–398.

(157) Welch, D.; Christen, J. B. *Lab. Chip* **2014**, *14* (6), 1191.

(158) Fomina, N.; Johnson, C. A.; Maruniak, A.; Bahrampour, S.; Lang, C.; Davis, R. W.; Kavusi, S.; Ahmad, H. *Lab Chip* **2016**, *16* (12), 2236–2244.

(159) Gubanova, O.; Andrianova, M.; Saveliev, M.; Komarova, N.; Kuznetsov, E.; Kuznetsov, A. *Mater. Sci. Semicond. Process.* **2017**, *60*, 71–78.
(160) Mousavi Shaegh, S. A.; De Ferrari, F.; Zhang, Y. S.; Nabavinia, M.; Binth Mohammad, N.; Ryan, J.; Pourmand, A.; Laukaitis, E.; Banan Sadeghian, R.; Nadhman, A.; Shin, S. R.; Nezhad, A. S.; Khademhosseini, A.; Dokmeci, M. R. *Biomicrofluidics* **2016**, *10* (4), 044111.
(161) Lee, K. S.; Boccazzi, P.; Sinskey, A. J.; Ram, R. J. *Lab. Chip* **2011**, *11* (10), 1730–1739.
(162) Gruber, P.; Marques, M. P. C.; Sulzer, P.; Wohlgemuth, R.; Mayr, T.; Baganz, F.; Szita, N. *Biotechnol. J.* **2017**, *12* (6), 1600475.
(163) Jezierski, S.; Belder, D.; Nagl, S. *Chem Commun* **2013**, *49* (9), 904–906.
(164) Pfeiffer, S. A.; Borisov, S. M.; Nagl, S. *Microchim. Acta* **2016**.
(165) Poehler, E.; Herzog, C.; Suendermann, M.; Pfeiffer, S. A.; Nagl, S. *Eng. Life Sci.* **2015**, *15* (3), 276–285.
(166) Poehler, E.; Herzog, C.; Lotter, C.; Pfeiffer, S. A.; Aigner, D.; Mayr, T.; Nagl, S. *The Analyst* **2015**, *140* (22), 7496–7502.
(167) Mashaghi, S.; van Oijen, A. M. *Sci. Rep.* **2015**, *5* (1).
(168) Mitchell, T. M. *Machine Learning*; McGraw-Hill series in computer science; McGraw-Hill: New York, 1997.
(169) Borisov, S. M.; Saf, R.; Fischer, R.; Klimant, I. *Inorg. Chem.* **2013**, *52* (3), 1206–1216.

9 Appendix

9.1 Curriculum Vitae

CURRICULUM VITAE

SHIWEN SUN

Applied Sensor Group, Institute of Analytical Chemistry and Food Chemistry, Graz University of Technology
Stremayrgasse 9/2, 8010 Graz, Austria

Tel: +43 664 2734 821; E-mail: s.shiwen14@gmail.com

EDUCATION

2014-2017	Ph.D., Technical Chemistry Institute of Analytical Chemistry and Food Chemistry, Graz University of Technology *Graz Austria* Supervisor: Prof. Torsten Mayr Dissertation: Applications of integrated optical sensors for pH and oxygen monitoring in micro(bio)reactor
2011-2014	MSc., Chemical and Biochemical Engineering Department of Chemical and Biochemical Engineering, Rutgers University *New Jersey, USA* Supervisor: Prof. Nina Shapley Thesis: Design of polymeric nanoparticles for edible antimicrobials and chemical oxygen sensors
2007-2011	B.E., Bioengineering (*Distinction*) College of Biotechnology and Pharmaceutical Engineering, Nanjing University of Technology *Nanjing, China* Supervisor: Prof: He Huang Thesis: Using *Pennisetum alopecuroides* as raw material for bio-ethanol production

PROFESSIONAL EXPERIENCE

2015.09	Organizer *Sensor Technology for Microbioreactors and Microfluidic Systems Workshop* Graz, Austria
2013 Fall	Marshall Plan Scholar (Supervisor: Prof. Ingo Klimant) *Institute of Analytical Chemistry and Food Chemistry, Graz University of Technology* *Graz Austria*
2013 Spring	Grader *Advanced Transport Phenomenon II (Graduate level core course), Rutgers University,* Piscataway, NJ, USA
2012-2014	Research Assistant *Prof. Nina Shapley, Chemical and Biochemical Engineering, Rutgers, University* Piscataway, NJ, USA
2013	Dive master *Rutgers Scuba (PADI 5 STAR Instructor Development Center)* Piscataway, NJ, USA
2011	Intern *Professional Education, Johnson & Johnson Medical China* Shanghai, China
2008-2011	Research Assistant *Prof. He Huang, National Bio-chemical Engineering Technique Research Center* Nanjing, China

SHORT-TERM RESEARCH STAYS

2017.06	Supervisor: Prof. Piotr Garstecki *Institute of Physical Chemistry, Polish Academy of Science* Warsaw, Poland
2017.05	Supervisor: Prof. Rainer Krull *Institute of Biochemical Engineering, Technische Universität Braunschweig* Braunschweig, Germany
2017.01	Supervisor: Prof. Martin Roth

	Leibniz Institute for Natural Product Research and Infection Biology, Hans Knöll Institute Jena, Germany
2016.06	Supervisor: Martin Roth *Leibniz Institute for Natural Product Research and Infection Biology, Hans Knöll Institute* Jena, Germany
2016.01-02	Supervisor: Prof. Ulrich Krühne *Department of Chemical and Biochemical Engineering, Technical University of Denmark* Kgs. Lyngby, Denmark
2015.10	Supervisor: Prof. Piotr Garstecki *Institute of Physical Chemistry, Polish Academy of Science* Warsaw, Poland
2015.06	Supervisor: Prof. Adama Marie Sesay *Measurement Technology Unit, CEMIS-Oulu, Kajaani Universitym University of Oulu* Kajaani, Finland

EXTRACURRICULAR EXPERIENCE

2013	Student manager *Busch Campus Dining Hall, Rutgers University, Piscataway, NJ, USA*
2012	Student employee *Busch Campus Dining Hall, Rutgers University, Piscataway, NJ, USA*
2012.09	Volunteer *International Student Orientation, Rutgers University, New Brunswick, NJ, USA*
2010.01-03	Volunteer/ Project manager *AIESEC, Kumasi, Ghana*
2009-2010	President *Student Union of Nanjing University of Technology, Nanjing, China*

SCHOLARSHIP

2014-2017	Marie Skłodowska-Curie Actions Research Fellowship by European Commission
2013 Fall	Marshall Plan Scholarship by Austrian Marshall Plan Foundation

HORNORS/AWARDS

2016.04	Best presentation, DocDays 2016 NAWI, Graz Austria
2010.10	3rd Place (5%) the 7th Challenge Cup University Students Business Plan Competition, China
2009.03	Outstanding Student Leader, Nanjing University of Technology, China
2008.11	1st Place, the 4th Undergraduate Scientific Competition, Nanjing, China

PRESENTATIONS

2017.06	Shiwen Sun, Michał Horka, Miguel Tovar, Lisa Mahler, Artur Ruszczak, Josef Ehgartner, Martin Roth, Piotr Garstecki, and Torsten Mayr. Real-time determination of oxygen concentration and pH in droplet microfluidic culturing systems using optical sensor nanoparticles. Gordon Research Conferences: Microfluidics, Physics, &Chemistry of, Lucca, Italy.
2017.04	Shiwen Sun, Nicola Altenhuber, Philipp Sulzer, Ulrich Krühne, and Torsten Mayr. Glucose sensor employing optical oxygen transducer with tunable dynamic range for applications in microreactor (POSTER); Real-time determination of oxygen concentration and pH in droplet microfluidic culturing systems using optical sensor nanoparticles (ORAL). Implementation of Microreactor Technology in Biotechnology (IMTB), Bled, Slovenia.
2016.10	Shiwen Sun, Michał Horka, Miguel Tovar, Lisa Mahler, Artur Ruszczak, Josef Ehgartner, Martin Roth, Piotr Garstecki, and Torsten Mayr. Real-time determination of oxygen and pH in droplet microfluidic culturing systems using optical nanosensor particles. The Twentieth International Conference on Miniaturized Systems for Chemistry and Life Science (MicroTAS 2016), Dublin, Ireland.

2016.07	Michał Horka, Shiwen Sun Artur Ruszczak, Piotr Garstecki, and Torsten Mayr. Quantitative monitoring of oxygen concentration in droplets in microfluidic culturing systems. EMBL Conference: Microfluidics 2016, Heidelberg, Germany.
2016.04	Shiwen Sun, Michał Horka, Artur Ruszczak, Piotr Garstecki, and Torsten Mayr. Quantitatively monitor oxygen in droplets in microfluidic culturing systems. DocDays 2016 NAWI, Graz, Austria.
2016.03	Shiwen Sun, Michał Horka, Artur Ruszczak, Alice Kasjanow, Dominique Bouwes, Piotr Garstecki, and Torsten Mayr. Online oxygen monitoring in droplet based microfluidic systems using optical sensor particles. EUROPT(R)ODE-Conference on Optical Chemical Sensors and Biosensors, Graz, Austria.
2016.02	Shiwen Sun, Michał Horka, Artur Ruszczak, Piotr Garstecki, and Torsten Mayr. Quantitative monitoring of oxygen concentration in droplets in microfluidic culturing systems. 8th Workshop of Chemical and Biological Micro Laboratory Technology, Ilmenau, Germany.
2015.09	Borisov, S., Dmitriev, R. I., Lasave, L. C., Sun, S., Mayr, T., Papkovsky, D. B. & Klimant, I. Conjugated Polymer Nanoparticles as Versatile Materials for Optical Sensing and Imaging of Oxygen in Cells and Microfluidic Devices. Methods and Application of Fluorescence, Würzburg, Germany.
2015.05	Shiwen Sun, Alice Kasjanow, Dominique Bouwes, and Torsten Mayr. Oxygen determination in segmented flow systems using optical sensor particles. Implementation of Microreactor Technology in Biotechnology (IMTB), Opatija, Croatia.

PEER REVIEWED JOURNAL PUBLICATIONS

1. Viefhues, M., **Sun, S**., Valikhani, D., Nidetzky, B., Vrouwe, E. X., Mayr, T., & Bolivar, J. M. (2017). Tailor-made resealable micro (bio) reactors providing easy integration of in situ sensors. *Journal of Micromechanics and Microengineering*, *27*(6), 065012.
2. Horka, M.[*], **Sun, S**.[*], Ruszczak, A., Garstecki, P., & Mayr, T. (2016). Lifetime of Phosphorescence from Nanoparticles Yields Accurate Measurement of Concentration of Oxygen in Microdroplets, Allowing One to Monitor the Metabolism of Bacteria. *Analytical Chemistry*, *88*(24), 12006-12012. ([*]contributed equally)
3. **Sun, S.**, Ungerböck, B., & Mayr, T. (2015). Imaging of oxygen in microreactors and microfluidic systems. *Methods and Applications in Fluorescence*, *3*(3), 034002.
4. Dmitriev, R. I., Borisov, S. M., Düssmann, H., **Sun, S.**, Müller, B. J., Prehn, J., Baklaushev, V. P., Klimant, I., & Papkovsky, D. B. (2015). Versatile conjugated polymer nanoparticles for high-resolution O2 imaging in 2D and 3D cell models and tissues.